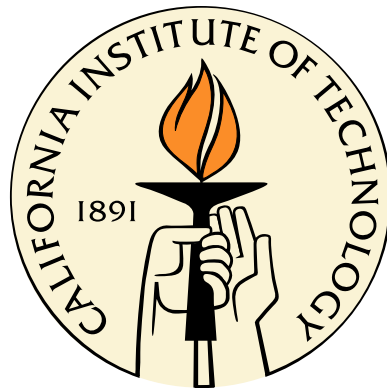


# Source imaging with dense sensor networks: Inversions based on adjoint methods

Thesis by

Surendra Nadh Somala

In Partial Fulfillment of the Requirements  
for the Degree of  
Doctor of Philosophy



California Institute of Technology  
Pasadena, California

2013

(Defended May 24, 2013)



To my nanamma (paternal grandmother), who played a key role in my upbringing, whose death ceremony I couldn't attend in fear of missing the deadline to walk this commencement.

I will regret for the rest of my life not spending time with her during her last days on the planet Earth.

# Acknowledgments

Choosing the right combination of advisors was essential in making this dissertation happen. At some point in my PhD career, my advisors were the only people I was interacting with. I had two advisors and I learned a lot from each of them. Unfortunately, I have to order them with one advisor as first and the other as second but each of them have their own special place. I choose the same order as that used in the papers that were submitted to show my gratitude towards my advisors Jean-Paul (Pablo) Ampuero and Nadia Lapusta. I need to thank them for the brand new MacBook pro they bought half-way through my PhD and for sending me to international conferences in countries that I never imagined I would step in.

Pablo has been a very hands-on advisor, especially in my early PhD days where I needed someone to be checking every minor thing I did. He gives a very critical review of work and taught me how to pay attention to details. His mentoring style has been unique. It enabled me to do independent research and take initiative, as well as taking charge of my work as I got closer and closer to completion of my graduate studies.

Nadia is one great human being who transmits enthusiasm and encouragement to her surroundings, including, but not limited to, her students. Her way of asking questions when a totally new topic is put forth inspires the confidence to face and understand out-of-field work and might even be able to offer solutions towards that end. I owe sincere and earnest thankfulness for the resources she provided when I was at a low time in life.

I would like to acknowledge the financial support of the Keck Institute for Space Studies (KISS) grant for this study and the Graduate Fellowship 2012 for the final

year.

I owe my deepest gratitude to Swaminathan (Swami) Krishnan and Jean-Philippe Avouac. Jean-Philippe agreed to serve on my committee at the last minute to replace a committee member who was on sabbatical. Jean-Philippe also advertised my work to the Keck audience which helped in receiving a KISS fellowship. Swami was also my advisor for my Masters. He had the course matrix all worked out on my first day at Caltech so that I didn't have to Figure out much in terms of getting my Master's degree by the end of the first year. I would also like to thank Tom Heaton, who served on my committee for candidacy.

I was working in a field that I did not have much background in. Several people helped me get up to speed with the geosciences topics. I enjoyed discussions with Hiroyuki Noda on dynamic ruptures, friction laws, and sometimes random philosophy of life. Carl Tape was the first one to introduce me to spectral element code, although Yoshi Kaneko later provided his version and explained several things in detail. Carl Tape, however, was still helping indirectly through his publications. Foundations for most of my work here on adjoint methods was only possible after reading his papers. Towards the final years, Zacharie Duputel shared his perspectives on source inversion. He also once helped me with moving for which he got a ticket! I had minimal interaction with my engineering colleagues but I'm indebted to Ahmed Elbanna, who made available his support in a number of ways. He was the one who suggested talking to Pablo while I was searching for PhD advisor.

Most of my works were run on supercomputing facilities. Even though I used external HPC clusters, the in-house Caltech computing systems admin Naveed Ansari needs a special mention here. A lot of time often went into installing the right dependencies required for the numerical simulation packages I ran and Naveed offered immediate help when required.

Last but not least, I am grateful to my Dad who made me believe in myself and for the undivided moral support he offered at every stage.

# Abstract

Inversions of earthquake source slip from the recorded ground motions typically impose a number of restrictions on the source parameterization, which are needed to stabilize the inverse problem with sparse data. Such restrictions may include smoothing, causality considerations, predetermined shapes of the local source-time function, and constant rupture speed. The best regional networks have sensor spacing in the tens of kilometers range, much larger than the wavelengths relevant to key aspects of earthquake physics. Novel approaches to providing orders-of-magnitude denser sensing include low-cost sensors (Community Seismic Network) and space-based optical imaging (Geostationary Optical Seismometer). This thesis aims to understand whether the inversion results could be substantially improved, with fewer constraints, by the availability of much denser sensor networks than currently available.

Inversions that involve large number of sensors and 3D crustal velocity models are intractable with the current source inversion codes. Hence we have developed a new approach that can handle thousands of sensors in heterogeneous media. It employs iterative conjugate-gradient optimization based on an adjoint method and involves iterative time-reversed 3D wave propagation simulations using the spectral element method (SPECFEM3D). We have also developed a variant of this adjoint-based method for layered media that utilizes pre-computed Green's functions instead of the time-reversed wave propagation. The developed methods have been applied to two problems: impact of crustal structure uncertainties on source inversion and resolution of rise time as a function of network spacing and rupture velocity. In the first part, we show that typical uncertainties in crustal velocity models represented by a von Karman distribution of 5 km correlation length and 5% standard deviation (with

Hurst exponent of zero), severely degrade the quality of source inversion. However, if the velocity uncertainties have a correlation of 500 m or a standard deviation of 1%, then source inversion has an adequate quality. In the second part we find that supershear ruptures show almost identical source recovery in terms of width of the slip pulse for network spacings ranging from few km to tens of km, even for rise times as short as 1 sec, while subshear ruptures require a network spacing finer than a penetration length that depends on rupture velocity and rise time, as their peak ground velocity decays rapidly with distance from the fault.

In summary, we have developed scalable source inversion tools that will enable exploiting the next generation of very dense earthquake observation systems, improvements in regional scale 3D tomography models and accelerated advancements in computing capabilities. These developments will be critical in resolving the fine spatio-temporal features of earthquake sources that are pertinent to fracture mechanics and earthquake physics. With the 3D iterative time-reversal imaging, one could aspire for extracting more information from the high-frequency wavefield by considering joint improvement of source and structure.

# Contents

<b>Acknowledgments</b>	<b>iv</b>
<b>Abstract</b>	<b>vi</b>
<b>1 Introduction</b>	<b>1</b>
1.1 Limitations of inversions using sparse datasets . . . . .	2
1.1.1 Real earthquakes . . . . .	2
1.1.2 Synthetic example . . . . .	2
1.2 Need for minimal constraints . . . . .	4
1.3 Physics-based vs. Kinematic source representation . . . . .	5
1.4 Classical methods for source inversion . . . . .	6
1.5 Adjoint methods for imaging . . . . .	7
1.6 Prerequisites to incorporate 3D media . . . . .	7
1.7 Unconventional earthquake observation systems . . . . .	8
1.8 Source imaging in other areas . . . . .	10
1.9 Outline of the thesis . . . . .	11
<b>2 Adjoint methods for finite-fault kinematic source inversion</b>	<b>12</b>
2.1 Statement of the source inversion problem . . . . .	12
2.2 Overview of the iterative procedure for source inversion . . . . .	14
2.3 Lagrangian formulation of the adjoint problem: Dirichlet boundary control problem . . . . .	17
2.4 Discrete formulation and model parametrization . . . . .	23
2.5 Higher-order representations do not preserve positivity . . . . .	24

2.6	Verification of the adjoint field computation . . . . .	26
2.7	Computational cost compared to pre-computed Green's functions approach . . . . .	27
2.8	Summary . . . . .	32
<b>3</b>	<b>Impact of crustal structure uncertainties on source inversion</b>	<b>33</b>
3.1	Reference inversions with known 3D velocity model . . . . .	33
3.2	Effect of uncertainties in the 3D velocity model on source recovery . .	37
3.3	Validity of our study for other rise times . . . . .	41
3.4	Summary . . . . .	43
<b>4</b>	<b>Rise-time resolution: Effect of network spacing and rupture velocity</b>	<b>44</b>
4.1	Problem formulation . . . . .	45
4.2	Model parametrization . . . . .	46
4.3	Green's functions . . . . .	46
4.4	Inversion method . . . . .	47
4.5	Benchmarking . . . . .	48
4.6	Resolution of rise time for pulse-like ruptures . . . . .	50
4.6.1	Problem setup . . . . .	50
4.6.2	Misfit metrics . . . . .	54
4.6.3	Effect of network spacing on resolving rise time . . . . .	58
4.6.4	Effect of rupture velocity on resolving rise time . . . . .	63
4.6.5	Rise-time resolvability for variable rupture speed . . . . .	69
4.7	Trade-off between noise and network spacing . . . . .	70
4.8	Summary . . . . .	71
<b>5</b>	<b>Conclusions</b>	<b>74</b>
<b>6</b>	<b>Recommendations for further research</b>	<b>76</b>
6.1	Complex kinematic scenarios . . . . .	76
6.1.1	Double pulse . . . . .	76

6.1.2	Back-propagating asperity . . . . .	78
6.1.3	Apparent supershear . . . . .	78
6.2	Dynamic shear rupture . . . . .	79
6.3	Trade-off between station spacing and noise . . . . .	81
6.4	ShakeOut scenario . . . . .	83
6.5	Tohoku-Oki earthquake . . . . .	84
6.6	Community Seismic Network . . . . .	87
6.7	Summary . . . . .	88
<b>A</b>	<b>Software development (SPECFEM3D)</b>	<b>91</b>
A.1	Parallelization and scalability of fault solver in SPECFEM3D . . . . .	91
A.2	Convergence analysis of SPECFEM3D for dynamic rupture . . . . .	94

# List of Figures

1.1	Source models for the 1999 Izmit earthquake in Turkey obtained by four different groups using their own inversion methods and data processing ( <a href="http://equake-rc.info/srcmod/">http://equake-rc.info/srcmod/</a> ). The inverted sources of different groups are clearly different. . . . .	3
1.2	Source models obtained by 9 different groups (bottom left) for the input source shown in top left recorded at stations shown by triangles in top right. Even a simple model such as MOD A that looks nothing like input shows good fit to the data (bottom right). (After <i>Mai et al.</i> [2007]).	4
1.3	Fault-parallel (left) and fault-normal (right) ground velocities from supershear (top) and sub-Rayleigh (bottom) scenarios . . . . .	9
1.4	Fault-parallel ground velocity from a supershear scenario: simulated (left), as seen by an optical telescope of 4-m diameter (middle) and 10-m diameter (right). The noise in the telescope data is due to a number of sources, including capturing the image for a finite time and atmospheric disturbances. . . . .	10
2.1	Sketch of the adjoint method illustrating the iterative procedure to update the source model using a forward and a time-reversed (adjoint) wave propagation simulation for each iteration. If only the first adjoint simulation is carried out, then the procedure is equivalent to time-reversal source imaging. . . . .	16

2.2	Root mean squared (RMS) error between data and synthetics as a function of the timestep of the temporal basis functions that discretize the slip velocity. The data is computed based on a very finely discretized source, to represent a continuum source. A timestep of 0.1 sec explains 99% of the data. . . . .	24
2.3	Comparison of the computational cost of the adjoint method based on the spectral element method (SEM) and the method with pre-computed Green's functions ("GF approach") for a typical $M_w$ 7.0 earthquake scenario with $40 \times 15$ km <sup>2</sup> rupture area, a 3D velocity model, data low-pass filtered below 1 Hz, fixed domain size extending up to approximately 2 fault lengths away from the source, and regular station spacing. The cost is normalized by the computational cost of SEM. The cost of the adjoint method does not depend on the number of stations, while the cost of the GF approach increases drastically until it becomes advantageous to exploit reciprocity to compute the Green's functions. . . . .	30
3.1	Spatial distribution of P-wave velocity ( $V_p$ ), normalized by its mean (5.6 km/s), on a cross section parallel to the fault plane for the three velocity models A, B and C (from top to bottom) with random heterogeneity described in Table 3.1. Histograms for each model are shown at the bottom. . . . .	35
3.2	Fault and station geometry for a $M_w$ 7 earthquake scenario in two hypothetical networks with (a) 20 km and (b) 1 km station spacing. The number of stations for each network is 88 and 32160, respectively. The fault ( $40$ km $\times$ $15$ km) is in the XZ-plane. The domain is symmetric with respect to the XZ-plane. Blue stars indicate station locations. The inset shows a zoomed portion of a $10$ km $\times$ $10$ km area. The number of stations in the inset is more than the total number of stations in the 20 km network. . . . .	36

3.3	Results from reference inversions. Data is generated in the 3D heterogeneous velocity model A and source inversion is performed assuming the same heterogeneous velocity model. The left column shows snapshots of input slip rate at three different times. The middle and right columns show inverted slip rate from the data of the 20 km network and the 1 km network, respectively. Note that the dense network allows for a better source recovery. It would be challenging for current source inversion codes and methodologies to do this inversion for the dense network with 32160 stations. . . . .	37
3.4	Same as Figure 3.3, with data generated in model A but now with source inversion based on the background homogeneous velocity model. The inverted slip pulses are distorted (bending in the dense network and widening of the pulse in the sparse network) compared to the reference inversions shown in Figure 3.3. . . . .	38
3.5	Same as Figure 3.4, but with data generated in model B (the source inversion still assumes the homogeneous background velocity model). The pulses recovered with the dense network are distorted while those of the sparse network are qualitatively similar to results of an inversion based on the true velocity model (not shown). . . . .	39
3.6	Same as Figure 3.4, but with data generated in model C. For both networks, the inverted pulses are qualitatively similar to the results of inversions based on the true velocity model (not shown). . . . .	39
3.7	Power spectrum of the three heterogeneous velocity models considered, normalized by the peak value of model A . . . . .	40
3.8	Effect of rise time on source inversions. Data is generated in model A and inversion assumes the homogeneous background velocity model. The description of the three columns is the same as that given in Figure 3.3. Each row shows a representative snapshot of slip rate for rise times 1 sec, 2 sec, 4 sec and 8 sec, respectively, top to bottom. The slip pulse is distorted in the dense network irrespective of rise time. . . . .	42

4.1	Geometry of the problem. The fault is indicated by red rectangle. Stations are shown in blue dots. . . . .	49
4.2	Comparison of the input slip rate and the inverted slip rate at three different times. (a) Inversion using our method. (b) Inversion shown in <i>Konca et al.</i> [2013]. In both cases first column shows input snapshots and second column shows inverted snapshots. Our inversion method seems to resolve equally well the slip rate visually, if not better, when compared with <i>Konca et al.</i> [2013]. . . . .	51
4.3	Comparison of the input final slip and the inverted final slip. (a) Inversion using our method. (b) Inversion shown in <i>Konca et al.</i> [2013]. In both cases top panel shows input slip and bottom panel shows inverted slip. Our inversion method does not seem to do well in terms of slip when compared with <i>Konca et al.</i> [2013] as we do not consider the GPS data. . . . .	52
4.4	Geometry of the problem setup for all the scenarios considered in the rise-time study. The station configuration is shown for 20 km station spacing but various network spacings are considered in this study. For a given network spacing, the closest station to the fault is as close as the spacing between stations. . . . .	53
4.5	Normalized variance as a function of iteration number. Denser networks produce more rapid reduction in normalized variance than a sparser network. . . . .	55
4.6	Normalized RMS error of slip rate as a function of iteration number. The RMS error in slip rate decreases more than 90% with denser networks performing better than coarser networks. . . . .	56
4.7	Normalized RMS error of slip rate in space. Coarser networks have a higher RMS error in the central region of the fault while the dense network has a uniform reduction of about 90% everywhere on the fault plane. . . . .	56

4.8	Normalized RMS error of slip rate as a function of time averaged over the entire fault plane. The dense network has only about 10% RMS error overall while the coarse network has approximately 50% RMS error during the time for which rupture lasts on the fault plane. . . . .	57
4.9	Normalized RMS error of slip as a function of iteration number. The RMS error in slip increases during the initial iterations eventually decreasing by an order of magnitude, with denser networks giving less RMS error than their coarser counterparts. . . . .	58
4.10	Normalized RMS error of slip in space. The spatial RMS error in slip is lower compared to the spatial RMS error in slip rate (Figure 4.7). . . .	59
4.11	Normalized RMS error of slip in time averaged over the entire fault plane. Errors in the final slip decrease with increasing network spacing.	59
4.12	Trade-off between network spacing and pulse width for a square Haskell pulse propagating at $V_r = 2$ km/s. Rows show inversions for different network spacings with bottommost row showing the input. Columns correspond to a representative snapshot from scenarios with rise times 0.5 sec, 1 sec, 1.5 sec, 2 sec, 2.5 sec, 3 sec, 3.5 sec, and 4 sec, respectively. Coarser networks have trouble resolving shorter rise times. . . . .	60
4.13	Trade-off between network spacing and pulse width for a Yoffe pulse propagating at $V_r = 2$ km/s. Rows show inversions for different network spacings with bottommost row showing the input. Columns correspond to a representative snapshot from scenarios with rise times 0.5 sec, 1 sec, 1.5 sec, 2 sec, 2.5 sec, 3 sec, 3.5 sec and 4 sec, respectively. Coarser networks have trouble resolving shorter rise times. . . . .	62
4.14	Contours of the ratio of the median rise-time estimates over the entire fault from the model to that of the input median rise time, for $V_r = 2$ km/s. Contour labeled 2 partitions the parameter space into two of which the top-left portion is unreliable. . . . .	63

4.15	Trade-off between network spacing and pulse width for a Yoffe pulse propagating at $V_r = 5$ km/s. Rows show inversions for different network spacings with the bottommost row showing the input. Columns correspond to a representative snapshot from scenarios with rise times 0.5 sec, 1 sec, 1.5 sec, 2 sec, 2.5 sec, 3 sec, 3.5 sec, and 4 sec, respectively. Coarser networks have trouble resolving shorter rise times. . . . .	64
4.16	Contours of the ratio of the median rise-time estimates over the entire fault to the rise time of the input for $V_r = 5$ km/s. . . . .	65
4.17	Trade-off between network spacing and rupture velocity for a square Haskell pulse with $T_r = 1$ sec. Rows show inversions for different network spacings with bottommost row showing the input. Columns correspond to a representative snapshot from the scenarios with rupture velocity 1 km/s, 1.5 km/s, 2 km/s, 2.5 km/s, 3 km/s, 3.5 km/s, 4 km/s, 4.5 km/s and 5 km/s, respectively. In the supershear regime, rise times are well resolved by all the networks while in the subshear regime a dense network is required to resolve the rise time better. . . . .	66
4.18	Peak ground velocity (PGV) as a function of distance from the fault for $T_r = 1$ sec Haskell pulse considering different rupture velocities. The supershear ruptures have near flat dependence of PGV with distance.	68
4.19	Contours of the ratio of the median rise-time estimates over the entire fault to rise time of input for $T_r = 1$ sec. For supershear rupture velocities, all the networks seem to resolve the rise time well except possibly for the 40 km network spacing. In the case of sub-Rayleigh rupture speeds, a network spacing smaller than a km is required to get a good estimate of the rise time. . . . .	68
4.20	Profiles of the final slip averaged along strike plotted as a function of depth for different rise times (left) $T_r=1$ sec and (right) $T_r=4$ sec. Depth averaged slip recovery is almost independent of the rise time. . . . .	69

- 4.21 Space-time plot of the slip rate at mid-depth to test variable rupture velocity. A scenario with 2 km/s rupture velocity in  $0 < x \leq 10$  km,  $20 < x \leq 30$  km and 2.5 km/s in  $10 < x \leq 20$  km,  $30 < x \leq 40$  km gives inversion comparable to an overall rupture speed of 2 km/s in the regions where rupture speed is 2 km/s and comparable to an overall rupture speed of 2.5 km/s in the regions where rupture speed is 2.5 km/s. . . . . 70
- 4.22 Slip rate snapshots from inversion with a noise of 1 cm/s added to the dense network data, and its comparison to its noiseless counterpart and a sparse network inversion for  $V_r = 3$  km/s. The recovery of the dense network with 1 cm/s noise added to its data is qualitatively similar the dense network recover without noise. . . . . 71
- 4.23 Slip rate snapshots from inversion with a noise of 1 cm/s added to the dense network data, and its comparison to its noiseless counterpart and a sparse network inversion for  $V_r = 2$  km/s. The recovery of the dense network with 1 cm/s noise added to its data is qualitatively similar the dense network recover without noise. . . . . 72
- 4.24 Slip rate snapshots from inversion for  $V_r = 2$  km/s and  $T_r = 1$  sec. Instead of having the network spacing as the closest distance from the fault, 20km-network is adjusted such that the closest stations are at a distance 4 km from the fault. Network spacing is the determining factor for the quality of inversion, but not the distance of the closest station to the fault. . . . . 73
- 6.1 Top panel shows the input double pulse scenario (first column) and inversions for it based on data from the coarse network (second column) and data from the dense network (third column) at three different times. Bottom panel shows depth averaged profiles of the amplitude of slip velocity along strike for each of these cases. Only inversion from the dense network shows two pulses clearly. Pulse width is 1.5 km and the gap between pulses is also 1.5 km. . . . . 77

6.2	The three columns show the input, inversion with the coarse network and inversion with the dense network, respectively. Pulse width and the gap between them are both 3 km. Inversion from the data of coarse network also shows signs of two pulses for 3 km gap between pulses which was not the case when the gap was 1.5 km (Figure 6.1). . . . .	78
6.3	The three columns show rupture process of the input, inversion from the coarse network data and inversion from the dense network data, respectively, at five different times. A semi-circular asperity in the top center of the fault ruptures backward with higher slip velocity. Only the inversion from dense dataset can identify the amplitude difference in the back-propagating pulse. . . . .	79
6.4	The three rows show the rupture process in space-time plots for the input, inversion from the coarse network data and inversion from the dense network data, respectively. The changes in speeds of individual pulses at regular intervals along strike is more evident in the dense dataset inversion. . . . .	80
6.5	A spontaneously propagating dynamic shear rupture shown at three different times (left). Inversion from the coarse dataset is shown in the middle column and inversion from the dense dataset is shown in the right column. . . . .	81
6.6	Inversions of a finely tuned double pulse scenario demonstrating that there is a certain pulse width and a certain gap below which the coarse dataset cannot predict that there are two pulses in the input while the dense dataset can show signs of two pulses even when the noise added to it has a signal to noise ratio of 10:1. . . . .	82
6.7	Domain for ShakeOut scenario showing shear-wave velocity ( $V_s$ ). The shallowest layers have a velocity of 600 m/s. . . . .	84

6.8	Source inversion of the ShakeOut scenario using data from the SCSN network (middle) and the data that would be provided by GSI (right). The input slip rate is shown at several time steps in left column. Data is low-pass filtered at 0.2 Hz before inversion. The 3D velocity model (SCEC CVM-H) of Southern California, with shallow layers having 600 m/s shear wave velocity, was used in the forward modeling as well as in the inversion. . . . .	85
6.9	Meshed domain for the Tohoku earthquake. The central region is meshed by 5 km elements with buffer zones surrounding it that progressively coarsen outward. . . . .	87
6.10	(a) Non-planar fault geometry of the Sierra Madre fault from the SCEC Community Fault Model (CFM). (b) A domain is constructed to encompass the fault and is meshed with hexahedral elements. . . . .	89
A.1	Results of strong scalability of SPECFEM3D with and without our fault implementation on CSCS' Cray XE6 system (Rosa), up to 8192 processors. The tests are based on the SCEC TPV5 benchmark. . . . .	93
A.2	Results of weak scalability of SPECFEM3D with our fault implementation on CSCS' Cray XE6 system (Rosa). The tests are based on the TPV205 benchmark with 50, 100 and 200 m average grid spacing. . . .	94
A.3	Results of weak scalability of SPECFEM3D with our fault implementation on CSCS' Cray XE6 system (Rosa). The tests are based on the TPV205 benchmark with 50, 100 and 200 m average grid spacing. ( <a href="http://scecddata.usc.edu/cvws/benchmark_descriptions.html">http://scecddata.usc.edu/cvws/benchmark_descriptions.html</a> ). . . . .	95
A.4	(a) RMS misfits final slip (blue) and peak slip rate (black) as a function of grid size (b) RMS misfits rupture time as a function of grid size. Dotted line shows timestep. . . . .	96

# List of Tables

3.1	Parameters of the three random velocity models (A, B and C) with von Karman correlation function . . . . .	34
4.1	Various sets of scenarios examined. Yoffe and Haskell pulses are both tested for various rise times and network spacings in the subshear case. The same setup is used to repeat the supershear case for Yoffe pulse. Fixing the rise time, the rupture velocity dependency is examined using a Haskell pulse. Finally, noise is added to dense network for end-member cases of rupture velocity and for a fixed rise time. . . . .	53

# Chapter 1

## Introduction

Earthquakes represent a large portion of the global natural hazard. In an earthquake, a stressed out portion of the Earth releases the stored strain energy, displacing the crust in opposite directions across a discontinuity. The resulting shaking is measured on the surface of the Earth using instruments like accelerometers. The recordings are in turn used to explain what happened inside the Earth by formulating an inverse problem.

Earthquake source inversion is the process of inferring the spatio-temporal distribution of slip rate on an assumed fault surface from a combination of seismological, geodetic, remote sensing, tsunami and field observations. The inferred source parameters inform fundamental studies in earthquake physics and applied studies in earthquake engineering. Strong ground motions near active faults, a key input for earthquake hazard assessment, are greatly affected by the details of the source rupture process. The design of source rupture models for future earthquakes is guided by the slip models inferred for past earthquakes. Valuable constraints on earthquake rupture processes can in principle be derived from ground motion recordings. In particular, only seismological data provides a window into the time-dependency of the rupture process.

## 1.1 Limitations of inversions using sparse datasets

### 1.1.1 Real earthquakes

Inversions of earthquakes with few recordings are found to be inconsistent across source inversion modeling groups [Beresnev, 2003] even when the same approach (e.g., *Olson and Apsel*, 1982 and *Hartzell and Heaton*, 1983 for 1979 Imperial Valley earthquake) is used. These discrepancies arise due to subjective decisions made on kinematic parameters and stabilizing constraints.. An example of a poorly recorded earthquake where different groups produced widely different source models is the 1999 Izmit earthquake in Turkey. *Beresnev* [2003] found little resemblance among five published source models of this earthquake [*Bouchon et al.*, 2002; *Delouis et al.*, 2002; *Gülen et al.*, 2002; *Li et al.*, 2002; *Sekiguchi and Iwata*, 2002] in terms of asperity locations and slip distribution (Figure 1.1). The 1999 Chi-Chi earthquake in Taiwan was recorded by a few hundred of stations [*Lee et al.*, 2001]. *Ide et al.* [2005] compared four published source models of this event [*Ma et al.*, 2001; *Chi et al.*, 2001; *Yu et al.*, 2001; *Zeng and Chen*, 2001] and found that they are very similar in terms of rupture length, width, duration and propagation velocity. Despite the differences in the assumed velocity structure and modeling approaches, the dense distribution of the Chi-Chi earthquake dataset enabled robust constraints on first- and second-order source parameters.

### 1.1.2 Synthetic example

A group of source inversion modelers from various countries took the initiative to validate their codes and understand the limitations of their methods. The effort was led by Martin P. Mai as the SPICE (Seismic wave Propagation and Imaging in Complex media: a European network) BlindTest which later evolved into the Source-Inversion Validation (SIV) project (<http://equake-rc.info/sivdb/wiki/>). The modelers were provided with noise-free data but were not given any information about the input source. The velocity-density structure together with hypocentral depth,

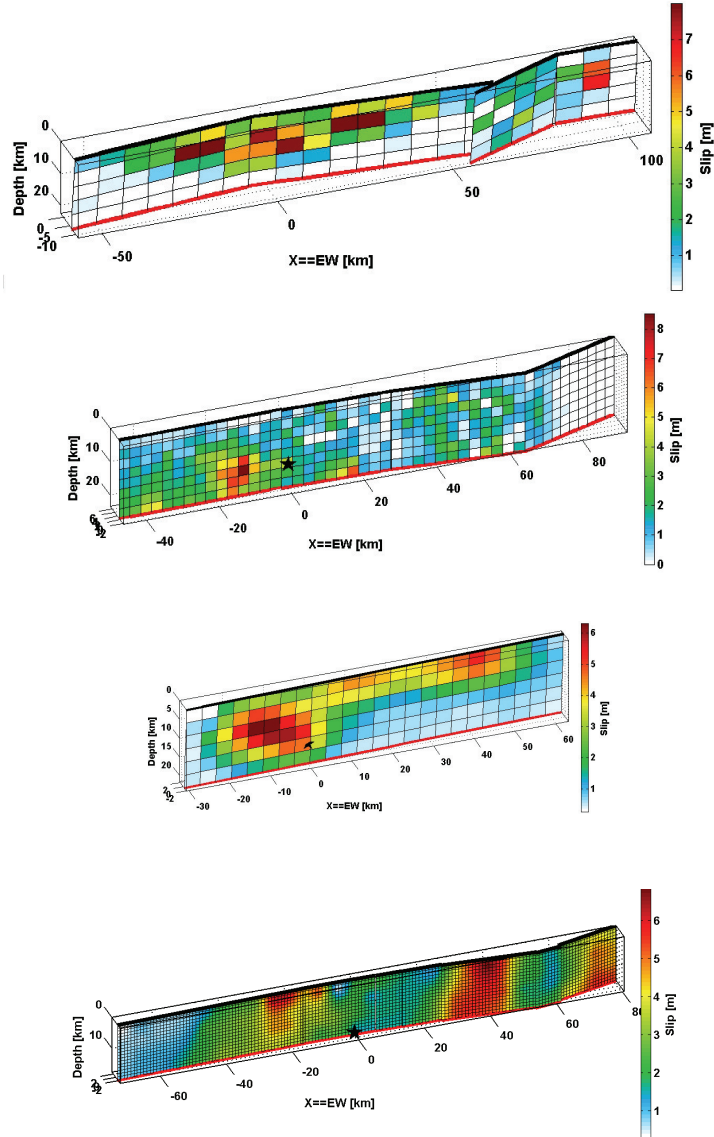


Figure 1.1: Source models for the 1999 Izmit earthquake in Turkey obtained by four different groups using their own inversion methods and data processing (<http://equake-rc.info/srcmod/>). The inverted sources of different groups are clearly different.

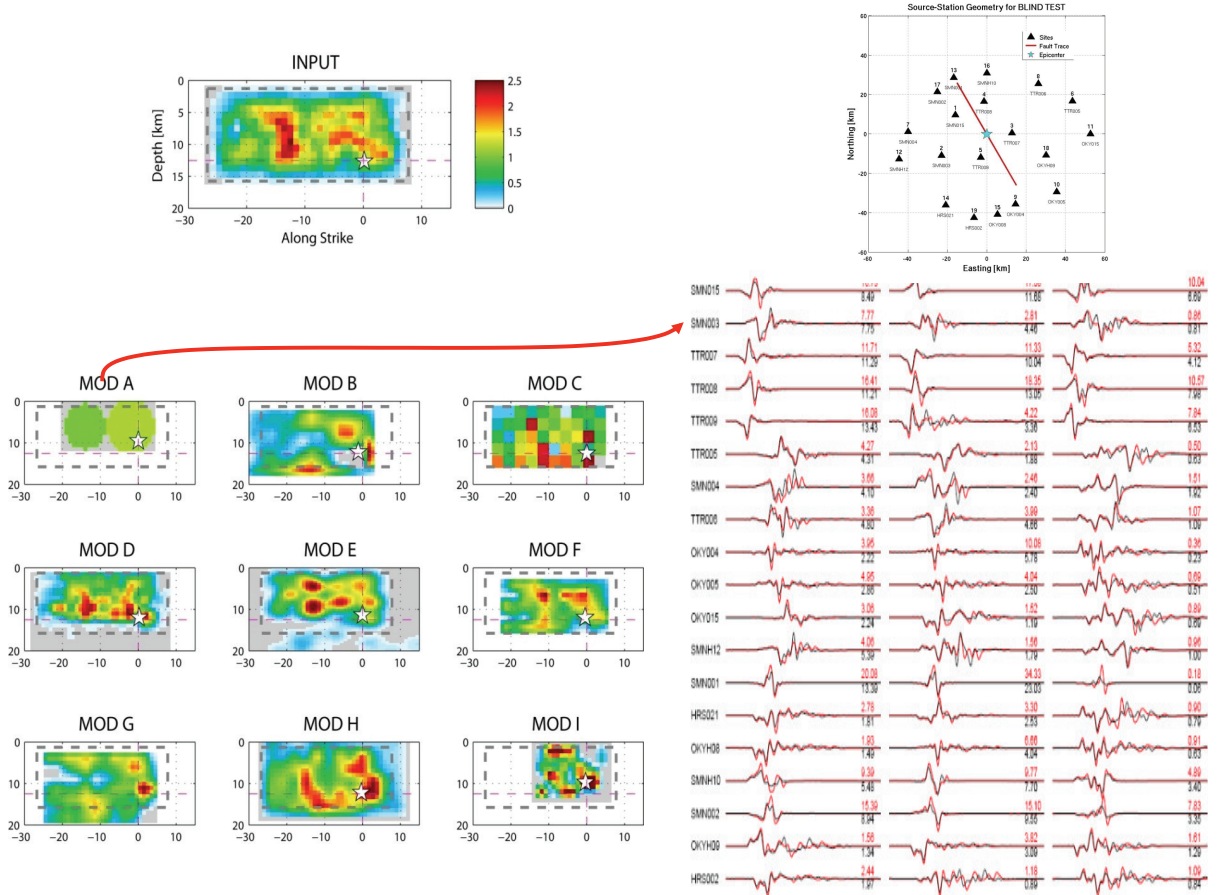


Figure 1.2: Source models obtained by 9 different groups (bottom left) for the input source shown in top left recorded at stations shown by triangles in top right. Even a simple model such as MOD A that looks nothing like input shows good fit to the data (bottom right). (After *Mai et al.* [2007]).

seismic moment, strike, dip and rake were provided to compute Green's functions. Nine groups participated in this BlindTest. While some of the inverted source models had about 90% correlation with the input, four of them were statistically no different from a random model but still fit the data quite well (Figure 1.2).

## 1.2 Need for minimal constraints

The discrepancies in the source models seen in Section 1.1 arise from subjective decisions made on kinematic parameters and stabilizing constraints. Additional constraints are typically imposed on source inversions, including total seismic moment,

minimum norm, minimum roughness, positivity or bounds on rupture speed and rise time. Some of these constraints have a strong physical basis. For instance, constraining rupture speed to be slower than the P-wave speed naturally enforces the causality principle if the hypocenter location is assumed. In contrast, constraints on rise time are usually motivated by the desire to reduce the number of unknowns in order to mitigate the non-uniqueness of the inverse problem, rather than by known physical bounds on rise time. Dynamic rupture simulations show that earthquakes can produce a wide variety of behaviors depending on initial conditions and friction parameters [Gabriel *et al.*, 2012]. One example of such complexity is the occurrence of rupture reversals, i.e., rupture propagation in the direction opposite to that of the ongoing rupture, as was suggested for the 2010 El Mayor-Cucapah earthquake (<http://www.scec.org/meetings/2011am/emc.html>) and for the 1984 Morgan Hill earthquake [Beroza and Spudich, 1988]. Another example is the occurrence of multiple pulses (repeated slip) during the 2011 Tohoku earthquake inferred by Lee *et al.* [2011]. Capturing such complex rupture processes requires a flexible parameterization with minimal constraints. We, therefore, derive a method here that does not assume any particular properties of the sources, aside from the knowledge of the rupture plane. Additionally, we avoid all sorts of constraints thereby allowing the data to dictate how rupture evolved.

### 1.3 Physics-based vs. Kinematic source representation

Elastodynamic equations together with fault friction laws are used to construct physics-based models of earthquakes. This approach uses fault constitutive laws derived from laboratory experiments, but the scaling of friction parameters from laboratory to natural fault scales is not well understood. Attempts to invert for dynamic source parameters [Peyrat *et al.*, 2004] from seismological observations have had limited success. Kinematic inversions [e.g., Wald and Graves, 2001; Liu and Archuleta, 2004; Beres-

*nev and Atkinson, 2002*], on the other hand, are well studied using various kinds of optimization methods although they are not physics based. Kinematic source models usually assume that rupture starts from a point on the fault known as hypocenter that is inferred from arrival times of direct P- and S-waves. Nucleating from hypocenter, rupture propagates at a fixed or variable speed known as rupture speed. The ruptured region creates a finite offset across the fault plane termed slip. The duration for which rupture occurs is usually much larger than the time for which any chosen portion of the fault slips, also known as “rise time” [*Heaton, 1990*]. To characterize kinematic rupture models, the rise time of each patch that constitutes the fault is required along with the rupture velocity and slip of that patch. The temporal evolution of slip on each patch is described by a slip-time function that depends on rise time.

## 1.4 Classical methods for source inversion

Seismograms can be expressed as the sum of the contributions from all fault patches. Each fault patch contributes its slip-rate function convolved by a Green’s function. The classification of inversion approaches comes from the kind of assumptions inversion modelers make on the temporal evolution of slip. Allowing for variable rupture speeds leads to a nonlinear formulation of the inverse problem [*Ji et al., 2002; Liu and Archuleta, 2004*] and it is typically done in conjunction with assuming the shape of the slip-time function, to reduce the number of free parameters.. Although great care is taken to choose slip-time functions that are similar to those of dynamic rupture modeling, the assumption of the same slip time function on all fault patches is highly simplified [*Shao and Ji, 2012*]. Formulated in the wavelet domain [*Ji et al., 2002*] or time domain [*Hartzell and Heaton, 1983*], these methods rely on a class of global optimization methods like simulated annealing [*Sen and Stoffa, 1991*] or genetic algorithms [*Sambridge and Drijkoningen, 1992*]. In addition to the assumption on slip-time function, the work of *Ji et al. [2002]* also assumes bounds on the starting-phase time ( $t_s$ ) and ending-phase time ( $t_e$ ) which determine rise time ( $t_s+t_e$ ). The other class of methods that treats the timing of rupture as known by an assumption

on rupture velocity and inverts for potency in a certain number of temporal bins. Such methods are known as multi-time window [Olson and Apsel, 1982; Hartzell and Heaton, 1983] methods. Often, these methods use linear least-square optimization [Menke, 1989] to solve the inverse problem. Constraints like non-negativity lead to loss of linearity and require specialized methods such as non-negative least-squares [Lawson and Hanson, 1995] to obtain a solution. To analyze small-scale features such as nucleation simultaneously with the large-scale rupture process, Uchide and Ide [2007] proposed a multiscale inversion model renormalizing the slip-rate distribution on different scales.

## 1.5 Adjoint methods for imaging

Adjoint methods [Tarantola, 1984] have been in use in seismology for tomography [Tromp et al., 2005; Tape et al., 2010; Fichtner et al., 2010; Liu and Tromp, 2008; Askan and Bielak, 2008], point-source moment-tensor inversion [Hjörleifsdóttir et al., 2007; Kim et al., 2011] and joint inversion of finite source and tomography in 2D [Akcelik et al., 2006]. The adjoint fields are related to time-reversal imaging [Kawakatsu and Montagner, 2008]. Attempts to achieve finite-fault source imaging through time reversal were unsuccessful in resolving rupture details [Kremers et al., 2011]. Here, we present a method for source inversion based on adjoint methods, iteratively updating the source model through time-reversal simulations. We show that the gradient of the cost function with respect to slip rate is given by the tractions on the locked fault plane in the adjoint problem. This is different from moment tensor (density) source inversion [Kremers et al., 2011; Hjörleifsdóttir et al., 2007], for which the adjoint fields are strains.

## 1.6 Prerequisites to incorporate 3D media

Earthquake source inversion is typically performed with Green’s functions computed under the assumption of a horizontally layered crust. Waves propagating through a

3D medium are scattered as they reach the surface and imaging source properties with such scattered datasets produces blurred models. Lateral heterogeneity is accounted for only approximately, for instance, through station correction factors [Shao *et al.*, 2012] or through station-specific layered models [Liu *et al.*, 2006; Asano and Iwata, 2009]. Graves and Wald [2001] showed that incorporating well calibrated 3D Green’s functions provides a better reconstruction of the source. The development of 3D crustal velocity models is in steady progress. In Southern California, wave propagation simulations based on the SCEC CVM-H model are consistent with observed waveforms down to a period of approximately 2 seconds [Tape *et al.*, 2009]. However, for dense seismic networks and fine resolution source parameterizations, the computation and storage of 3D Green’s functions can be prohibitively demanding, and an alternative approach for source inversion is desirable. The methodology presented here provides such an approach and allows us to study finite earthquake sources when a 3D velocity model of the region is adequately known. Our formulation also permits exploring the effects of uncertainties in the velocity model on source inversion.

## 1.7 Unconventional earthquake observation systems

Earthquake source imaging suffers from limited resolution due to the spatial sparsity of data provided by current seismic networks. To distinguish between predictions of competing earthquake-physics models, we need the source resolution on scales smaller than 1 km. Yet seismometers in currently deployed networks are located tens of kilometers from each other, and inversions of their data need to be dramatically smoothed to yield stable and convergent results. The source inversion problem with sparse data is severely non-unique and its regularization requires dramatic assumptions on rupture kinematics that restrict the range of earthquake physics that can be unveiled. Densifying seismic networks is one path towards more reliable source imaging. Ideally, a spatial resolution finer than the wavelengths exploited in the source inversion would capture an unaliased picture of the wavefield. Block-by-block networks of low-cost MEMS sensors [Clayton *et al.*, 2012] could soon provide ground motion

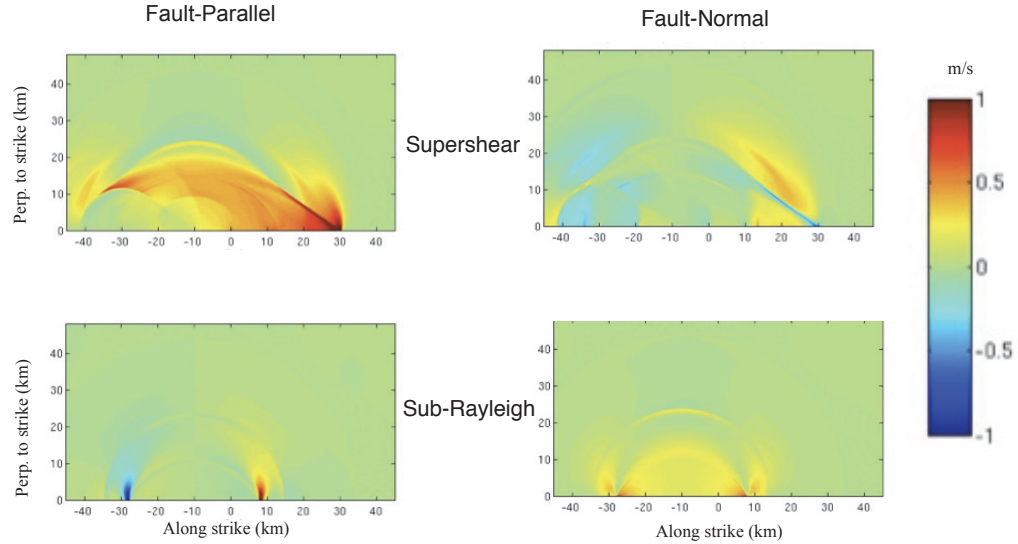


Figure 1.3: Fault-parallel (left) and fault-normal (right) ground velocities from supershear (top) and sub-Rayleigh (bottom) scenarios

recordings at every few hundreds of meters in urban areas. Emergent concepts for space-based earthquake observation systems [Michel *et al.*, 2013] could expand such dense coverage to remote areas.

The dense set of observations from Geostationary Seismic Imager (GSI) can give clues about the source characteristics, such as rupture speed, without actually having to perform an inversion. For instance, one can distinguish supershear rupture from subshear rupture just by the signature feature Mach cone that is visible in supershear ruptures (Michel *et al.*, 2013, Figure 1.3). Though the particle velocities shown in Figure 1.3 are from the simulated ground motion, these features are also evident (Figure 1.4) in the velocities processed to emulate as they would be seen from the optical seismometer.

The use of these innovative dense observational systems for the large earthquakes source imaging is very challenging for several reasons. First, the high sensitivity of these dense networks to shallow heterogeneities requires the ability to simulate accurately the propagation of seismic waves in a 3D Earth, which is computationally expensive. Second, the large amount of data increases the difficulty to handle this problem because of the required memory and processing power. Current inversion

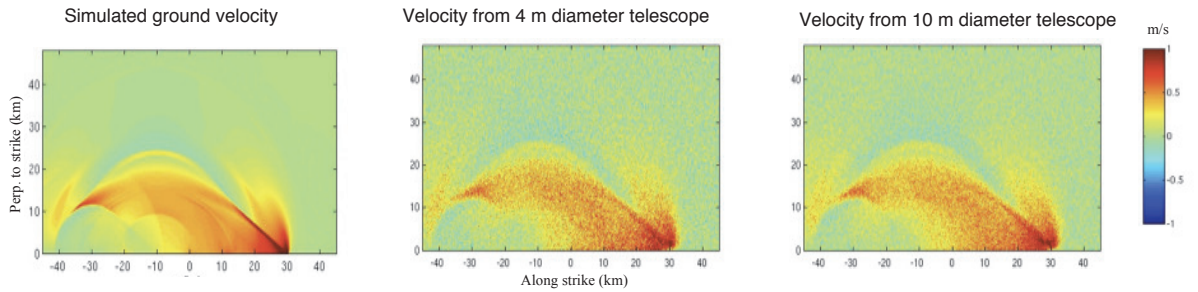


Figure 1.4: Fault-parallel ground velocity from a supershear scenario: simulated (left), as seen by an optical telescope of 4-m diameter (middle) and 10-m diameter (right). The noise in the telescope data is due to a number of sources, including capturing the image for a finite time and atmospheric disturbances.

codes cannot handle such vast amounts of data. A scalable source inversion code that can help us better understanding the space-time evolution of earthquake rupture, while handling the substantial amount of data provided by a next-generation Earth observatory systems, can bring a paradigm shift in earthquake seismology. The development of such approach is a goal of this thesis.

## 1.8 Source imaging in other areas

Although the source imaging technique described here is in the context of seismic source, it may be applicable in various other fields. One example comes from structural engineering. Brittle fractures in welded beam-column connections of steel moment-resisting frames (MRFs) are detected by solving an inverse problem (provide citation), and our method may help in dealing with increasingly larger number of sensors used for structural monitoring. Localizing the sources in human brain activity through electroencephalography (EEG) involves solving an inverse problem to invert for the spatio-temporal details of large-scale neuronal circuits, forming an important tool in cognitive and clinical neurosciences [Brodbeck *et al.*, 2011], and the method developed in this work may help in this area as well. .

## 1.9 Outline of the thesis

In summary, the developments of this thesis build towards addressing the following question: How to perform efficiently seismic source inversion based on dense seismological datasets and minimal prior assumptions on the source? In Chapter 2, a Lagrangian based PDE-constrained optimization method is presented and an analytical expression for the gradient of cost function with respect to the model is derived. Using a 3D wave propagation code based on spectral element method, an inversion scheme is developed combining the adjoint problem with the forward problem. Choosing a rise time of 1 sec, the resolvability of pulses is qualitatively tested with a dense (1 km station spacing) and a coarse (20 km station spacing) network for various von Karman distributed 3D heterogeneous models and an explanation about qualitative recovery is presented using the power spectra of von Karman distributions in Chapter 3. In Chapter 4, the “adjoint linear source inversion” with “unrestricted multi-time window” parametrization is outlined and benchmarked with an example in comparison to an existing widely used nonlinear source inversion method. Equipped with this hybrid inversion scheme, the rise-time resolvability is tested for various network spacing ranging from 2 km to 40 km. A range of values are chosen for the rise time and the rupture velocity to establish quantitatively the rise times resolvable by a given network spacing. Chapter 5 shows how to combine the separately obtained results for homogeneous velocity models (Chapter 4) and heterogeneous velocity models (Chapter 3) to arrive at an understanding of rise time resolvability for complex source embedded in complex velocity model. Chapter 6 provides future directions in which this work can be extended.

## Chapter 2

# Adjoint methods for finite-fault kinematic source inversion

### 2.1 Statement of the source inversion problem

We aim at inferring the spatio-temporal distribution of slip velocity on an assumed fault surface from ground motion data recorded at or near the Earth’s surface. The data comprises three-component ground velocity timeseries  $\dot{\mathbf{d}}(\mathbf{x}_r, t)$  recorded at a set of  $n$  receiver locations  $\mathbf{x}_r$  between the initiation of rupture at  $t = 0$  and a final recording time  $t = T$ . The model comprises the two-component slip velocity time series  $\mathbf{m}(\mathbf{x}, t)$  at all points  $\mathbf{x}$  on the fault surface  $\Sigma$ . The fault geometry is assumed and the fault normal component of slip is assumed to be zero (shear faulting). We use the term “synthetics” and the notation  $\dot{\mathbf{s}}(\mathbf{x}_r, t, \mathbf{m})$  to denote ground velocities computed at receiver location  $\mathbf{x}_r$  based on source model  $\mathbf{m}$ . The synthetic time series and the model parameters are linearly related by a partial differential equation, the seismic wave equation, or equivalently by a representation theorem (e.g., 3.2 of *Aki and Richards*, 2002). We concisely write this relation as

$$\dot{\mathbf{s}} = \mathbf{G} \mathbf{m} \tag{2.1}$$

where  $\mathbf{G}$  is a linear operator from model space to data space. We seek a model that reproduces the observed wavefield,  $\dot{\mathbf{s}}(\mathbf{m}) \approx \dot{\mathbf{d}}$  in a sense that will be made precise now.

Waveform data is usually low-pass filtered prior to earthquake source inversion in order to downweight those high-frequency components of the wavefield that cannot be well predicted based on available crustal velocity models, which are usually relatively coarse. We denote by  $h(t)$  the impulse time response of the filter, by  $f_c$  its cut-off frequency and by  $*$  the convolution operation between two timeseries. We define a cost function  $\chi$  that quantifies the misfit between filtered data and synthetics:

$$\chi(\mathbf{m}) = \frac{1}{2} \int_0^T \sum_{r=1}^{N_{sta}} W_r \left\| h(t) * \left( \dot{\mathbf{s}}(\mathbf{x}_r, t, \mathbf{m}) - \dot{\mathbf{d}}(\mathbf{x}_r, t) \right) \right\|^2 dt \quad (2.2)$$

where  $W_r$  is a data weight for the receiver located at  $\mathbf{x}_r$  and  $\|\cdot\|$  is the 3D Euclidian norm. Defining a dot product in the data space,  $\langle \cdot, \cdot \rangle$ , that incorporates the weights  $W_r$  and the filter  $h$ , we concisely write the cost function in terms of the associated data space norm,  $\|\cdot\|$ :

$$\chi(\mathbf{m}) = \frac{1}{2} \|\dot{\mathbf{s}}(\mathbf{m}) - \dot{\mathbf{d}}\|^2 \quad (2.3)$$

Our goal is to find the source model  $\mathbf{m}$  that minimizes the cost function  $\chi$ , subject to Equation 2.1. The optimal model in this classical least-squares problem is the solution of the so-called normal equations:

$$\mathbf{G}^\dagger \mathbf{G} \mathbf{m} = \mathbf{G}^\dagger \mathbf{d} \quad (2.4)$$

where  $\mathbf{G}^\dagger$  is the adjoint operator of  $\mathbf{G}$ , defined as the linear operator from data space to model space that satisfies the relation

$$\langle \mathbf{d}', \mathbf{G} \mathbf{m}' \rangle = \langle \mathbf{G}^\dagger \mathbf{d}', \mathbf{m}' \rangle \quad (2.5)$$

for any arbitrary data  $\mathbf{d}'$  and model  $\mathbf{m}'$ . The right hand side involves the natural dot product in model space.

Upon discretization of the space and time dimensions, this leads to the classical linear formulation of the source inversion problem [e.g., *Hartzell and Heaton, 1983*], in which the unknowns are the slip rates at each fault cell and on multiple time

windows. In standard practice, the slip velocity unknowns are restricted to time intervals much shorter than the whole rupture duration. At each fault location these intervals are dictated by assumed bounds on rupture speed and rise time. Some of these additional constraints have a strong physical basis. For instance, constraining rupture speed to be slower than the P-wave speed naturally enforces the causality principle if the hypocenter location is assumed. However, constraints on rise time are motivated by a desire to reduce the number of unknowns in order to mitigate the non-uniqueness of the inverse problem, rather than by known physical bounds on rise time. In contrast to standard practice, we consider the values of slip velocity at every instant as unknowns. This allows for any fault location to rupture multiple times and for the inversion to capture complex rupture histories that are physically admissible, e.g., secondary rupture fronts running in the opposite direction as the main front.

## 2.2 Overview of the iterative procedure for source inversion

We solve the normal equations (2.4) by applying a standard iterative algorithm, the conjugate-gradient (CG) method. The algorithm is detailed below and shown pictorially in Figure 2.1.

1. Initialize the iteration counter,  $k = 0$
2. Assume an initial model,  $\mathbf{m}^0$ , and compute the corresponding synthetics,  $\mathbf{s}^0 = \mathbf{G} \mathbf{m}^0$
3. Compute residuals by subtracting synthetics from data,  $\mathbf{r}^0 = \mathbf{s}^0 - \mathbf{d}$
4. Compute the gradient of the cost function with respect to the model parameters,  $\boldsymbol{\gamma}^0 = \mathbf{G}^\dagger \mathbf{r}^0$
5. Set the search direction,  $\mathbf{p}^0 = -\boldsymbol{\gamma}^0$
6. Compute new synthetics,  $\mathbf{s}^k = \mathbf{G} \mathbf{p}^k$

7. Update the model such that the cost function is minimized along the search direction,  $\mathbf{m}^{k+1} = \mathbf{m}^k + \alpha \mathbf{p}^k$  where  $\alpha = \langle \mathbf{r}^k, \mathbf{s}^k \rangle / \langle \mathbf{s}^k, \mathbf{s}^k \rangle$
8. Update the residuals,  $\mathbf{r}^{k+1} = \mathbf{r}^k + \alpha \mathbf{s}^k$
9. Compute the new gradient,  $\boldsymbol{\gamma}^{k+1} = \mathbf{G}^\dagger \mathbf{r}^{k+1}$
10. Update the search direction applying the Polak-Ribiere formula,  $\mathbf{p}^{k+1} = -\boldsymbol{\gamma}^{k+1} + \beta \mathbf{p}^k$  where  $\beta = \langle \boldsymbol{\gamma}^{k+1} - \boldsymbol{\gamma}^k, \boldsymbol{\gamma}^{k+1} \rangle / \langle \boldsymbol{\gamma}^k, \boldsymbol{\gamma}^k \rangle$
11. If the norm of the new search direction,  $\mathbf{p}^{k+1}$ , is less than a prescribed tolerance stop. Otherwise increment the iteration counter,  $k \leftarrow k + 1$ , and go to step 6.

The inverse problem of earthquake source retrieval from ground motions recorded over a limited region of the Earth’s surface generally suffers from non-uniqueness. The particular solution to which the CG algorithm converges depends on the choice of the initial guess. Here we set  $\mathbf{m}^0 = 0$ . With this choice, the CG algorithm is known to converge to the minimum-norm solution. This choice is not motivated by physical considerations on the rupture process, but rather by the insight it provides on the intrinsic uncertainties of the source inversion problem: the minimum-norm solution is orthogonal to the null space of the inverse problem, hence it isolates that part of the earthquake rupture that is “visible” by a given dataset.

In our implementation, steps 2 and 6 involve a wave propagation simulation with prescribed kinematic source. In the next Section we show that steps 4 and 9 can be efficiently accomplished by a wave propagation simulation with time-reversed ground motion residuals applied as point forces at the receivers. In that back-propagation simulation the fault plane is locked and the gradient of the cost function is obtained as the fault tractions. In summary, each iteration requires one forward-propagation simulation (during model update, step 6) and one back-propagation simulation (during gradient update, step 9).

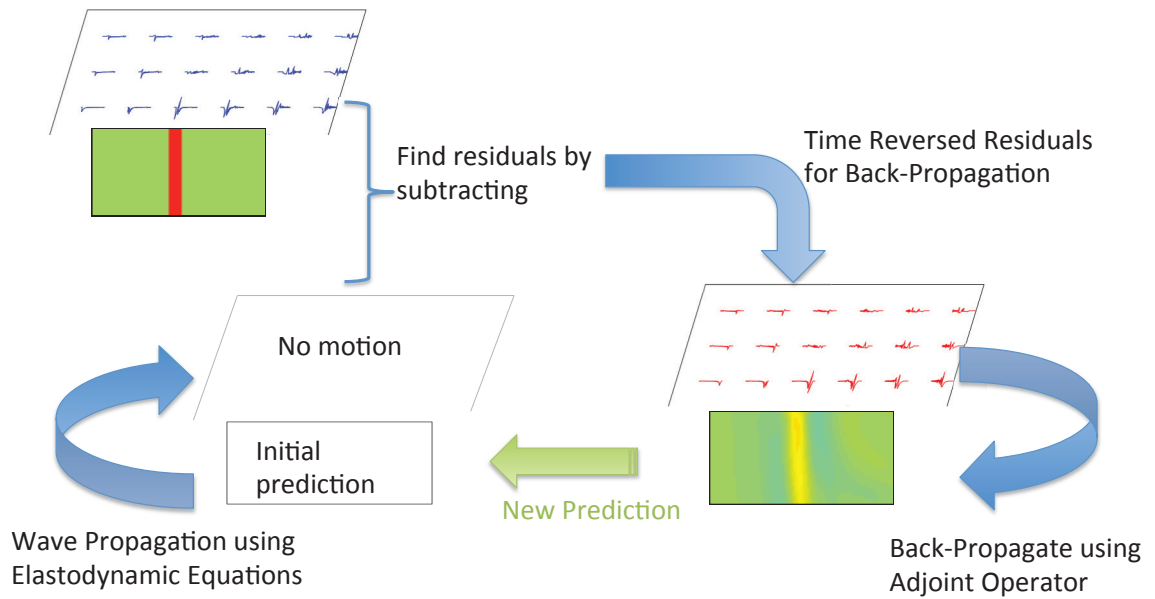


Figure 2.1: Sketch of the adjoint method illustrating the iterative procedure to update the source model using a forward and a time-reversed (adjoint) wave propagation simulation for each iteration. If only the first adjoint simulation is carried out, then the procedure is equivalent to time-reversal source imaging.

## 2.3 Lagrangian formulation of the adjoint problem: Dirichlet boundary control problem

For the problems we are interested in, the most efficient way to compute the gradient of the cost function with respect to the source model is by solving an adjoint problem. We use a Lagrangian formulation modified from that presented by *Liu and Tromp* [2006]. We formulate the Lagrangian based on filtered residuals. Simulations are done on a bounded domain  $\Omega$ , whose boundary comprise a free surface  $\partial\Omega_1$  and an absorbing boundary  $\partial\Omega_2$ . We denote by  $\rho$  the density and  $\mathbf{C}$  the fourth-order elastic stiffness tensor of the crust. These material properties can be spatially non uniform. The Lagrangian is given by

$$\begin{aligned} \mathcal{L}(\dot{\mathbf{s}}, \mathbf{m}, \boldsymbol{\mu}, \lambda) = & \frac{1}{2} \int_0^T \sum_{r=1}^{N_{sta}} W_r \left[ h(t) * \left( \dot{\mathbf{s}}(\mathbf{x}_r, t, \mathbf{m}) - \dot{\mathbf{d}}(\mathbf{x}_r, t) \right) \right]^2 dt \\ & - \int_0^T \int_{\Omega} \boldsymbol{\lambda} \cdot (\rho \partial_t^2 \mathbf{s} - \nabla \cdot (\mathbf{C} : \nabla \mathbf{s})) d^3 \mathbf{x} dt \\ & + \int_0^T \int_{\Sigma} \boldsymbol{\mu} \cdot (\dot{\mathbf{s}}_+ - \dot{\mathbf{s}}_- - \mathbf{m}) d^2 \mathbf{x} dt \end{aligned} \quad (2.6)$$

where  $\boldsymbol{\lambda}$  and  $\boldsymbol{\mu}$  are Lagrange multipliers and  $\dot{\mathbf{s}}_+$  and  $\dot{\mathbf{s}}_-$  are the velocity fields on each side of the fault.

We seek  $\dot{\mathbf{s}}, \mathbf{m}, \boldsymbol{\lambda}$  and  $\boldsymbol{\mu}$  such that the Lagrangian  $\mathcal{L}$  is minimized. A necessary condition is stationarity of the Lagrangian with respect to its four arguments:

$$d\mathcal{L}(\dot{\mathbf{s}}, \mathbf{m}, \boldsymbol{\mu}, \lambda) = 0 = \frac{\partial \mathcal{L}}{\partial \dot{\mathbf{s}}} \delta \dot{\mathbf{s}} + \frac{\partial \mathcal{L}}{\partial \mathbf{m}} \delta \mathbf{m} + \frac{\partial \mathcal{L}}{\partial \boldsymbol{\lambda}} \delta \boldsymbol{\lambda} + \frac{\partial \mathcal{L}}{\partial \boldsymbol{\mu}} \delta \boldsymbol{\mu} \quad \forall \delta \dot{\mathbf{s}}, \delta \mathbf{m}, \delta \boldsymbol{\lambda}, \delta \boldsymbol{\mu} \quad (2.7)$$

This implies

$$0 = \frac{\partial \mathcal{L}}{\partial \dot{\mathbf{s}}} \delta \dot{\mathbf{s}} = \frac{\partial \mathcal{L}}{\partial \mathbf{s}} \delta \mathbf{s} \quad \forall \delta \dot{\mathbf{s}}, \forall \delta \mathbf{s} \quad (2.8)$$

$$0 = \frac{\partial \mathcal{L}}{\partial \mathbf{m}} \delta \mathbf{m} \quad \forall \delta \mathbf{m} \quad (2.9)$$

$$0 = \frac{\partial \mathcal{L}}{\partial \boldsymbol{\lambda}} \delta \boldsymbol{\lambda} \quad \forall \delta \boldsymbol{\lambda} \quad (2.10)$$

$$0 = \frac{\partial \mathcal{L}}{\partial \boldsymbol{\mu}} \delta \boldsymbol{\mu} \quad \forall \delta \boldsymbol{\mu} \quad (2.11)$$

We now examine these four conditions sequentially. The first stationarity condition is

$$\begin{aligned} 0 = \frac{\partial \mathcal{L}}{\partial \dot{\mathbf{s}}} \delta \dot{\mathbf{s}} &= \int_0^T \int_{\Omega} \sum_r W_r \left[ h(t) * \left( \dot{\mathbf{s}}(\mathbf{x}_r, t, \mathbf{m}) - \dot{\mathbf{d}}(\mathbf{x}_r, t) \right) \right] \delta(\mathbf{x} - \mathbf{x}_r) \cdot h(t) * \delta \dot{\mathbf{s}} d^3 \mathbf{x} dt \\ &\quad - \int_0^T \int_{\Omega} \boldsymbol{\lambda} \cdot [\rho \partial_t^2 \delta \mathbf{s} - \nabla \cdot (\mathbf{C} : \nabla \delta \mathbf{s})] d^3 \mathbf{x} dt \\ &\quad + \int_0^T \int_{\Sigma} \boldsymbol{\mu} \cdot (\delta \dot{\mathbf{s}}_+ - \delta \dot{\mathbf{s}}_-) d^2 \mathbf{x} dt \end{aligned} \quad (2.12)$$

Integrating by parts the spatial and temporal derivatives we obtain, after some

algebra,

$$\begin{aligned}
0 = \frac{\partial \mathcal{L}}{\partial \dot{\mathbf{s}}} \delta \dot{\mathbf{s}} &= \int_0^T \int_{\Omega} \sum_r W_r \left[ h(t) * \left( \dot{\mathbf{s}}(\mathbf{x}_r, t, \mathbf{m}) - \dot{\mathbf{d}}(\mathbf{x}_r, t) \right) \right] \delta(\mathbf{x} - \mathbf{x}_r) \cdot h(t) * \delta \dot{\mathbf{s}} d^3 \mathbf{x} dt \\
&- \int_0^T \int_{\Omega} [\rho \partial_t^2 \boldsymbol{\lambda} - \nabla \cdot (\mathbf{C} : \nabla \boldsymbol{\lambda})] \cdot \delta \mathbf{s} d^3 \mathbf{x} dt \\
&- \int_{\Omega} [\rho (\boldsymbol{\lambda} \cdot \partial_t (\delta \mathbf{s}) - \partial_t \boldsymbol{\lambda} \cdot \delta \mathbf{s})]_0^T d^3 x \\
&+ \int_0^T \int_{\partial \Omega_1} \boldsymbol{\lambda} \cdot [\hat{\mathbf{n}} \cdot (C : \nabla \delta \mathbf{s})] - \hat{\mathbf{n}} \cdot (C : \nabla \boldsymbol{\lambda}) \cdot \delta \mathbf{s} d^2 \mathbf{x} dt \\
&+ \int_0^T \int_{\partial \Omega_2} \boldsymbol{\lambda} \cdot [\hat{\mathbf{n}} \cdot (C : \nabla \delta \mathbf{s})] - \hat{\mathbf{n}} \cdot (C : \nabla \boldsymbol{\lambda}) \cdot \delta \mathbf{s} d^2 \mathbf{x} dt \\
&+ \int_0^T \int_{\Sigma_+} \boldsymbol{\lambda} \cdot [\hat{\mathbf{n}} \cdot (C : \nabla \delta \mathbf{s})] - \hat{\mathbf{n}} \cdot (C : \nabla \boldsymbol{\lambda}) \cdot \delta \mathbf{s} d^2 \mathbf{x} dt \\
&+ \int_0^T \int_{\Sigma_-} \boldsymbol{\lambda} \cdot [\hat{\mathbf{n}} \cdot (C : \nabla \delta \mathbf{s})] - \hat{\mathbf{n}} \cdot (C : \nabla \boldsymbol{\lambda}) \cdot \delta \mathbf{s} d^2 \mathbf{x} dt \\
&+ \int_0^T \int_{\Sigma} \boldsymbol{\mu} \cdot (\delta \dot{\mathbf{s}}_+ - \delta \dot{\mathbf{s}}_-) d^2 \mathbf{x} dt
\end{aligned} \tag{2.13}$$

where  $[f]_0^T = f(T) - f(0)$  for any function  $f$ . We can simplify this expression by considering the perturbed initial conditions,  $\delta \mathbf{s}(\mathbf{x}, 0) = \mathbf{0}$  and  $\partial_t \delta \mathbf{s}(\mathbf{x}, 0) = \mathbf{0}$ ; the perturbed free surface boundary condition,  $\hat{\mathbf{n}} \cdot (C : \nabla \delta \mathbf{s}) = 0$  on  $\partial \Omega_1$ ; the perturbed absorbing boundary condition,  $\hat{\mathbf{n}} \cdot (C : \nabla \delta \mathbf{s}) = C_{abs} \delta \dot{\mathbf{s}}$  on  $\partial \Omega_2$ , whose contribution we further integrate by parts; and the perturbed continuity of tractions on the fault surface  $[\hat{\mathbf{n}} \cdot (C : \nabla \delta \mathbf{s})]_+ = -[\hat{\mathbf{n}} \cdot (C : \nabla \delta \mathbf{s})]_-$ , noting in addition that  $\hat{\mathbf{n}}_+ = -\hat{\mathbf{n}}_-$ . We

obtain

$$\begin{aligned}
0 = \frac{\partial \mathcal{L}}{\partial \dot{\mathbf{s}}} \delta \dot{\mathbf{s}} &= \int_0^T \int_{\Omega} \sum_r W_r \left[ h(t) * \left( \dot{\mathbf{s}}(\mathbf{x}_r, t, \mathbf{m}) - \dot{\mathbf{d}}(\mathbf{x}_r, t) \right) \right] \delta(\mathbf{x} - \mathbf{x}_r) \cdot h(t) * \delta \dot{\mathbf{s}} d^3 \mathbf{x} dt \\
&- \int_0^T \int_{\Omega} [\rho \partial_t^2 \boldsymbol{\lambda} - \nabla \cdot (\mathbf{C} : \nabla \boldsymbol{\lambda})] \cdot \delta \mathbf{s} d^3 \mathbf{x} dt \\
&- \int_{\Omega} [\rho (\boldsymbol{\lambda} \cdot \partial_t (\delta \mathbf{s}) - \partial_t \boldsymbol{\lambda} \cdot \delta \mathbf{s})]^T d^3 x \\
&- \int_0^T \int_{\partial \Omega_1} \hat{\mathbf{n}} \cdot (\mathbf{C} : \nabla \boldsymbol{\lambda}) \cdot \delta \mathbf{s} d^2 \mathbf{x} dt \\
&+ \int_{\partial \Omega_2} [C_{abs} \boldsymbol{\lambda} \cdot \delta \mathbf{s}]^T d^2 \mathbf{x} - \int_0^T \int_{\partial \Omega_2} \left( C_{abs} \dot{\boldsymbol{\lambda}} + \hat{\mathbf{n}} \cdot (\mathbf{C} : \nabla \boldsymbol{\lambda}) \right) \cdot \delta \mathbf{s} d^2 \mathbf{x} dt \\
&+ \int_0^T \int_{\Sigma} [(\boldsymbol{\lambda}_+ - \boldsymbol{\lambda}_-) \cdot \hat{\mathbf{n}} \cdot (\mathbf{C} : \nabla \delta \mathbf{s})] \\
&- [\hat{\mathbf{n}} \cdot (\mathbf{C} : \nabla \boldsymbol{\lambda}) \cdot \delta \mathbf{s}]_+ - [\hat{\mathbf{n}} \cdot (\mathbf{C} : \nabla \boldsymbol{\lambda}) \cdot \delta \mathbf{s}]_- \\
&+ \boldsymbol{\mu} \cdot (\delta \dot{\mathbf{s}}_+ - \delta \dot{\mathbf{s}}_-) d^2 \mathbf{x} dt
\end{aligned} \tag{2.14}$$

where  $[f]^T = f(T)$ . Since this stationarity condition should be valid for all  $\delta \mathbf{s}$  (and all  $\delta \dot{\mathbf{s}}$ ), and noting that the adjoint of convolution is cross-correlation, which we denote by  $\star$ , we get

$$\rho \partial_t^2 \boldsymbol{\lambda} - \nabla \cdot (\mathbf{C} : \nabla \boldsymbol{\lambda}) = \sum_r W_r h \star \left[ h * \left( \dot{\mathbf{s}}(\mathbf{x}_r, \mathbf{m}) - \dot{\mathbf{d}}(\mathbf{x}_r) \right) \right] (t) \delta(\mathbf{x} - \mathbf{x}_r) \tag{2.15}$$

subjected to the following boundary and terminal conditions:

$$\begin{aligned}
\hat{\mathbf{n}} \cdot (\mathbf{C} : \nabla \boldsymbol{\lambda}) &= 0 \quad \text{on } \partial \Omega_1 \\
\hat{\mathbf{n}} \cdot (\mathbf{C} : \nabla \boldsymbol{\lambda}) &= -C_{abs} \dot{\boldsymbol{\lambda}} \quad \text{on } \partial \Omega_2 \\
\boldsymbol{\lambda}(\mathbf{x}, T) &= \mathbf{0} \\
\partial_t \boldsymbol{\lambda}(\mathbf{x}, T) &= \mathbf{0} \\
\boldsymbol{\lambda}_+ &= \boldsymbol{\lambda}_- \quad \text{on } \Sigma \\
[\hat{\mathbf{n}} \cdot (\mathbf{C} : \nabla \boldsymbol{\lambda})]_+ &= -[\hat{\mathbf{n}} \cdot (\mathbf{C} : \nabla \boldsymbol{\lambda})]_- \quad \text{on } \Sigma
\end{aligned} \tag{2.16}$$

and to the following requirement:

$$\boldsymbol{\mu} = [\hat{\mathbf{n}} \cdot (C : \nabla \boldsymbol{\lambda})]_+ \quad (2.17)$$

We define the adjoint wavefield as

$$\mathbf{s}^\dagger(\mathbf{x}, t) = \boldsymbol{\lambda}(\mathbf{x}, T - t). \quad (2.18)$$

It satisfies the following adjoint wave equation:

$$\rho \partial_t^2 \mathbf{s}^\dagger - \nabla \cdot (C : \nabla \mathbf{s}^\dagger) = \mathbf{f}^\dagger(\mathbf{x}, t) \quad (2.19)$$

subject to the following adjoint source:

$$\mathbf{f}^\dagger(\mathbf{x}, t) = \sum_{r=1}^{N_{sta}} W_r h \star \left[ h \star \left( \dot{\mathbf{s}}(\mathbf{x}_r) - \dot{\mathbf{d}}(\mathbf{x}_r) \right) \right] (T - t) \delta(\mathbf{x} - \mathbf{x}_r), \quad (2.20)$$

and to the following boundary and initial conditions:

$$\begin{aligned} \hat{\mathbf{n}} \cdot (C : \nabla \mathbf{s}^\dagger) &= 0 \quad \text{on } \partial\Omega_1, \\ \hat{\mathbf{n}} \cdot (C : \nabla \mathbf{s}^\dagger) &= C_{abs} \dot{\mathbf{s}}^\dagger \quad \text{on } \partial\Omega_2, \\ \mathbf{s}^\dagger(\mathbf{x}, 0) &= \mathbf{0}, \\ \partial_t \mathbf{s}^\dagger(\mathbf{x}, 0) &= \mathbf{0}, \\ \mathbf{s}^\dagger_+ &= \mathbf{s}^\dagger_- \quad \text{on } \Sigma, \\ [\hat{\mathbf{n}} \cdot (C : \nabla \mathbf{s}^\dagger)]_+ &= - [\hat{\mathbf{n}} \cdot (C : \nabla \mathbf{s}^\dagger)]_- \quad \text{on } \Sigma. \end{aligned} \quad (2.21)$$

Note that the adjoint field assumes a locked fault (no slip): the last two equations express the continuity of displacements and tractions of the adjoint field across the fault surface  $\Sigma$ . We define the adjoint tractions on the “+” side of the fault,  $\Sigma_+$ , by

$$\mathbf{T}^\dagger(\mathbf{x}, t) = (C(\mathbf{x}) : \nabla \mathbf{s}^\dagger(\mathbf{x}, t)) \cdot \hat{\mathbf{n}}(\mathbf{x}) \quad (2.22)$$

Equation 2.17 then gives, for any  $\mathbf{x} \in \Sigma$ ,

$$\boldsymbol{\mu} = \mathbf{T}^\dagger(\mathbf{x}, t). \quad (2.23)$$

The second stationarity condition is

$$0 = \frac{\partial \mathcal{L}}{\partial \mathbf{m}} \delta \mathbf{m} = \frac{\partial \chi}{\partial \mathbf{m}} \delta \mathbf{m} - \int_0^T \int_\Sigma \boldsymbol{\mu} \cdot \delta \mathbf{m} d^2 \mathbf{x} dt \quad (2.24)$$

Considering Equation 2.23, we obtain a useful expression for the gradient of the cost function:

$$\frac{\partial \chi}{\partial \mathbf{m}} \delta \mathbf{m} = \int_0^T \int_\Sigma \mathbf{T}^\dagger(\mathbf{x}, T - t) \cdot \delta \mathbf{m} d^2 \mathbf{x} dt. \quad (2.25)$$

The third stationarity condition is

$$0 = \frac{\partial \mathcal{L}}{\partial \boldsymbol{\lambda}} \delta \boldsymbol{\lambda} = \int_0^T \int_\Omega \delta \boldsymbol{\lambda} \cdot [\rho \partial_t^2 \mathbf{s} - \nabla \cdot (\mathbf{C} : \nabla \mathbf{s})] d^3 \mathbf{x} dt \quad (2.26)$$

Since the above equation should be valid for all  $\delta \boldsymbol{\lambda}$ ,

$$\rho \partial_t^2 \mathbf{s} - \nabla \cdot (\mathbf{C} : \nabla \mathbf{s}) = \mathbf{0} \quad (2.27)$$

which is the forward wave equation.

Similarly, the fourth stationarity condition yields the slip boundary condition on the fault for the forward problem: for any  $\mathbf{x} \in \Sigma$ ,

$$\mathbf{m}(\mathbf{x}, t) = \dot{\mathbf{s}}_+(\mathbf{x}, t) - \dot{\mathbf{s}}_-(\mathbf{x}, t) \quad (2.28)$$

In common practice seismograms are band-pass filtered prior to source inversion. We note that the model in previous adjoint source inversion implementations [Kremers *et al.*, 2011; Hjörleifsdóttir *et al.*, 2007; Kim *et al.*, 2011; Akcelik *et al.*, 2006] based on pre-filtered data actually represents a filtered version of the complete source model. The approach described here handles the temporal filter in a novel way: the forcing term for the adjoint wave equation (Equation 2.20) involves a cross-correlation of

the filter and the filtered residuals. This is the result of the Lagrangian based on filtered waveform residuals (Equation 2.6). In Equation 2.20 the cross-correlation operation is introduced in the data space. Alternatively, one can introduce the cross-correlation in the model space, in which case, the integrand of Equation 2.25 will be a cross-correlation of the filter and the adjoint tractions. Whether the cross-correlation is introduced in data space or model space, our formulation allow to retrieve the unfiltered version of the source.

## 2.4 Discrete formulation and model parametrization

The simplest possible parametrization of the model is adopted here. The fault surface is decomposed into a mesh of  $N_{fault}$  non-overlapping fault elements of typical size  $\Delta x_m$ . The time axis is decomposed into  $N_t$  regular time intervals of size  $\Delta t_m$ . The slip rate is represented by a piecewise constant distribution in space and time, i.e., slip rate is constant inside each fault element and each time interval. This implies that the unknowns in our inverse problem are essentially the average slip rates within spatio-temporal cells of dimensions  $\Delta x_m \times \Delta t_m$ . We refrain from using higher order basis functions (linear, splines, etc.) because the resulting discrete representation of a non-negative continuum field can have negative values (see Section 2.5), which complicates the enforcement of non-negativity constraints on the continuum model.

We set the temporal resolution of the model parameterization,  $\Delta t_m$ , such that an RMS misfit lower than 1% is achieved between low-pass filtered ground motions computed from a continuum source and from its temporally discrete version. In practice the continuum source is also discrete, but described with a very small timestep. For a specific source scenario described in a later Section, we find that this is achieved with  $\Delta t_m = 0.1/f_c$ , where  $f_c$  is the cut-off frequency of the data filter (Figure 2.2).

We set the spatial resolution of the model parameterization,  $\Delta x_m$ , to be much smaller than the minimum wavelength at the cut-off frequency,  $\lambda = c_S/f_c$  [Liu and Archuleta, 2004]. We carry out the wave propagation simulations using a spectral element code [Komatitsch et al., 2010]. Adequate accuracy is obtained by setting a

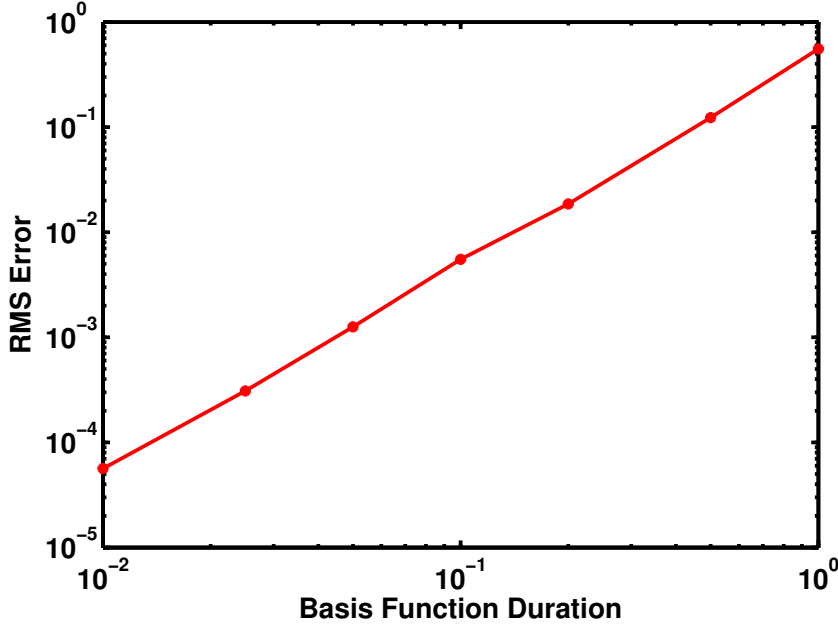


Figure 2.2: Root mean squared (RMS) error between data and synthetics as a function of the timestep of the temporal basis functions that discretize the slip velocity. The data is computed based on a very finely discretized source, to represent a continuum source. A timestep of 0.1 sec explains 99% of the data.

spectral element size comparable to the minimum wavelength  $\lambda$  and a polynomial order of four, that is  $N_{GLL} = 5$  Gauss-Lobatto-Legendre nodes per spectral element edge. The slip velocity model is represented at all the spectral nodes, so the average spatial resolution of the model is  $\Delta x_m \approx \lambda / (N_{GLL} - 1)$ .

## 2.5 Higher-order representations do not preserve positivity

Through an example we show that the representation of a non-negative continuum model by linear basis functions might introduce negative values. Consider a representation  $m(t)$  of a continuous slip-rate function  $v(t)$  in terms of orthonormal linear

temporal basis functions  $b_q(t)$ :

$$v(t) \approx m(t) = \sum_{p=0}^{N_t} m_p b_p(t) \quad (2.29)$$

where

$$b_q(t) = \begin{cases} \frac{t-t_{q-1}}{t_q-t_{q-1}} & \text{if } t \in [t_{q-1}, t_q] \\ \frac{t_{q+1}-t}{t_{q+1}-t_q} & \text{if } t \in [t_q, t_{q+1}] \\ 0 & \text{otherwise} \end{cases} \quad (2.30)$$

The coefficients  $m_p$  are found by solving

$$\int_0^T (m(t) - v(t)) b_p(t) dt = 0 \quad \forall p = 0 \text{ to } N_t \quad (2.31)$$

This leads to the following algebraic problem:

$$\mathbf{Bm} = \tilde{\mathbf{v}} \quad (2.32)$$

where  $\mathbf{B}$  is a tridiagonal matrix with components

$$B_{pq} = \int_0^T b_p(t) b_q(t) dt \quad (2.33)$$

and  $\tilde{\mathbf{v}}$  is a vector with components

$$\tilde{v}_p = \int_0^T v(t) b_p(t) dt. \quad (2.34)$$

Consider a continuous slip-rate function  $v(t)$  discretized by four linear basis functions with unit width. Consider the following non-negative vector of projected slip rates

$$\tilde{\mathbf{v}} = \begin{bmatrix} 2 \\ 1 \\ 4 \\ 3 \end{bmatrix} \quad (2.35)$$

Solving Equation 2.32 with

$$\mathbf{B} = \frac{1}{3} \begin{bmatrix} 1 & 0.5 & 0 & 0 \\ 0.5 & 2 & 0.5 & 0 \\ 0 & 0.5 & 2 & 0.5 \\ 0 & 0 & 0.5 & 1 \end{bmatrix} \quad (2.36)$$

we obtain the model coefficients

$$\mathbf{m} = \frac{1}{3} \begin{bmatrix} 20 \\ -4 \\ 14 \\ 20 \end{bmatrix}. \quad (2.37)$$

A negative value in the model coefficients appears even though all the projected values are non-negative.

## 2.6 Verification of the adjoint field computation

One can perform a dot-product test [Claerbout and Fomel, 2008] to verify that the computation of the adjoint field is implemented correctly in a 3D wave propagation code. The test amounts to verifying that Equation 2.5 holds for arbitrary  $\mathbf{m}'$  and  $\mathbf{d}'$ . The test involves two inner products, one in data space and one in model space. The inner product in data space is the one emerging from the definition of the cost function (Equation 2.2). The inner product in model space is

$$\langle \mathbf{G}^\dagger \mathbf{d}', \mathbf{m}' \rangle = \sum_{p=0}^{N_t} \int_{\Sigma} m'_p(\mathbf{x}) \tau'_p(\mathbf{x}) d^2 \mathbf{x} = \tau'^\dagger W_m m'$$

where  $\tau'_q$  is the discrete version of the adjoint field,  $\mathbf{G}^\dagger \mathbf{d}'$ , at the  $p$ -th timestep and  $W_m$  is the weighting matrix introduced by spatial integral.

## 2.7 Computational cost compared to pre-computed Green's functions approach

Here we compare the computational cost of our method to that of a prevailing approach that requires pre-computing Green's functions. The cost is here defined as the computational complexity quantified by the total number of floating point operations. The actual performance on modern-day computers is determined by many other factors such as cache or CPU pipeline optimization, I/O density and inter-processor communication. However, closed-form relations can be conveniently derived with a metric based on arithmetic operations which, as we have found in practice, allow an adequate comparison between two methods implemented in the same computer across a wide range of application scenarios.

Our method requires two simulations per iteration of the CG algorithm: one forward and one adjoint simulation. Because our focus is on source inversions incorporating 3D crustal velocity models, both simulations require a 3D wave propagation code. We choose the spectral element method (SEM) code SPECFEM3D, but any other 3D wave propagation code may be used if adjoint simulation capabilities can be incorporated. In addition to incorporating adjoint capabilities, we parallelized the fault solver in SPECFEM3D and tested for scaling and convergence (Appendix A). The total computational cost,  $\Gamma_{adj}$ , of an inversion with our adjoint approach is

$$\Gamma_{adj} = 2 N_{iter} C_{SEM} \quad (2.38)$$

where  $N_{iter}$  is the number of CG iterations and  $C_{SEM}$  is the computational cost of one 3D SEM wave propagation simulation. The latter is quantified here by the number of floating point multiplications, which we evaluated by inspection of the SPECFEM3D code, mainly in the routines corresponding to the elastic force computation and the Newmark timestepping:

$$C_{SEM} = N_t^{SEM} N_e \times 9 (2 N_{GLL} + 9) N_{GLL}^3 \quad (2.39)$$

where  $N_t^{SEM}$  is the number of timesteps of the SEM simulation and  $N_e$  the number of spectral elements.

Alternatively, one can implement the CG algorithm by pre-computing and storing a database of Green's functions (GF). The total cost of this approach,  $\Gamma_{GF}$ , comprises the cost per CG iteration plus the overhead cost of pre-computing the GFs,  $\Gamma_{GF}^{oh}$ . The number of CG iterations is the same for the adjoint and GF approaches,  $N_{iter}$ . The cost per iteration is dominated by the cost,  $2C_{conv}$ , of convolutions between the GFs and the slip-rate timeseries in step 6 and cross-correlations between GFs and residual ground velocity timeseries in step 9. Each of these operations involves essentially two FFTs per data channel ( $N_{sta}$  stations with three components) per model channel ( $N_{fault}$  fault cells with two components of slip rate). The timeseries contain  $N_t^{data}$  samples and the FFTs include zero-padding to twice this length. The number of floating point operations per FFT is  $O(10) 2N_t^{data} \log_2(2N_t^{data})$ . The overhead involves  $2 N_{fault}$  3D SEM wave propagation simulations. If reciprocity is exploited,  $3 N_{sta}$  simulations are needed. Hence,

$$\Gamma_{GF} = 2 N_{iter} C_{conv} + \Gamma_{GF}^{oh} \quad (2.40)$$

with

$$C_{conv} = 2 N_{fault} \times 3 N_{sta} \times O(10) 4N_t^{data} \log_2(2N_t^{data}) \quad (2.41)$$

and

$$\Gamma_{GF}^{oh} = \min(2N_{fault}, 3N_{sta}) \times C_{SEM} \quad (2.42)$$

The cost ratio of the two methods is

$$\frac{\Gamma_{GF}}{\Gamma_{adj}} = \frac{C_{conv}}{C_{SEM}} + \frac{\Gamma_{GF}^{oh}}{\Gamma_{adj}} \quad (2.43)$$

with

$$\frac{C_{conv}}{C_{SEM}} = O(10) \frac{24 N_{fault} N_{sta} N_t^{data} \log_2(2N_t^{data})}{9 N_e N_t^{SEM} N_{GLL}^3 (2N_{GLL} + 9)} \quad (2.44)$$

and

$$\frac{\Gamma_{GF}^{oh}}{\Gamma_{adj}} = \frac{\min(N_{fault}, 3/2 N_{sta})}{N_{iter}} \quad (2.45)$$

Figure 2.3 shows the cost ratio as a function of the number of stations for a specific earthquake scenario considered in a later Section. The rupture dimensions are 40 km along strike and 15 km along dip, typical of a  $M_w$  7.0 strike-slip earthquake. Ground motions up to approximately two fault lengths away from the source are included, low-passed filtered below 1 Hz. In this example, the pre-computed GF approach is more expensive than the adjoint approach if more than a few tens of stations are considered. Then the overhead of the GF approach dominates its cost and it is advantageous to use our adjoint approach if

$$N_{iter} < \min\left(N_{fault}, \frac{3}{2}N_{sta}\right) \quad (2.46)$$

We now develop order-of-magnitude estimates for all the terms in Equations 2.43 to 2.45. The number of fault cells,  $N_{fault}$ , is the potential rupture area (length  $L$  and width  $W$ ) divided by the area of each fault cell (size  $\Delta x_m \approx \lambda/(N_{GLL} - 1)$ , as explained in Section 2.4):  $N_{fault} = LW(N_{GLL} - 1)^2/\lambda^2$ . The number of timesteps for the GF approach,  $N_t^{data}$ , is the total duration of the seismograms,  $T$ , divided by the source timestep,  $\Delta t_m \approx 0.1/f_c$  (Section 2.4):  $N_t^{data} \approx 10Tf_c = 10T\lambda/c_S$ . For  $Tf_c = 10^2 \sim 10^4$ , a range covering most practical situations,  $\log_2(2N_t^{data}) = O(10)$ . The number of spectral elements,  $N_e$ , is the domain volume (a semi-sphere of radius a couple of fault lengths) divided by the volume of a spectral element:  $N_e = \frac{2}{3}\pi(2L/\lambda)^3$ . The number of SEM timesteps is the total simulation duration,  $T$ , divided by the SEM timestep ( $\approx 2\lambda/(c_p N_{GLL}^2)$  for  $N_{GLL} \approx 5$  and spectral element size  $\approx \lambda$ ):  $N_t^{SEM} \approx \frac{1}{2}c_p N_{GLL}^2 T/\lambda$ . The number of stations with spacing  $\Delta x_s$  on a disk of radius equal to a couple of fault lengths is  $N_{sta} = \pi(2L/\Delta x_s)^2$ . In our experience so far,  $N_{iter} = O(100)$ . Combining these estimates and considering  $N_{GLL} = 5$  and  $c_P/c_S = \sqrt{3}$ , we get

$$\frac{C_{conv}}{C_{SEM}} = O(1) \left(\frac{\lambda}{\Delta x_s}\right)^2 \frac{W}{\lambda} \quad (2.47)$$

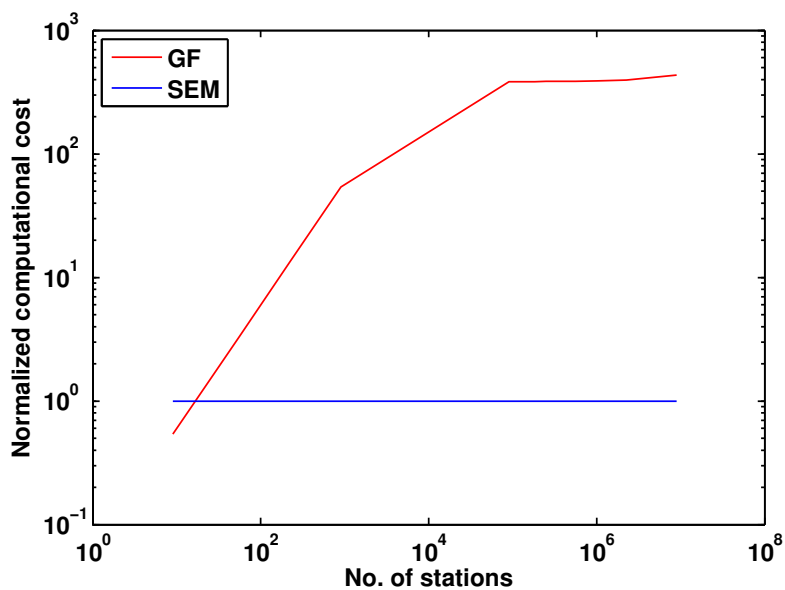


Figure 2.3: Comparison of the computational cost of the adjoint method based on the spectral element method (SEM) and the method with pre-computed Green’s functions (“GF approach”) for a typical  $M_w$  7.0 earthquake scenario with  $40 \times 15 \text{ km}^2$  rupture area, a 3D velocity model, data low-pass filtered below 1 Hz, fixed domain size extending up to approximately 2 fault lengths away from the source, and regular station spacing. The cost is normalized by the computational cost of SEM. The cost of the adjoint method does not depend on the number of stations, while the cost of the GF approach increases drastically until it becomes advantageous to exploit reciprocity to compute the Green’s functions.

and

$$\frac{\Gamma_{GF}^{oh}}{\Gamma_{adj}} = O(10^{-1}) \left(\frac{L}{\lambda}\right)^2 \min\left(\frac{W}{L}, \left(\frac{\lambda}{\Delta x_s}\right)^2\right). \quad (2.48)$$

We first compare the cost per iteration of both approaches (Equation 2.47). In source inversion of large earthquakes (say  $M > 7$ ) the wavelength corresponding to the cut-off frequency (typically  $f_c = O(1)$  Hz) is significantly smaller than the average spacing of current seismic networks (typically larger than 10 km) and smaller than the fault dimensions:  $\lambda/\Delta x_s = O(10^{-1})$  and  $W/\lambda = O(10)$ . These numbers imply  $C_{conv}/C_{SEM} = O(10^{-1})$ : in source inversion scenarios that are typical nowadays the GF approach has a much smaller cost per iteration than the adjoint approach based on SEM. However, if in the future we were to record the wavefield without aliasing on a dense network with spatial resolution somewhat finer than the minimum wavelength,  $\lambda/\Delta x_s = O(1)$ , the adjoint approach would have a relatively lower cost per iteration, especially so if we can aim at analyzing higher frequencies.

Even when the cost per iteration is lower in the GF approach, the adjoint approach can have a relative advantage due to the overhead of pre-computing GFs (Equation 2.48). Typically, rupture aspect ratios are in the range  $W/L = 0.1 \sim 1$  and the cut-off wavelength is a small to moderate fraction of the rupture length,  $L/\lambda = 10 \sim 100$ . For station spacings ranging from that of existing seismic networks to ideally unaliased dense networks,  $\lambda/\Delta x_s = O(10^{-1}) \sim O(1)$ . These numbers imply  $\Gamma_{GF}^{oh}/\Gamma_{adj} = O(10^{-1}) \sim O(10^3)$ : there is a significant range of situations in which the adjoint approach is more efficient than the GF approach. A denser network does not necessarily penalize the GF approach, because reciprocity can be exploited. This is reflected in the last term of Equation 2.48. For a coarse network with  $\Delta x_s \gg \lambda$ , we get  $W/L > (\lambda/\Delta x_s)^2$  and  $\Gamma_{GF}^{oh}/\Gamma_{adj} = O(10^{-1})(L/\Delta x_s)^2$ . The relative advantage of the adjoint approach in coarse networks is obvious only for ruptures that are very large compared to the average station spacing, for instance,  $M_w > 7$  for a network with 20 km spacing. For a very dense network with  $\Delta x_s \leq \lambda$ , we get  $W/L < (\lambda/\Delta x_s)^2$  and  $\Gamma_{GF}^{oh}/\Gamma_{adj} = O(10^{-1})LW/\lambda^2$ . For frequencies up to 1 Hz ( $\lambda \sim 3.6$  km) and  $M_w > 6.2$ , typically  $LW/\lambda^2 > 10$  and the advantage of the adjoint approach in very

dense networks is clear, especially for large ruptures. It is further emphasized at higher frequencies.

## 2.8 Summary

A method for earthquake source inversion including 3D heterogeneities of the crust is presented. The method is based on an adjoint linear formulation and is implemented here with wave propagation simulated with a spectral element method. The adjoint approach is found to be generally more computationally advantageous than the usual approach based on pre-computed Green's functions. The method presented here is an efficient way to incorporate information about lateral heterogeneity on earthquake source inversions, and take full advantage of the increasing availability of 3D tomography models at regional scales in order to improve the resolution of earthquake rupture processes.

## Chapter 3

# Impact of crustal structure uncertainties on source inversion

We show here that our source inversion procedure described in Chapter 2 reconstructs well the source when the 3D velocity model is known in complete detail. We denote these inversions as “reference inversions”. The 3D velocity model of Earth crust is known to follow von Karman statistics [*Frankel and Clayton, 1986*]. Analyzing the Bay Area velocity model provided by USGS, *Hartzell et al. [2010]* found that uncertainties in 3D velocity model represented as von Karman distribution has near zero Hurst exponent with 5 km correlation length and 5% standard deviation. Generating such a velocity model, we run forward simulation to compute synthetic data using which inversion is carried out employing methodology presented in Chapter 2 to see how it would compare with reference inversions. We also explore the parameters for von Karman distribution that can give reliable inversions comparable to reference inversions, when uncertainties in velocity model are not known.

### 3.1 Reference inversions with known 3D velocity model

We consider as earthquake scenario a Haskell source, a steady slip pulse with square slip-rate time function of rise time 1 sec propagating at a rupture speed of 2.9 km/s on a vertical strike-slip fault of dimensions 40 km  $\times$  15 km. Stations extend about two fault lengths away on each side giving a coverage of 200 km  $\times$  160 km. A fourth-order low-pass Butterworth filter with a corner frequency of 1 Hz is applied to

	Correlation Length ( $R_c$ )	Standard deviation ( $\sigma$ )	Hurst Exponent ( $\nu$ )
<b>Model A</b>	<b>5 km</b>	<b>5 %</b>	<b>0.0</b>
<b>Model B</b>	<b>0.5 km</b>	<b>5 %</b>	<b>0.0</b>
<b>Model C</b>	<b>5 km</b>	<b>1 %</b>	<b>0.0</b>

Table 3.1: Parameters of the three random velocity models (A, B and C) with von Karman correlation function

the data. The fault is embedded in a 3D velocity model with lateral heterogeneities superimposed on a homogeneous half-space. The average P-wave velocity is 5.6 km/s, S-wave velocity 3.2 km/s and density 2.67 g/cm<sup>3</sup>. The velocity heterogeneities have Gaussian probability distribution and von Karman spatial correlation function with correlation length  $R_c$ , standard deviation  $\sigma$  and Hurst exponent  $H$  given as “model A” in Table 1 (Figure 3.1). We assume  $V_s = V_p/\sqrt{3}$ .

We consider two different station densities: one with a station spacing of 1 km denoted as dense network and the other with a station spacing of 20 km denoted as coarse network (Figure 3.2). The dense network setup is motivated by emergent concepts for earthquake observation systems [*Michel et al.*, 2013] and the block-by-block measurements using cheap MEMS-based sensors [*Clayton et al.*, 2012] that could provide ground motion recordings at every few hundreds of meters. The coarse network is representative of the average station spacing of the current Japanese seismic networks. Performing an inversion for the dense network would be challenging for currently available source inversion codes. Figure 3.3 shows results of the inversions based on the coarse network and the dense network. The spatial distribution of slip rate is sharper in the source model inferred from the dense dataset. This illustrates the intuitive idea that source recovery improves with increased number of sensors.

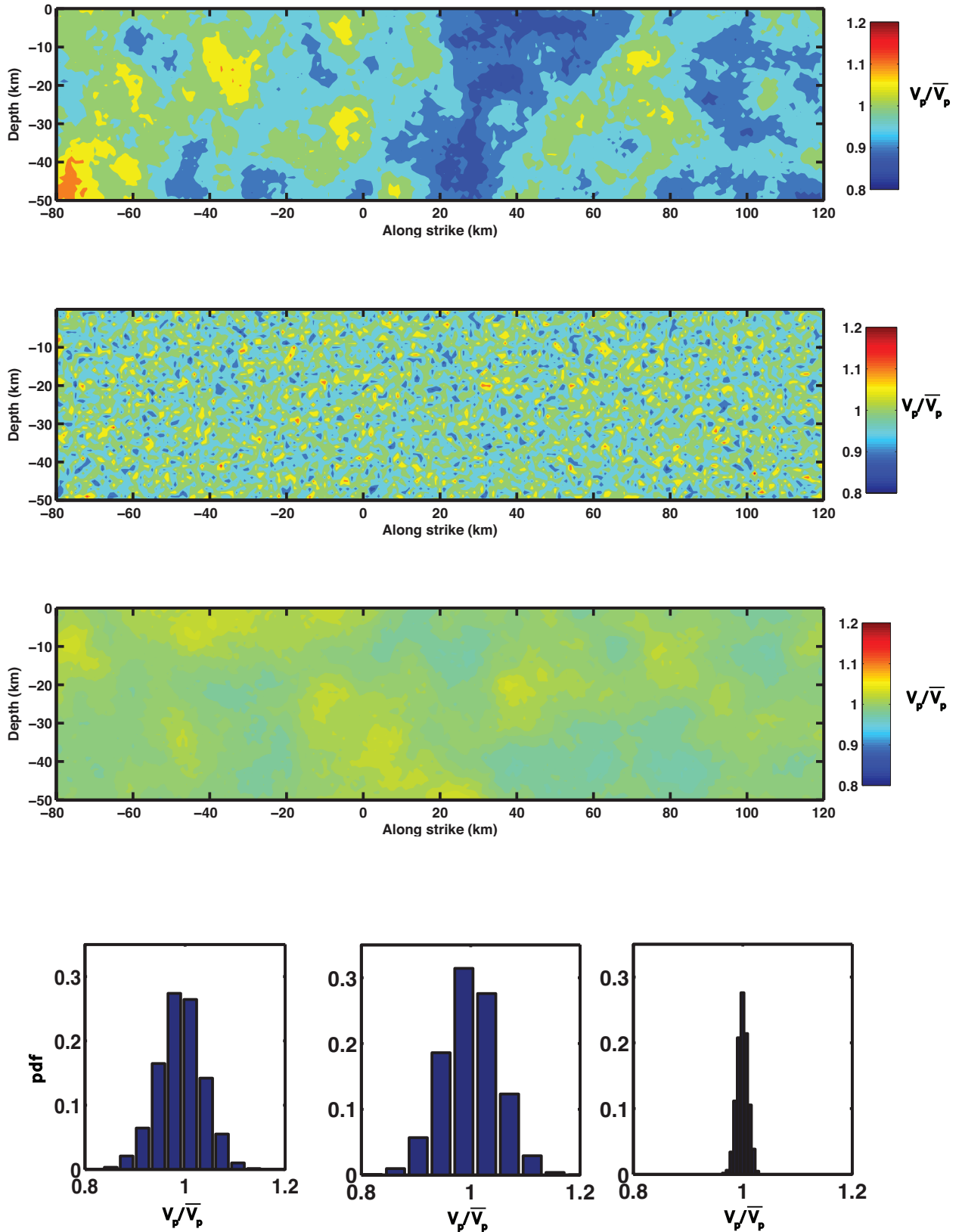


Figure 3.1: Spatial distribution of P-wave velocity ( $V_p$ ), normalized by its mean (5.6 km/s), on a cross section parallel to the fault plane for the three velocity models A, B and C (from top to bottom) with random heterogeneity described in Table 3.1. Histograms for each model are shown at the bottom.

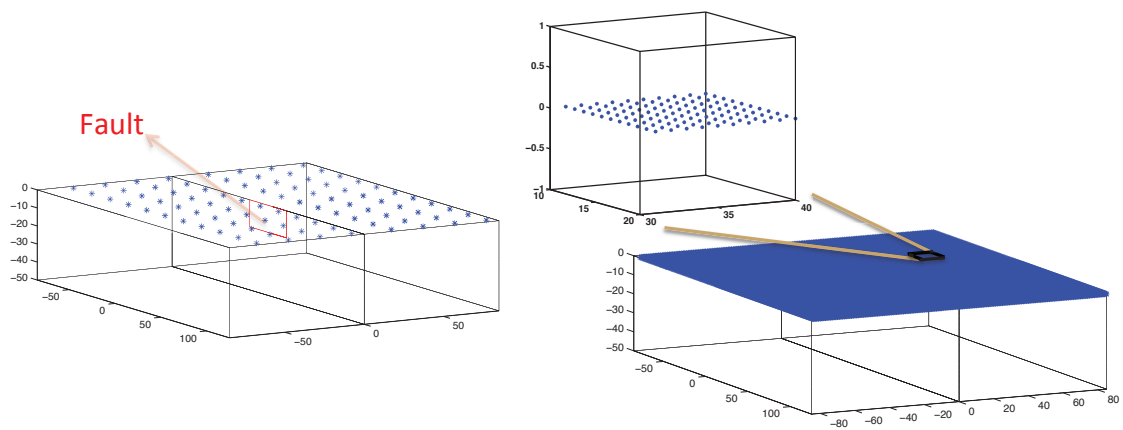


Figure 3.2: Fault and station geometry for a  $M_w 7$  earthquake scenario in two hypothetical networks with (a) 20 km and (b) 1 km station spacing. The number of stations for each network is 88 and 32160, respectively. The fault ( $40 \text{ km} \times 15 \text{ km}$ ) is in the XZ-plane. The domain is symmetric with respect to the XZ-plane. Blue stars indicate station locations. The inset shows a zoomed portion of a  $10 \text{ km} \times 10 \text{ km}$  area. The number of stations in the inset is more than the total number of stations in the 20 km network.

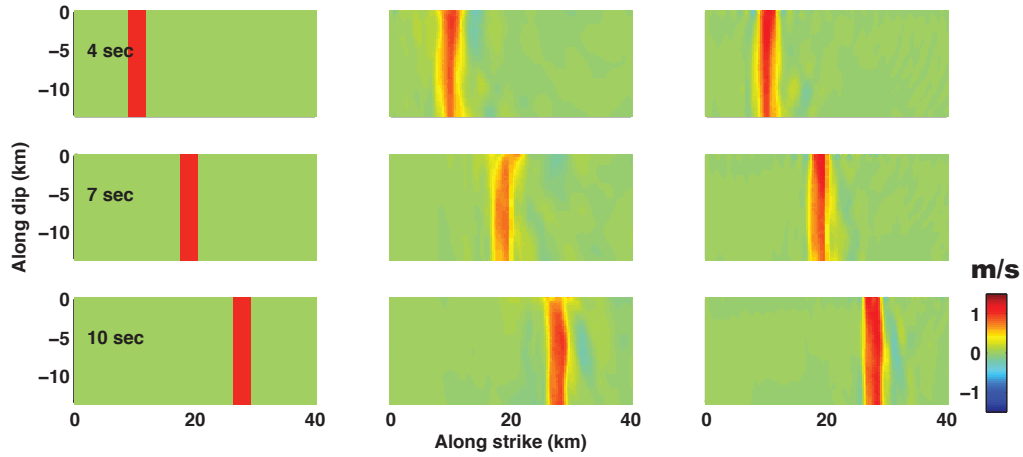


Figure 3.3: Results from reference inversions. Data is generated in the 3D heterogeneous velocity model A and source inversion is performed assuming the same heterogeneous velocity model. The left column shows snapshots of input slip rate at three different times. The middle and right columns show inverted slip rate from the data of the 20 km network and the 1 km network, respectively. Note that the dense network allows for a better source recovery. It would be challenging for current source inversion codes and methodologies to do this inversion for the dense network with 32160 stations.

## 3.2 Effect of uncertainties in the 3D velocity model on source recovery

We discuss here the effects of ignoring the heterogeneity of the crustal velocity model by comparing reference inversions to inversions that adopt the background homogeneous velocity model. Given the currently available velocity models and their estimated level of uncertainty, we aim at understanding whether or not one can invert for slip rate on the fault plane adequately without taking into account the uncertainty in velocity structure.

Assuming that the heterogeneities in model A are unknown, inversions are carried out in a homogeneous half-space corresponding to the background velocity model A. Comparing the second and third columns of Figure 3.3 with the respective columns of Figure 3.4, it can be seen that the dense network maps most of the slip rate into the shallowest portions of the fault. This indicates that a denser network may not improve source inversion if the bulk uncertainties have the statistical properties assumed here

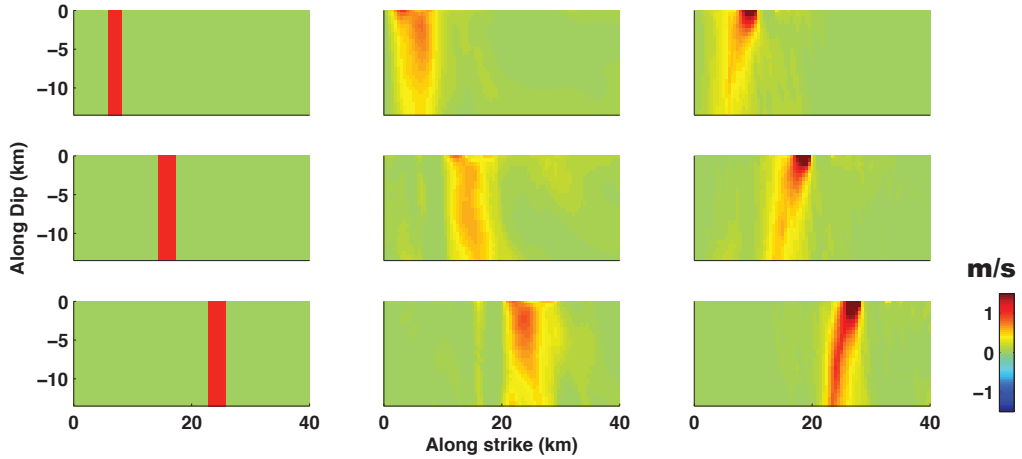


Figure 3.4: Same as Figure 3.3, with data generated in model A but now with source inversion based on the background homogeneous velocity model. The inverted slip pulses are distorted (bending in the dense network and widening of the pulse in the sparse network) compared to the reference inversions shown in Figure 3.3.

(standard deviation of 5% and von Karman correlation function with Hurst exponent of near zero and correlation length of 5 km).

We repeat this exercise for two other 3D heterogeneous velocity models: one with much shorter correlation length (model B) and one with smaller standard deviation (model C). The average velocities are the same for all models. The main parameters of the three models are summarized in Table 1. Typical cross sections and histograms are shown in Figure 3.1. Reference inversions using the true velocity models B and C (not shown here) yield similar results as the reference inversion in model A (Figure 3.3). For the earthquake scenarios generated in models B and C the results from inversions assuming the homogeneous velocity model (Figures 3.5 and 3.6) yield slip rates qualitatively similar to those obtained in reference inversions (Figure 3.3).

An explanation for the differences in the effect of velocity model uncertainties on source inversion across the different velocity models considered here could be obtained by examining their power spectra (Figure 3.7). The normalized power spectral density of a von Karman distribution is given by:

$$P(k) \sim \frac{\sigma^2(4\pi R_c^2)^{3/2}}{(1 + (kR_c)^2)^{3/2}} \quad (3.1)$$

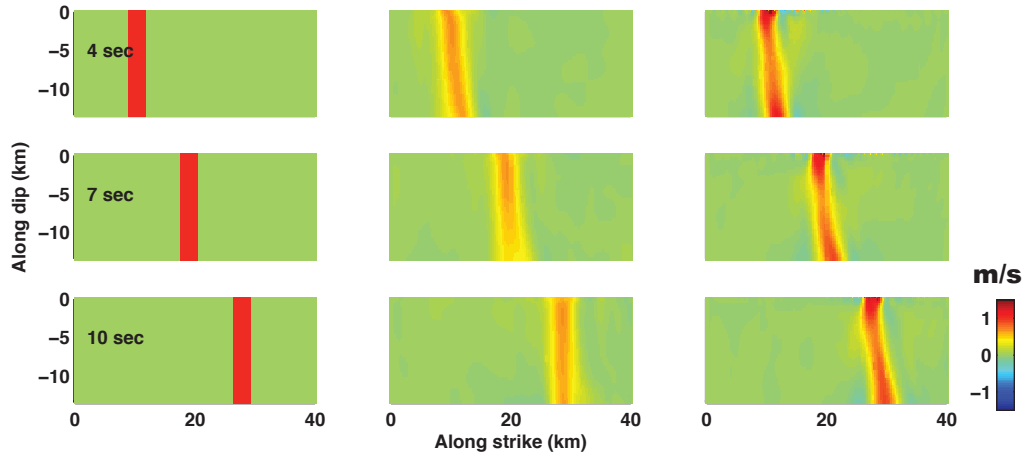


Figure 3.5: Same as Figure 3.4, but with data generated in model B (the source inversion still assumes the homogeneous background velocity model). The pulses recovered with the dense network are distorted while those of the sparse network are qualitatively similar to results of an inversion based on the true velocity model (not shown).

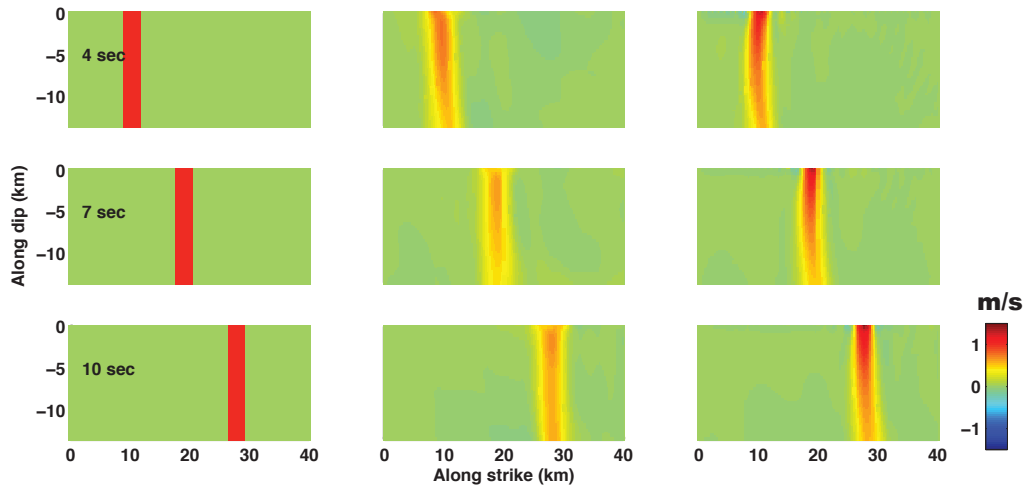


Figure 3.6: Same as Figure 3.4, but with data generated in model C. For both networks, the inverted pulses are qualitatively similar to the results of inversions based on the true velocity model (not shown).

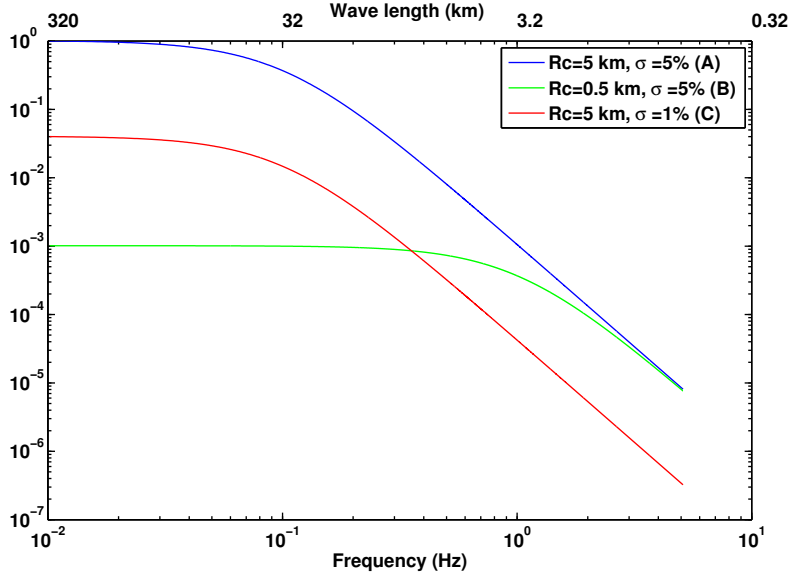


Figure 3.7: Power spectrum of the three heterogeneous velocity models considered, normalized by the peak value of model A

where  $k$  is the wavenumber. We map wavenumber into frequency [Frankel and Clayton, 1986] using  $2\pi f = k C_s$  where  $C_s$  is the shear-wave speed. Models B and C have low spectral amplitude in the frequency band of inversion ( $f < 1$  Hz), at least one order of magnitude lower than that of model A, and hence have less impact on the quality of the source inversion.

Our formulation of the inverse problem assumed implicitly that noise is Gaussian and uncorrelated. In a source inversion based on an incorrect velocity model the major source of noise is the wavefield scattered by the unknown heterogeneities. This noise can be correlated over length scales comparable to the correlation length of the heterogeneities. One might hypothesize that the spatial correlation of the scattered wavefield affects source inversions if its correlation length is larger than the station spacing and our results support this intuition. In model B, which has an effective correlation length of  $2\pi R_c \sim 3.14$  km, the coarse network (20 km spacing) might not see this noise correlation, but the dense network (1 km spacing) might (Figure 3.5). For model A, however, both networks will sense this correlation, because their stations spacing is shorter than the effective correlation length of the medium,  $2\pi R_c \sim 31.4$  km

(Figure 3.4). *Yagi and Fukahata* [2008] have discussed how to handle noise correlation induced by uncertainties in the velocity model.

The heterogeneities have the same correlation length in model C as in model A, but lower amplitudes. The slip pulses inferred in model C (Figure 3.6) have closer resemblance to the reference inversion (Figure 3.3) than those inferred in model A (Figure 3.4). So, the effects of noise correlation may be mitigated by reducing the amplitude of the uncertainties in the velocity model, even if the noise correlation is not accounted for in the inversion technique. When the velocity structure is poorly known and dense datasets are available, one may consider a joint inversion of source and structure [*Akcelik et al.*, 2006].

### 3.3 Validity of our study for other rise times

Although we considered only one scenario with rise time of 1 sec, we expect our findings to be valid for other rise times longer than 1 sec. This is confirmed in Figure 3.8, which shows the results of source inversions based on rupture scenarios with rise times of 2, 4 and 8 s. Scenarios are computed in the heterogeneous model A, while inversions are carried out on the homogenous background velocity model. Amplification and distortion of the slip pulse in the inversions based on data from the dense network is also observed in these cases, as was found for a rise time of 1 sec (Figure 3.3). Qualitatively similar deterioration of the inferred slip pulse is observed irrespective of rise time for inversions related to one particular 3D heterogeneous medium (Figure 3.8). The same has to be true for other media as well, suggesting that our observations are independent of rise time if it is longer than 1 s. Resolving rise times shorter than 1 s requires a finer temporal discretization of the source and, more importantly, higher frequency data.

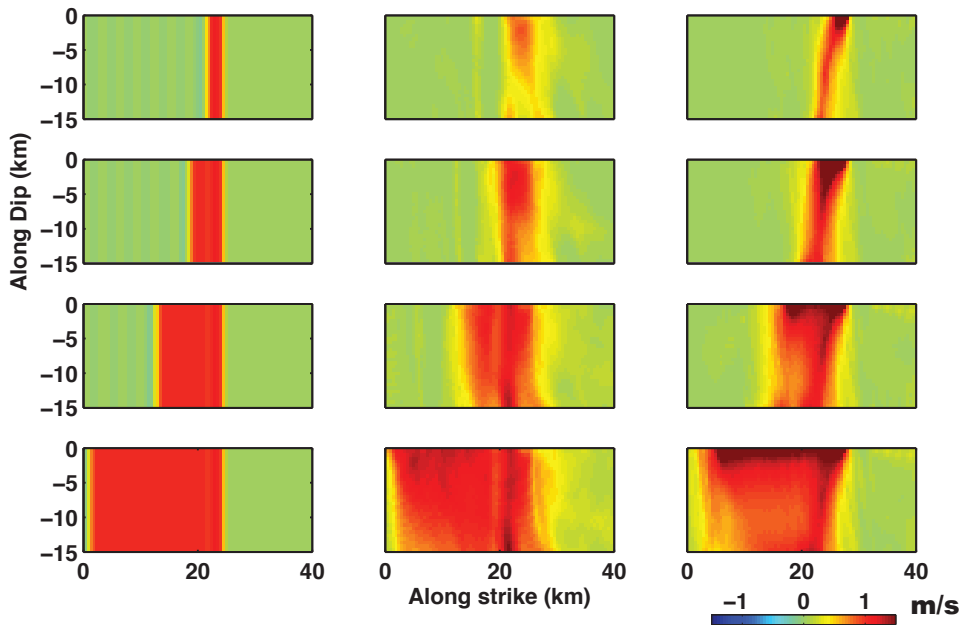


Figure 3.8: Effect of rise time on source inversions. Data is generated in model A and inversion assumes the homogeneous background velocity model. The description of the three columns is the same as that given in Figure 3.3. Each row shows a representative snapshot of slip rate for rise times 1 sec, 2 sec, 4 sec and 8 sec, respectively, top to bottom. The slip pulse is distorted in the dense network irrespective of rise time.

### 3.4 Summary

The adjoint inversion adequately retrieves spatio-temporal details of the rupture process when the 3D velocity structure is known. Typical uncertainties in crustal velocity models, represented by a von Karman distribution of 5 km correlation length and 5% standard deviation (with Hurst exponent of zero), severely degrade the quality of source inversions. However, if the velocity uncertainties have a correlation of 500 m or a standard deviation of 1%, then source inversion has an adequate quality. These conclusions are independent of rise time, if longer than 1 s.

## Chapter 4

# Rise-time resolution: Effect of network spacing and rupture velocity

Knowledge of rise time of an earthquake is useful in determining whether the event is crack-like or pulse-like. The latter produces strong shaking on the far side of rupture thereby causing extensive damage. In this Chapter we attempt to quantify the resolvability of rise time considering networks ranging from 2 km to few tens of km. To accomplish this, we propose a hybrid method that combines the best of the features available in various source inversion approaches. The conjugate-gradient algorithm that forms the basis of this method is similar to that presented in Chapter 2 with the only difference, the gradient of the cost function can now be readily computed without having to run wave propagation simulations, assuming that the Green's functions are known.

Using the hybrid inversion method developed, we focus on understanding the accuracy of rise-time estimates as a function of spacing between recorded stations. We choose the simplest possible source description, a Haskell pulse, to address the resolvability of rise time. *Saraò et al.* [1998] considered a Haskell-type rupture on dip-slip faults and found that coverage in the forward direction of rupture gives better results than the same number of stations placed in backward direction. *Miyatake et al.* [1986] concluded that a straight-line array perpendicular to the fault is less advantageous than a straight-line array parallel to the fault for source inversions. *Olson and Anderson* [1988] arrived at a similar conclusion using a frequency-domain

inversion approach. *Ida* [1990] found that optimal array geometry for a strike-slip fault requires stations well spaced in azimuth along with near-fault stations. Using the beam-forming technique, *Huang and Huang* [2004] showed that inversion results depend on the array configurations they used. None of these studies aimed at inferring systematically the rise-time resolution. By prescribing a pulse-like rupture similar to the Haskell pulse where rise time and rupture velocity are fixed we simulate ground velocities. Using the simulated ground velocities as data in a generalized source inversion approach that is a synthesis of the best of the methods and parametrizations available, we invert for slip rate on the fault plane to address the following questions: How narrow are the pulses that can be resolved with a particular network? How does rupture velocity affect the rise-time assessment? What happens if closely spaced data comes at the expense of much higher noise levels? Though the source inversion method outlined here is a medley of widely used procedures to invert for slip models, we validate our inversion method by rerunning the inversion for a published problem setup and comparing against their [*Konca et al.*, 2013] results as a benchmark.

## 4.1 Problem formulation

Given the three-component data (ground velocities) for an earthquake at certain receiver locations, we need to find the two-component slip rate on an assumed fault plane. The data and slip rate are related to each other through the Green's functions (GFs) of the medium:

$$\mathbf{G}\mathbf{m} = \dot{\mathbf{d}}, \quad (4.1)$$

where  $\mathbf{m}$  is the slip rate on the fault plane,  $\dot{\mathbf{d}}$  is the data (ground velocities) and  $\mathbf{G}$  is the Green's function matrix.

In the case of one fault cell (or a point source), data at any arbitrary location can be computed as a convolution of the slip rate on the fault cell with the Green's function relating the fault cell and data locations. In shear ruptures where opening is

not permitted, the relative displacement rate turns into slip rate which has only two linearly independent components. So,  $\mathbf{G}$  is a 3 x 2 matrix,  $\mathbf{m}$  is a 2 x 1 vector, and  $\dot{\mathbf{d}}$  is a 3 x 1 vector.

In the case of finite faults, one can divide the fault into cells known as sub-faults and sum over the contribution of each of them to obtain data at any arbitrary location. This is equivalent to collecting all the slip rates from each sub-fault vertically in the model vector and collecting the corresponding GFs to the right of the  $\mathbf{G}$  matrix. When data is available at multiple locations, each of them can be stacked vertically in the data vector, collecting corresponding GFs to the bottom of  $\mathbf{G}$  matrix [Lee *et al.*, 2006].

## 4.2 Model parametrization

We adopt the multi-time window approach without any a priori constraints on hypocenter, rupture speed, rise time, or shape of the slip-time function. This allows in principle to resolve complex scenarios such as fault re-rupturing. The slip rate at each sub-fault is expressed as a linear combination of boxcar temporal basis functions, leading to a linear inverse problem. Spatial basis functions are boxcars over each sub-fault. Since we do not limit the number of time windows, our scheme can be called “*unrestricted multiple time window*”. In principle, the model discretization in time is similar to the classical ‘multi-time window’ method introduced by *Hartzell and Heaton* [1983], but the implementations of that approach are typically limited to about 10 windows [Hartzell and Langer, 1993].

## 4.3 Green’s functions

We generate Green’s functions (GFs) up to frequencies of 5 Hz, higher than the cut-off frequency of 1 Hz used in our inversions. We use the reflectivity method [Herrmann, 2001; Fuchs and Müller, 1971; Berman, 1997] for calculating the near-field full waveform GFs. A database of GFs covering all possible distances and azimuths in the

densest configuration of stations is computed beforehand and used throughout this study. The same GFs are used both in kinematic forward simulations to generate data as well as in the inversions. In other words, we assume that the velocity model is known in complete detail. The velocity model used here is a homogenous half-space with  $V_p = 5.6$  km/s,  $V_s = 3.2$  km/s and  $\rho = 2.67$  g/cm<sup>3</sup>. An approach that does not need calculating GFs for inversion is described in Chapter 2.

## 4.4 Inversion method

We formulate our cost function as:

$$\chi(\mathbf{m}) = \int_0^T \sum_{r=1}^n [\dot{\mathbf{s}}(\mathbf{x}_r, t, \mathbf{m}) - \dot{\mathbf{d}}(\mathbf{x}_r, t)]^2 dt, \quad (4.2)$$

where  $\dot{\mathbf{s}}$  is the synthetic data that depends on the “current” model while the actual data ( $\dot{\mathbf{d}}$ ) depends on the “original” source. Note that both data and synthetics are given by the same Equation (4.1) except that  $\mathbf{m}$  is the true source in the case of data and is the model in the case of synthetics. It is easy to see from the cost function that equal weighting is given to the data from each station. Incorporating a weighting matrix to weight stations differently would not conceptually change the rest of the formulation.

Starting with no prior (zero initial guess) information, we use a conjugate-gradient (CG) algorithm to minimize the cost function [*Hestenes and Stiefel*, 1952; *Fletcher and Reeves*, 1964]. CG can be described briefly as follows:

1. Assume an initial model,  $\mathbf{m}^0$  (e.g., zero slip rate in space and time), and compute the corresponding synthetics,  $\mathbf{s}^0 = \mathbf{G} * \mathbf{m}^0$
2. Compute the residuals  $\mathbf{r}^0$  by subtracting the data from the synthetics,  $\mathbf{r}^0 = \mathbf{s}^0 - \mathbf{d}$
3. Compute the gradient of the cost function with respect to the model parameters,  $\boldsymbol{\gamma}^0 = \mathbf{G}^\dagger \mathbf{r}^0$ , where  $\mathbf{G}^\dagger$  is transpose of matrix  $\mathbf{G}$ .

4. Set the search direction,  $\mathbf{p}^0 = -\boldsymbol{\gamma}^0$
5. Then, for  $k=1,2,3,4,\dots$ , repeat the following:
  - (a) Compute new synthetics,  $\mathbf{s}^k = \mathbf{G} \mathbf{p}^k$ .
  - (b) Update the model so that the cost function is minimized along the search direction,  $\mathbf{m}^{k+1} = \mathbf{m}^k + \alpha \mathbf{p}^k$ , where  $\alpha = \langle \mathbf{r}^k, \mathbf{s}^k \rangle / \langle \mathbf{s}^k, \mathbf{s}^k \rangle$ .
  - (c) Update the residuals,  $\mathbf{r}^{k+1} = \mathbf{r}^k + \alpha \mathbf{s}^k$ .
  - (d) Compute the new gradient,  $\boldsymbol{\gamma}^{k+1} = \mathbf{G}^\dagger \mathbf{r}^{k+1}$ .
  - (e) Update the search direction applying the Polak-Ribiere formula [Polak and Ribière, 1969],  $\mathbf{p}^{k+1} = -\boldsymbol{\gamma}^{k+1} + \beta \mathbf{p}^k$  where  $\beta = \langle \boldsymbol{\gamma}^{k+1} - \boldsymbol{\gamma}^k, \boldsymbol{\gamma}^{k+1} \rangle / \langle \boldsymbol{\gamma}^k, \boldsymbol{\gamma}^k \rangle$ .
  - (f) If the norm of the new search direction  $\mathbf{p}^{k+1}$  is less than a prescribed tolerance (e.g., 1e-4) stop. Otherwise, increment the iteration counter,  $k \leftarrow k + 1$ , and go to step 5(a).

Since the approach is constructed based on the adjoint operator  $\mathbf{G}^\dagger$  and works for the linear formulation in terms of slip rate, we call it “*adjoint linear slip rate inversion*”. In Section 4.2 we classified our inversion as “*unrestricted multiple time window*” method. Combining the method formulation and parameterization, we name our method as “*adjoint linear slip rate inversion*” with “*unrestricted multiple time window*” parameterization.

## 4.5 Benchmarking

To test the performance of our method, we run dynamic rupture simulations in a geometry similar to the work of Konca *et al.* [2013], carry out inversions using the method described here, and compare the results to the simulated source and to the inversion results of Konca *et al.* [2013]. In particular, we focus on scenario 1 of Konca *et al.* [2013]. This scenario is a crack-like rupture breaking the surface. The rupture initiates from a nucleation patch (Figure 4.1) and propagates spontaneously governed

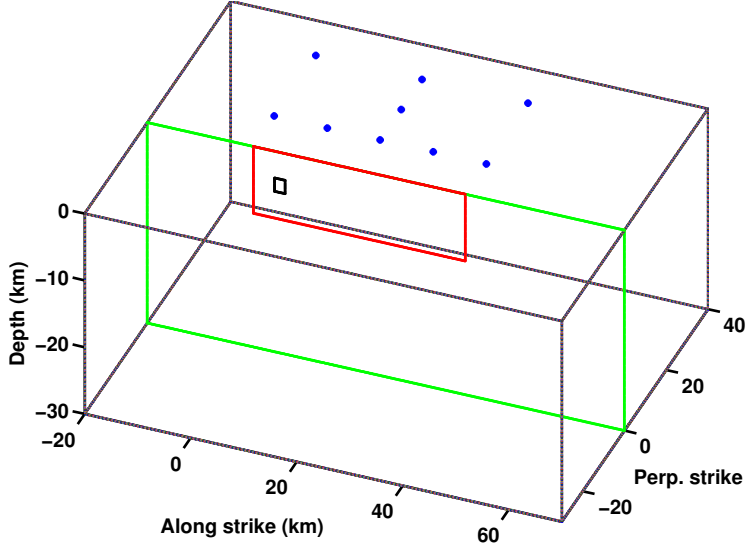


Figure 4.1: Geometry of the problem. The fault is indicated by red rectangle. Stations are shown in blue dots.

by slip-weakening friction. For more details see *Konca et al.* [2013]. We choose similar geometry and station setup (Figure 4.1) as in *Konca et al.* [2013], except we only use the velocities from the strong motion stations in our inversion, without the geodetic measurements of final displacements used in *Konca et al.* [2013]. In Figure 4.1, the fault is shown as a red rectangle and the extended plane from the fault is shown in green. Stations are marked by blue dots. All stations are on the free surface. There are a total of nine stations of which five stations are placed symmetrically at 10 km offset from the fault, one station at 20 km offset from the fault half way along the strike, and three stations at 30 km offset from the fault symmetric along strike. The horizontal spacing of the first set of five stations is 10 km and that of the last set of three stations is 20 km. The simulations are conducted using the 3D wave propagation code SPECFEM3D [*Komatitsch et al.*, 2010] in which we implemented extended kinematic sources represented by slip on a fault plane using the split-nodes approach.

Figure 4.2(a) shows the snapshots of the input and inverted slip rate in the left and right columns, respectively. Figure 4.2(b) shows the input and inverted slip rate from *Konca et al.* [2013]. Figure 4.3(a) shows the input (top) and inverted (bottom)

final slip from our inversion and Figure 4.3(b) from *Konca et al.* [2013]. We find that the approach described here can invert for the input source in a way comparable to those of previous studies, if not slightly better in resolving the visual details of slip rate (Figure 4.2), by considering only data from the strong motion station locations. Final slip in our inversion might improve if the GPS constraint is added. Both average slip and average slip rate are within 1% from input values while peak values are off by 6%.

## 4.6 Resolution of rise time for pulse-like ruptures

### 4.6.1 Problem setup

All rupture scenarios considered in sections hereafter have a fixed moment magnitude of 7.0 and occur on a rectangular vertical fault of dimensions 40 km x 15 km. The sub-fault size is chosen to be 0.5 km. The average slip on the fault is nearly 2 m. Stations of a fixed spacing on the surface extend as far as two fault lengths away on each side, giving a good surface coverage of 200 km x 160 km. No station is placed along the strike of the fault plane (Figure 4.4).

Our goal is to investigate the rise-time resolution for different station spacings. For this purpose, we consider a fixed-width slip pulse of a certain shape propagating at a constant speed along the strike of the fault plane. Two different pulse shapes are selected, boxcar and Yoffe [Yoffe, 1951]. The terms “boxcar pulse” and “Haskell pulse” are used interchangeably in the following. Rise times ranging from 0.5 to 4 s with the increment of 0.5 s are considered. For a fixed rise time, we also vary rupture velocity to see its influence on the rise-time resolvability. Rupture velocities ranging from 1 to 5 km/s with the increment of 0.5 km/s are selected. The slip-time function on a sub-fault is represented by three parameters: rise time  $T_r$ , rupture velocity  $V_r$  and slip  $D$ . We note that the problem addressed here is linear in slip, and so a parameter study over slip is not necessary. The different kinds of scenarios considered here are summarized in Table 4.1

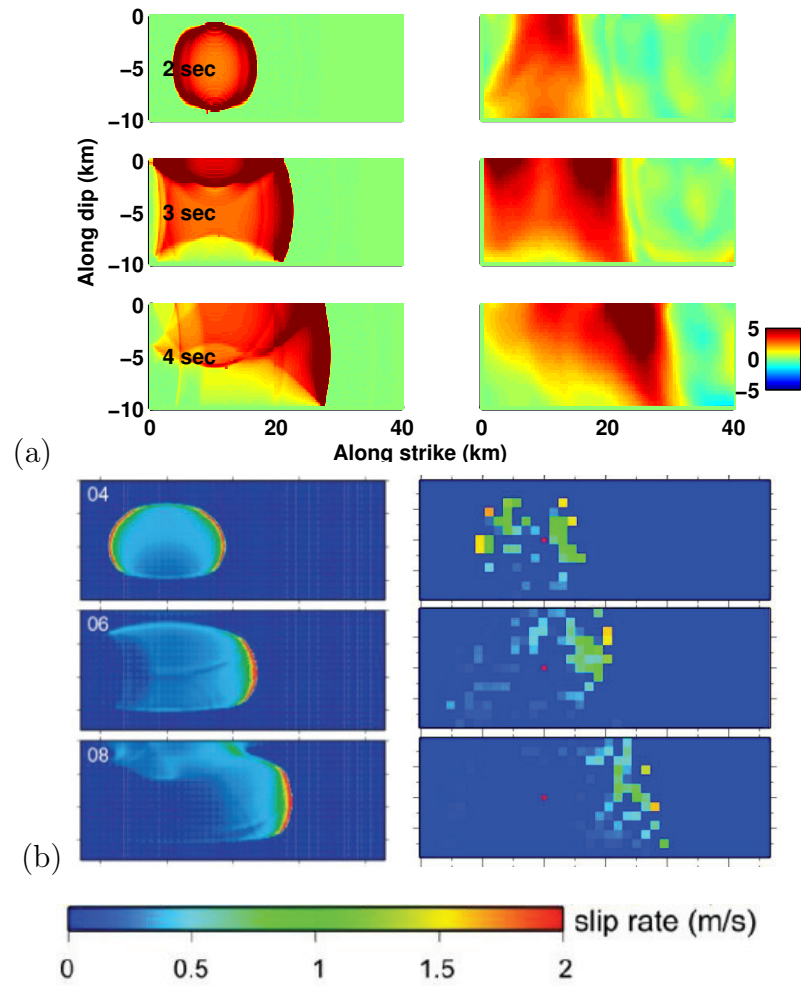


Figure 4.2: Comparison of the input slip rate and the inverted slip rate at three different times. (a) Inversion using our method. (b) Inversion shown in *Konca et al.* [2013]. In both cases first column shows input snapshots and second column shows inverted snapshots. Our inversion method seems to resolve equally well the slip rate visually, if not better, when compared with *Konca et al.* [2013].

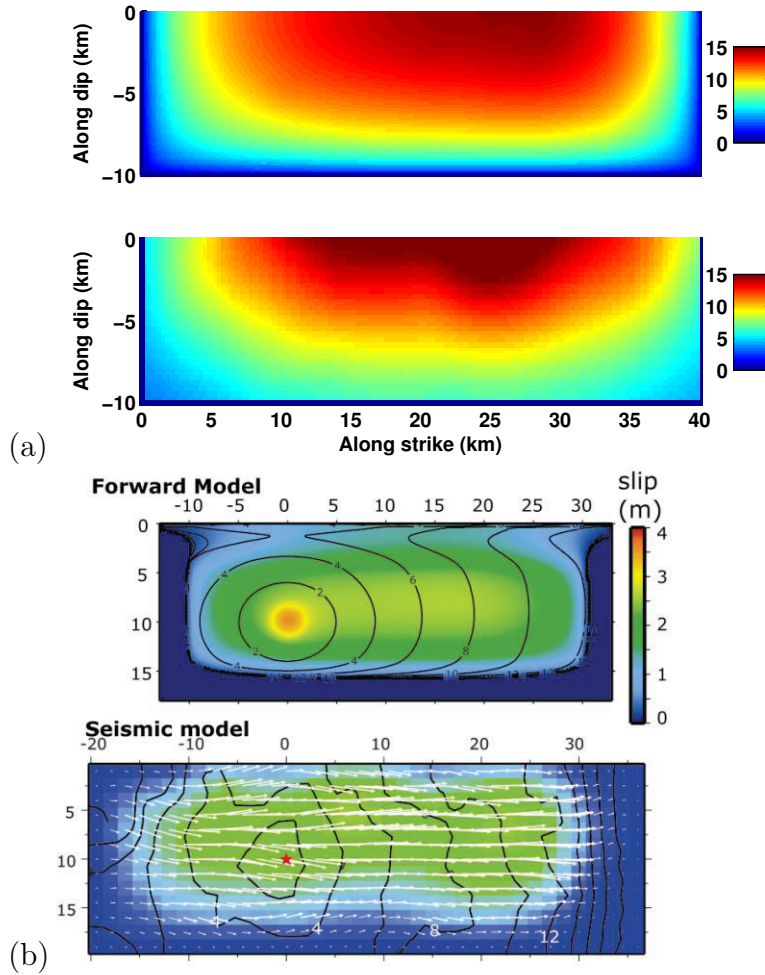


Figure 4.3: Comparison of the input final slip and the inverted final slip. (a) Inversion using our method. (b) Inversion shown in *Konca et al.* [2013]. In both cases top panel shows input slip and bottom panel shows inverted slip. Our inversion method does not seem to do well in terms of slip when compared with *Konca et al.* [2013] as we do not consider the GPS data.

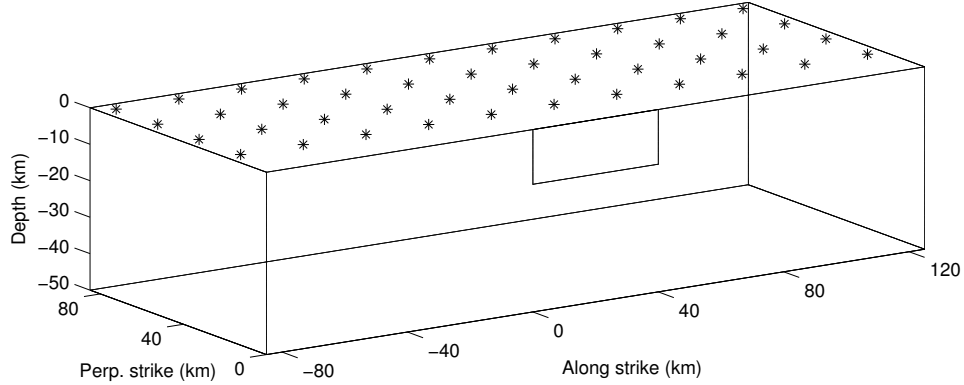


Figure 4.4: Geometry of the problem setup for all the scenarios considered in the rise-time study. The station configuration is shown for 20 km station spacing but various network spacings are considered in this study. For a given network spacing, the closest station to the fault is as close as the spacing between stations.

	Haskell	Yoffe	Haskell	Noise Haskell
	$(V_r=2 \text{ km/s})$	$(V_r=2 \text{ km/s} \ \& \ V_r=5 \text{ km/s})$	$(T_r=1 \text{ sec})$	$(T_r=1 \text{ sec})$
2 km	$T_r=0.5 \text{ to } 4 \text{ s}$	$T_r=0.5 \text{ to } 4 \text{ s}$	$V_r=1 \text{ to } 5 \text{ km/s}$	$1 \text{ cm/s noise}$ $V_r = 2 \text{ km/s} \ \& \ V_r = 3 \text{ km/s}$
4 km	$T_r=0.5 \text{ to } 4 \text{ s}$	$T_r=0.5 \text{ to } 4 \text{ s}$	$V_r=1 \text{ to } 5 \text{ km/s}$	
5 km	$T_r=0.5 \text{ to } 4 \text{ s}$	$T_r=0.5 \text{ to } 4 \text{ s}$	$V_r=1 \text{ to } 5 \text{ km/s}$	
8 km	$T_r=0.5 \text{ to } 4 \text{ s}$	$T_r=0.5 \text{ to } 4 \text{ s}$	$V_r=1 \text{ to } 5 \text{ km/s}$	
10 km	$T_r=0.5 \text{ to } 4 \text{ s}$	$T_r=0.5 \text{ to } 4 \text{ s}$	$V_r=1 \text{ to } 5 \text{ km/s}$	
20 km	$T_r=0.5 \text{ to } 4 \text{ s}$	$T_r=0.5 \text{ to } 4 \text{ s}$	$V_r=1 \text{ to } 5 \text{ km/s}$	Noiseless $V_r = 2 \text{ km/s} \ \& \ V_r = 3 \text{ km/s}$
40 km	$T_r=0.5 \text{ to } 4 \text{ s}$	$T_r=0.5 \text{ to } 4 \text{ s}$	$V_r=1 \text{ to } 5 \text{ km/s}$	

Table 4.1: Various sets of scenarios examined. Yoffe and Haskell pulses are both tested for various rise times and network spacings in the subshear case. The same setup is used to repeat the supershear case for Yoffe pulse. Fixing the rise time, the rupture velocity dependency is examined using a Haskell pulse. Finally, noise is added to dense network for end-member cases of rupture velocity and for a fixed rise time.

A solution to an inverse problem is crucially dependent on the sensor network geometry. Here, we use uniformly spaced networks, with spacing between stations of 2 km, 4 km, 5 km, 8 km, 10 km, 20 km, 40 km, where the densest station configuration is chosen to mimic the spacing of next-generation earthquake recording systems [Michel *et al.*, 2013] possible from an optical satellite imaging, and the coarsest resembles the spacing of best available current ground-based sensors. A given network spacing also indicates that the closest station to the fault is exactly at a perpendicular distance of its network spacing.

### 4.6.2 Misfit metrics

We show some plots in data space and model space on how the error metrics vary as a function of space, time or iteration number. Specifically, we use  $T_r = 1$  sec and  $V_r = 2$  km/s to illustrate the trends in these plots. These trends are preserved even for other cases considered in this study except that convergence is faster or slower depending on the shift in rupture velocity and rise time from the reference value for which they are presented.

The misfit function is defined by Equation 4.2. For our choice, the misfit function is the same as variance and its ratio to variance of the data gives the normalized variance as shown in Figure 4.5. In this case, normalized variance reduction of 99% is achieved in about 50 iterations. Denser networks tend to have faster reduction in normalized variance than coarser networks.

The Root Mean Square (RMS) error of the model at any iteration is defined as

$$\Psi^2(\mathbf{m}) = \int_0^T \sum_{s=1}^{N_{sub-fault}} [\mathbf{m}(\mathbf{x}_s, t) - \mathbf{m}^0(\mathbf{x}_s, t)]^2 dt$$

where  $\mathbf{m}$  is the model and  $\mathbf{m}^0$  is input source.  $k$  is the number of sub-faults.

The normalized model RMS error as a function of iteration number is shown in Figure 4.6. RMS error is normalized with the difference between maximum and minimum values. Figure 4.6 shows that the normalized RMS error decreases to a similar extent for all networks in the initial iterations and saturates there. Conjugate-gradient method retrieves the projection of true model onto the space orthogonal to

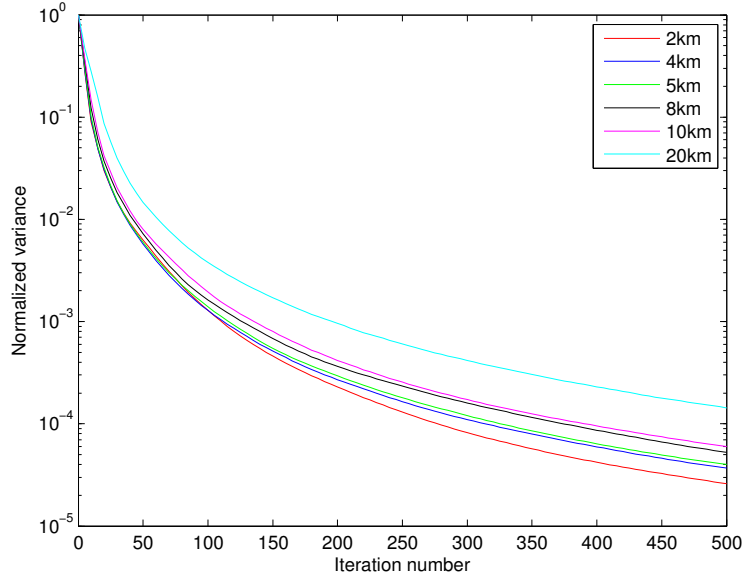


Figure 4.5: Normalized variance as a function of iteration number. Denser networks produce more rapid reduction in normalized variance than a sparser network.

the null space which happens in about 10 iterations for the case considered here. Instead of integrating in both space and time, integrating only in time gives the spatial variation  $\Psi^2(\mathbf{m}, \mathbf{x}_s) = \int_0^T [\mathbf{m}(\mathbf{x}_s, t) - \mathbf{m}^0(\mathbf{x}_s, t)]^2 dt$  (Figure 4.7) of RMS of slip rate and just the summation over sub-faults gives the temporal variation  $\Psi^2(\mathbf{m}, t) = \sum_{s=1}^{N_{sub-fault}} [\mathbf{m}(\mathbf{x}_s, t) - \mathbf{m}^0(\mathbf{x}_s, t)]^2$  (Figure 4.8) of the RMS of slip rate. Figure 4.7 shows that the spatial variation of slip-rate RMS seems to exhibit a pattern that is related to the station spacing of the network. The temporal variation of slip rate is higher (Figure 4.8) for the duration of the source (for  $V_r=2$  km/s and fault length of 40 km, rupture takes 20 sec to reach the other end of the fault) than the rest of simulation time.

The RMS error can also be calculated for slip in a similar fashion as it is done for slip rate.

$$\Phi^2(\mathbf{m}) = \int_0^T \sum_{s=1}^{N_{sub-fault}} [\delta(\mathbf{x}_s, t) - \delta^0(\mathbf{x}_s, t)]^2 dt$$

where  $\delta$  is slip at any given iteration and  $\delta^0$  is the input slip. The slip can be computed from the model as  $\delta = \sqrt{\delta_x^2 + \delta_z^2}$ , where  $\delta_x = \int_0^T m_x dt$ ,  $\delta_z = \int_0^T m_z dt$ ,  $m_x$  is the along strike component and  $m_z$  is the along dip component of slip rate. Note that

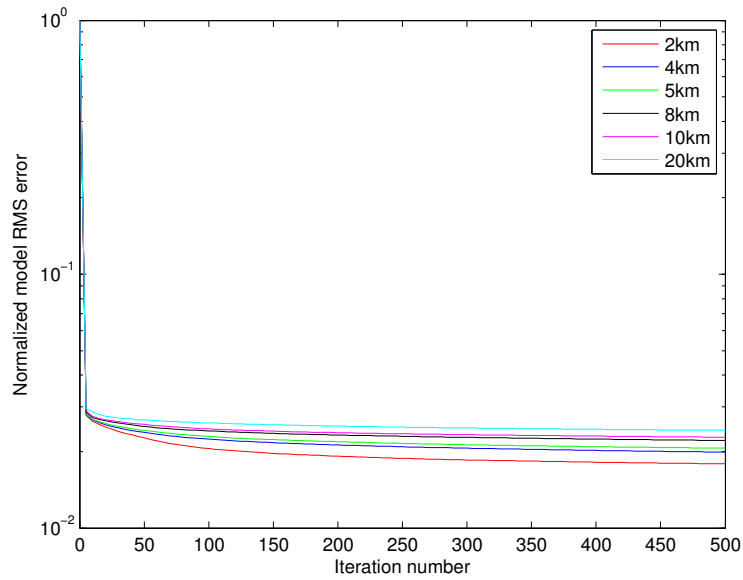


Figure 4.6: Normalized RMS error of slip rate as a function of iteration number. The RMS error in slip rate decreases more than 90% with denser networks performing better than coarser networks.

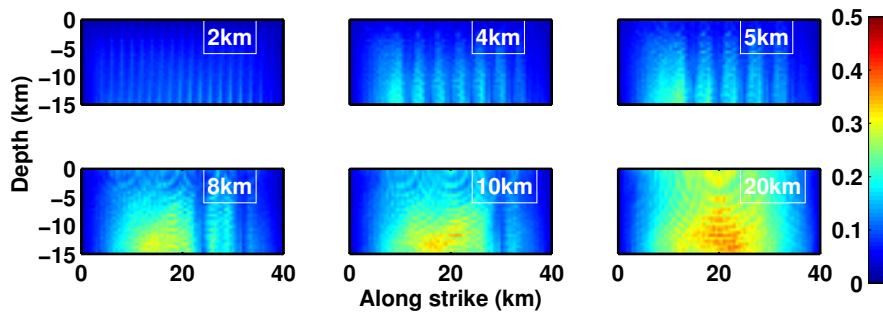


Figure 4.7: Normalized RMS error of slip rate in space. Coarser networks have a higher RMS error in the central region of the fault while the dense network has a uniform reduction of about 90% everywhere on the fault plane.

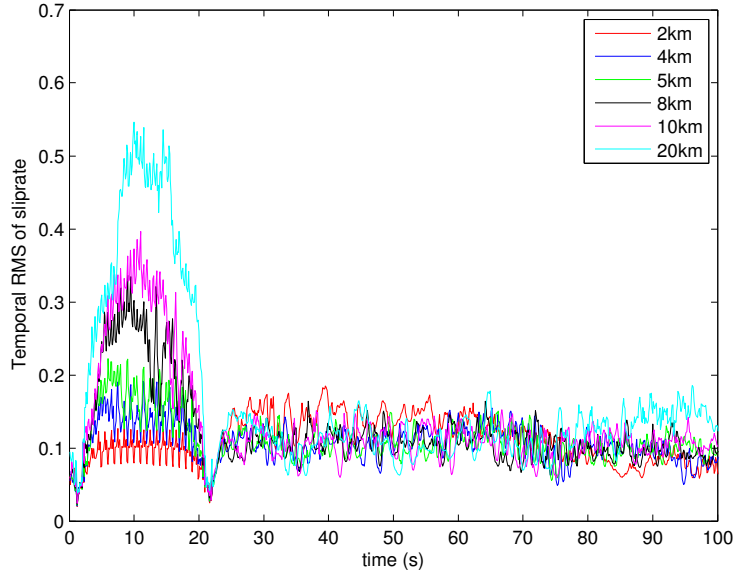


Figure 4.8: Normalized RMS error of slip rate as a function of time averaged over the entire fault plane. The dense network has only about 10% RMS error overall while the coarse network has approximately 50% RMS error during the time for which rupture lasts on the fault plane.

the integrals for calculating slip are cumulative integrals in time. The variation of the normalized RMS error of slip is shown in Figure 4.9. Normalization is done by dividing the RMS error with the difference between maximum and minimum values of slip. In our formulation, slip at long periods gets zero weighting and so it takes more iterations for slip to saturate (Figure 4.9) than the number of iterations taken by slip rate to saturate (Figure 4.6). Summing the RMS error over the sub-faults gives the temporal variation  $\Phi^2(\mathbf{m}, t) = \sum_{s=1}^{N_{sub-fault}} [\delta(\mathbf{x}_s, t) - \delta^0(\mathbf{x}_s, t)]^2$  (Figure 4.11) and integrating with respect to time gives the spatial variation  $\Phi^2(\mathbf{m}, x_s) = \int_0^T [\delta(\mathbf{x}_s, t) - \delta^0(\mathbf{x}_s, t)]^2 dt$  (Figure 4.10) of the RMS of slip. The spatial pattern of the RMS of slip (Figure 4.10) is not so evident as it was in case of slip rate. Similar to the temporal pattern of the RMS of slip rate, temporal variation of the RMS of slip also shows also different behavior for the duration of source than rest of the simulation time (Figure 4.11). However, the temporal variation of the RMS of slip is lower for the duration of source. The increase in temporal variation of the RMS of slip after the source duration could be because the final slip gets near zero weight at long periods for the cost function

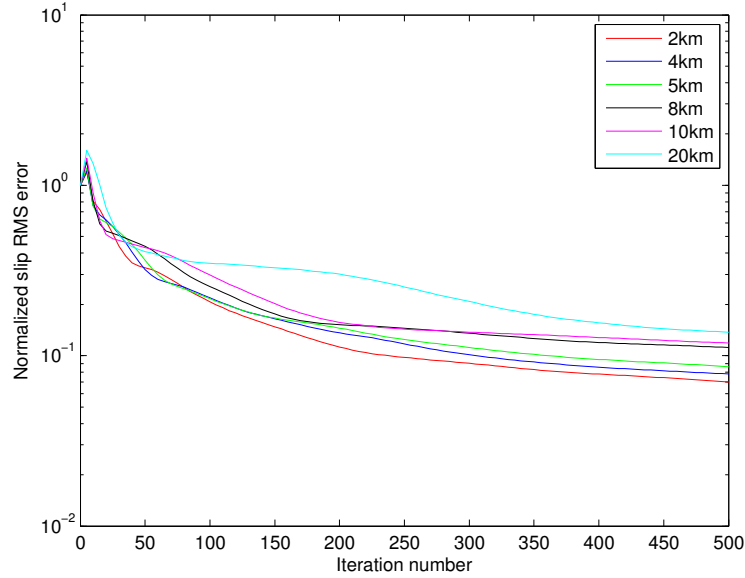


Figure 4.9: Normalized RMS error of slip as a function of iteration number. The RMS error in slip increases during the initial iterations eventually decreasing by an order of magnitude, with denser networks giving less RMS error than their coarser counterparts.

we used.

### 4.6.3 Effect of network spacing on resolving rise time

Our goal is to investigate the rise-time resolution for different station spacings. Rise times ranging from 0.5 to 4 s with the increment of 0.5 s are considered. For a fixed rise time, we also vary rupture velocity to see its influence on the rise-time resolvability. Rupture velocities ranging from 1 to 5 km/s with the increment of 0.5 km/s are selected. The slip-time function on a sub-fault is represented by three parameters: rise time  $T_r$ , rupture velocity  $V_r$  and slip  $D$ . We note that the problem addressed here is linear in slip, and so a parameter study over slip is not necessary.

Figure 4.12 shows a representative snapshot of slip rate for inversions of slip pulses with various rise times and network spacings, all with the rupture velocity of 2 km/s. For the rise times as short as 1 s, only the densest station configuration, with the spacing of 2 km, shows spatial pattern of slip rate that resembles the input slip rate.

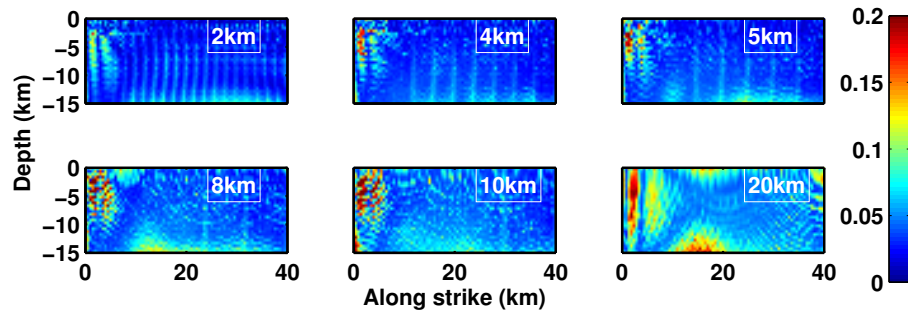


Figure 4.10: Normalized RMS error of slip in space. The spatial RMS error in slip is lower compared to the spatial RMS error in slip rate (Figure 4.7).

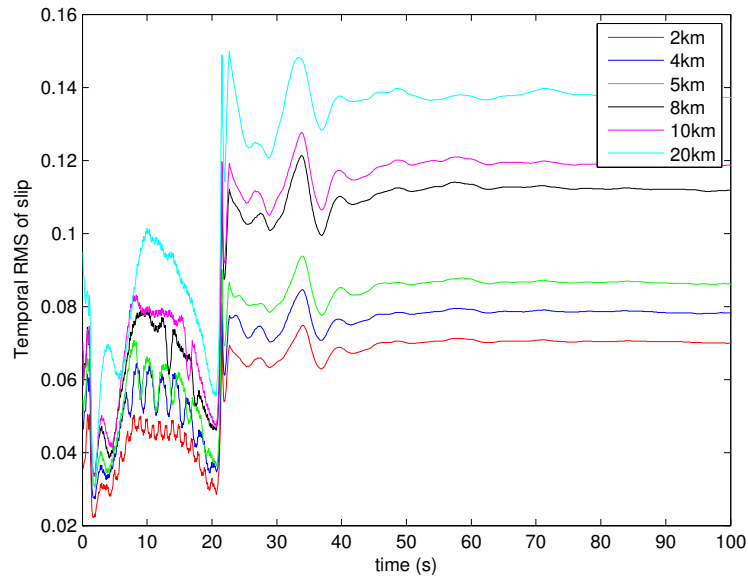


Figure 4.11: Normalized RMS error of slip in time averaged over the entire fault plane. Errors in the final slip decrease with increasing network spacing.

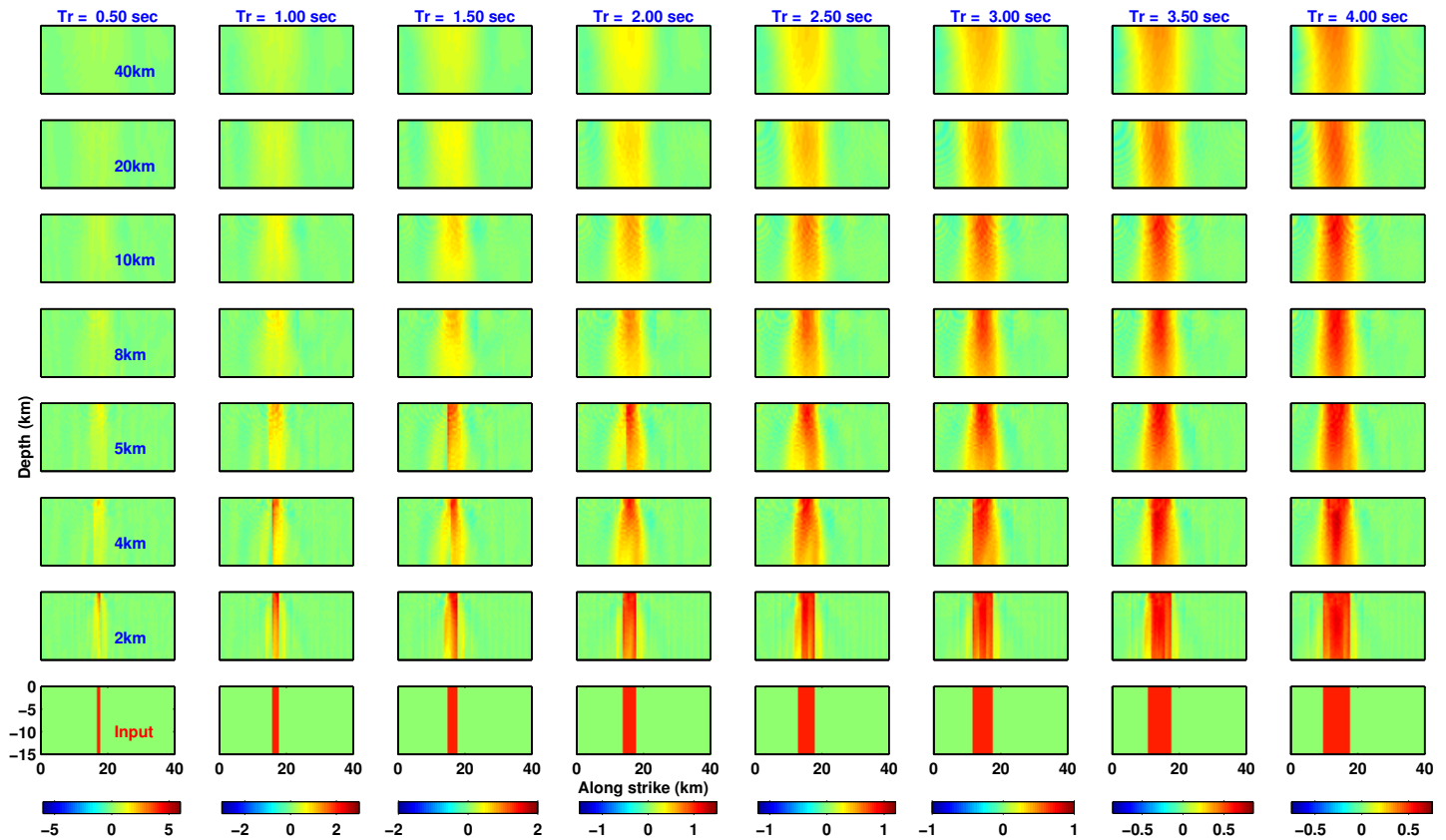


Figure 4.12: Trade-off between network spacing and pulse width for a square Haskell pulse propagating at  $V_r = 2$  km/s. Rows show inversions for different network spacings with bottommost row showing the input. Columns correspond to a representative snapshot from scenarios with rise times 0.5 sec, 1 sec, 1.5 sec, 2 sec, 2.5 sec, 3 sec, 3.5 sec, and 4 sec, respectively. Coarser networks have trouble resolving shorter rise times.

As the spacing between stations increases, the slip pulse smears out over a region wider than the input pulse width. As the station spacing gets as coarse as 40 km, there is barely any sign of the pulse. Changing the pulse shape from boxcar to Yoffe had little effect on resolution in comparison to the input (Figure 4.13). We also consider a rise time of 0.5 sec but its resolution is poor, as expected, since one cannot resolve rise times that short while using a filter with the cut-off frequency of 1 Hz. Filters higher than 1 Hz cannot be confidently used in source inversion due to the poor knowledge about the crustal velocity structure [Ide *et al.*, 2005; Ide, 2007]. For the longer rise times of 4 sec, the pulse width as well as the peak slip rate are well constrained in inversions from dense datasets. Coarser networks broaden the pulse and decrease the peak slip rate. A commonly observed issue of loss of resolution with depth [Page *et al.*, 2009; Custódio *et al.*, 2009] is also evident in Figure 4.12.

Quantitative estimation of the goodness of the inverted rise-time values can be obtained from the slip-rate distribution. Since we do not impose non-negativity and smoothing constraints, slip rate exhibits an oscillatory behavior at the onset and cessation of slip. Hence we use slip accumulation to estimate the rise time. Specifically, we compute the rise time as the time taken for slip on a sub-fault to go from 20% to 80% of its final value. The rise-time estimates obtained for each sub-fault are converted into one nondimensional number for the entire fault plane by taking the ratio of the median value of the rise time over the whole fault to that of the input rise time. Repeating this rise-time calculation for each input rise time and network spacing in Figure 4.12, a contour plot is constructed for the inverted rise time (Figure 4.14). Values of 1 indicate good recovery of the rise time, with higher values indicating progressive smearing of the slip pulse. Selecting an acceptable value for the goodness of the recovered rise time (e.g., a factor of 2) partitions the parameter space into two regions, one of which (that of shorter rise times and sparser networks, top left in Figure 4.14) is unreliable. The dotted line shows  $\Delta x = V_r T_r$ , where  $\Delta x$  denotes network spacing and  $V_r$ ,  $T_r$  are rupture velocity and rise time respectively. One would expect the partitioning of reliable and unreliable to be somewhere close to this dotted line but this is not the case, as seen in Figure 4.14. Hence, one should be careful while

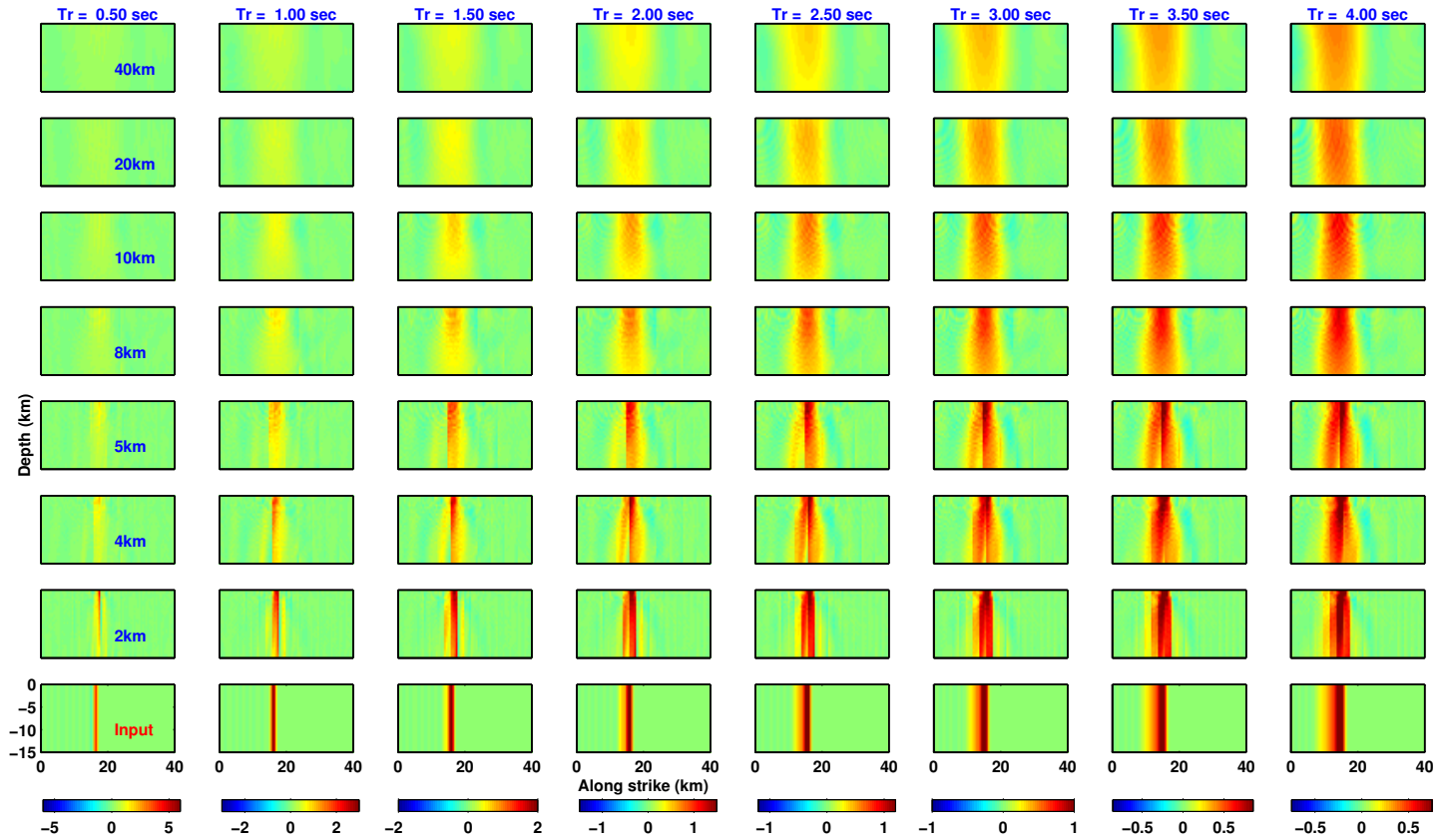


Figure 4.13: Trade-off between network spacing and pulse width for a Yoffe pulse propagating at  $V_r = 2 \text{ km/s}$ . Rows show inversions for different network spacings with bottommost row showing the input. Columns correspond to a representative snapshot from scenarios with rise times 0.5 sec, 1 sec, 1.5 sec, 2 sec, 2.5 sec, 3 sec, 3.5 sec and 4 sec, respectively. Coarser networks have trouble resolving shorter rise times.

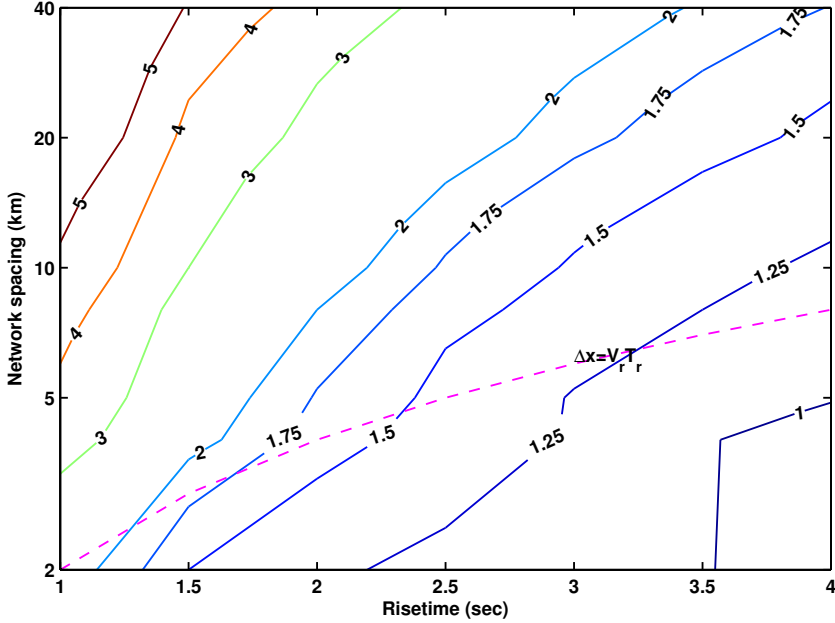


Figure 4.14: Contours of the ratio of the median rise-time estimates over the entire fault from the model to that of the input median rise time, for  $V_r = 2$  km/s. Contour labeled 2 partitions the parameter space into two of which the top-left portion is unreliable.

interpreting inverted rise times shorter than 2.5 s [Chen *et al.*, 1991; Huang *et al.*, 2001; Hernandez *et al.*, 2001; Bernard *et al.*, 1997] when they are obtained based on network spacings of tens of km using a filter with the corner frequency of 1 Hz.

#### 4.6.4 Effect of rupture velocity on resolving rise time

The rupture velocity can affect the resolvability of the source parameters, including the rise time. In particular, supershear ruptures do not have particle velocities decaying as fast as subshear ruptures away from the fault [Aagaard and Heaton, 2004; Bernard and Baumont, 2005] owing to the presence of well-known Mach wave the amplifies high frequencies [Bizzarri and Spudich, 2008]. Variable rupture speed decreases coherence in Mach front and reduces peak ground velocity [Bizzarri *et al.*, 2010], That is why we repeat the study of Section 4.6.3 for a supershear rupture speed of  $V_r = 5$  km/s (Figure 4.15). The results (Figure 4.14) show that the resolution of the rise time is much better for the supershear case, as expected, with the rise time being resolved within a factor of 2 in all cases considered (Figure 4.16).

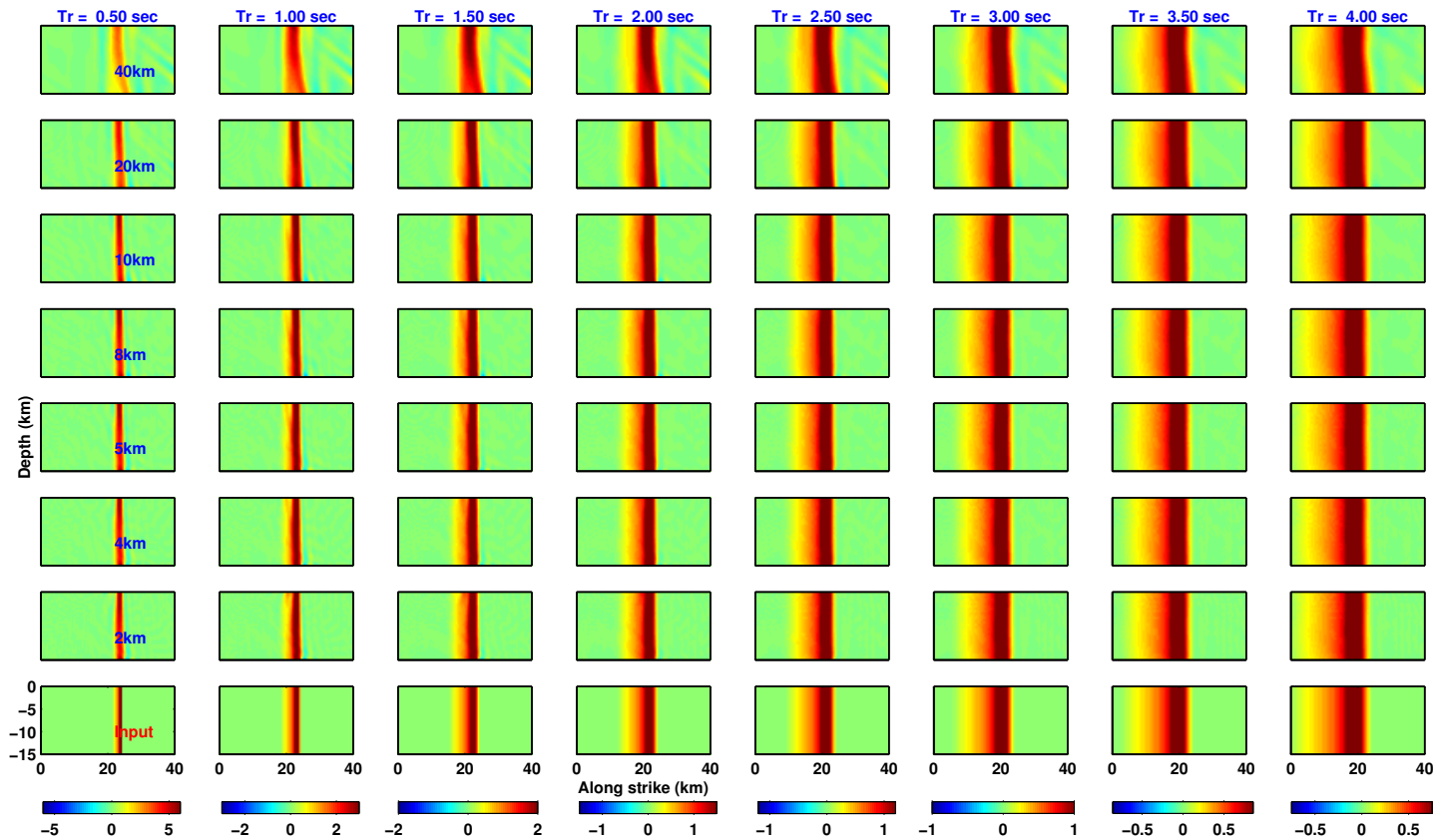


Figure 4.15: Trade-off between network spacing and pulse width for a Yoffe pulse propagating at  $V_r = 5$  km/s. Rows show inversions for different network spacings with the bottommost row showing the input. Columns correspond to a representative snapshot from scenarios with rise times 0.5 sec, 1 sec, 1.5 sec, 2 sec, 2.5 sec, 3 sec, 3.5 sec, and 4 sec, respectively. Coarser networks have trouble resolving shorter rise times.

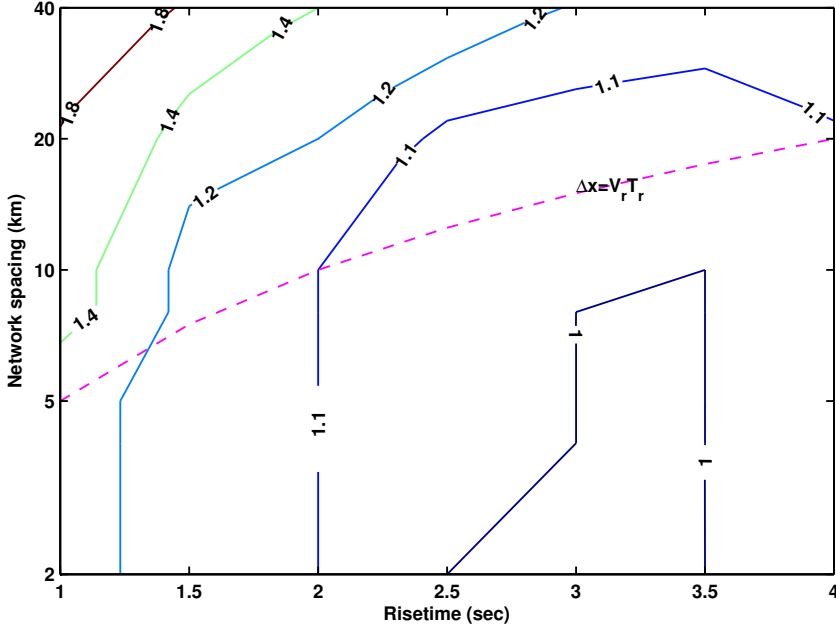


Figure 4.16: Contours of the ratio of the median rise-time estimates over the entire fault to the rise time of the input for  $V_r = 5$  km/s.

A plane wave approximation for a line fault in 2D can provide some rudimentary explanation for the better resolvability of supershear ruptures than subshear ruptures. Consider a shear rupture propagating at a rupture speed  $V_r = \omega/k$  along the strike (x-axis) of a fault, where  $\omega$  is the circular frequency and  $k$  is the wave number. The ground velocity is proportional to  $e^{i(-\omega t + kx + ly)}$  where  $k^2 + l^2 = \omega^2/c^2$  and  $c$  is a wave speed. The coefficient  $l$  in front of the off-fault coordinate  $y$  is then given by:

$$l^2 = \frac{\omega^2}{c^2} - k^2 = \omega^2 \left( \frac{1}{c^2} - \frac{1}{V_r^2} \right) \quad (4.3)$$

When  $c$  is the P-wave speed,  $l$  is always negative. However, for  $c = c_s$ ,  $l^2$  can be positive or negative depending on whether the rupture speed is supershear or subshear. The nature of waves change from propagating to exponentially decaying in the fault-normal direction as  $l^2$  changes sign from positive to negative. So, in the case of supershear ruptures, plane waves propagate much farther distance perpendicular to the fault. Additionally, one can define a penetration distance using the imaginary part of  $l$  for subshear ruptures as:

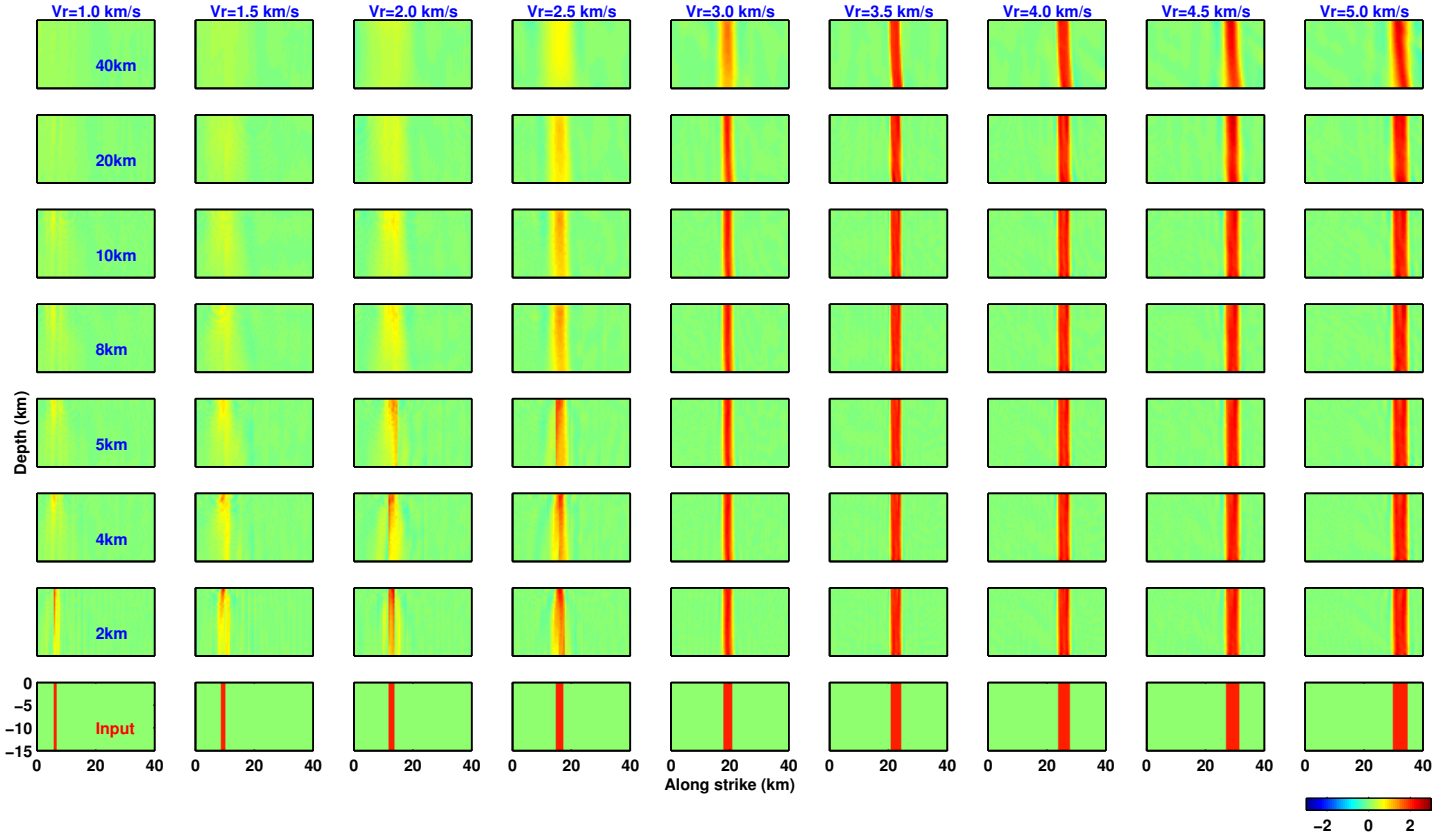


Figure 4.17: Trade-off between network spacing and rupture velocity for a square Haskell pulse with  $T_r = 1\text{sec}$ . Rows show inversions for different network spacings with bottommost row showing the input. Columns correspond to a representative snapshot from the scenarios with rupture velocity 1 km/s, 1.5 km/s, 2 km/s, 2.5 km/s, 3 km/s, 3.5 km/s, 4 km/s, 4.5 km/s and 5 km/s, respectively. In the supershear regime, rise times are well resolved by all the networks while in the subshear regime a dense network is required to resolve the rise time better.

$$y^* = \frac{1}{\mathbf{Im}(l)} = \frac{1}{\omega \sqrt{\frac{1}{V_r^2} - \frac{1}{c_s^2}}} = \frac{V_r}{2\pi} \frac{T_r}{\sqrt{1 - (V_r/c_s)^2}} \quad (4.4)$$

For subshear ruptures, therefore, station spacing has to be at least  $y^*$  to resolve the rise time  $T_r$  of a rupture propagating at  $V_r$ . Considering the  $V_r = 2\text{ km/s}$  case in Figure 4.19 which has a penetration distance of 2.5 km, resolution is good only for inversion with data from the 2 km network.

To confirm the anticipated dependence on rupture speed, we conduct inversions of

slip pulses with the rise time of 1 s propagating at a range of rupture speeds for various network spacings. A representative snapshot from each inversion is shown in Figure 4.17. Even a station spacing of few tens of kilometers gives a recovery qualitatively close to that of the input for the supershear regime, both in terms of pulse width and peak amplitude. For the subshear regime, however, there is a perceivable difference in the reconstructed source from sparse datasets compared to that from dense datasets. This can be explained by considering the peak ground velocity (PGV) as a function of the distance from the fault on a line of stations oriented perpendicular to the fault at its center (Figure 4.18). PGV decays relatively slowly with distance for cases with supershear rupture speeds, allowing propagation of the source information all the way to sparse stations. On the other hand, PGV for the cases with subshear speeds decays by more than an order of magnitude at about 10 km distance, not preserving the source information. A contour map of median value of recovered rise time over the fault as a ratio of prescribed rise time is also presented in rupture velocity network spacing parameter space (Figure 4.19). Supershear ruptures how good (factor of 1) resolvability of rise time even for station spacing up to 10 km while subshear ruptures always have a resolvability factor in excess of unity even for dense networks (Figure 4.19). Furthermore, rupture velocity as low of 1 km/s is very poorly resolved (factor of 10 off) when station spacing higher than 10 km is used.

While the recovery of the slip-rate profile exhibits much variation across rise times and rupture velocities, the recovery of total slip is barely affected by these parameters. Figure 4.20 shows the along-strike average of final slip on the fault plotted as a function of depth for the smallest and the largest rise time considered ( $T_r = 1$  s and  $T_r = 4$  s). The depth profiles of recovered slip are very similar for both end-member rise times in the subshear regime, where slip rate shows substantial variations in recovery. Variability in the shape of the slip profile with the network spacing is minimal, with the general trend of under-prediction at deeper portions of the fault with some minor over-prediction in the middle of the fault.

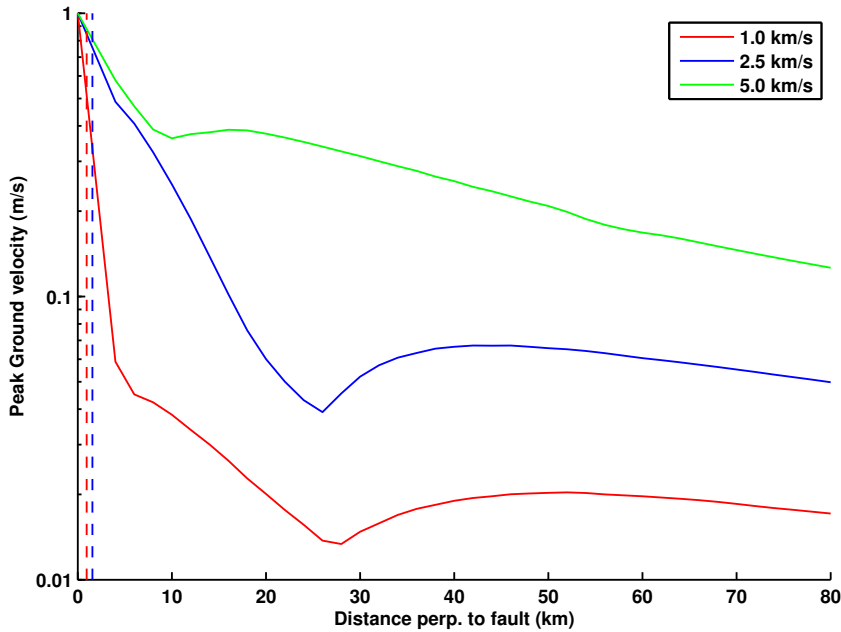


Figure 4.18: Peak ground velocity (PGV) as a function of distance from the fault for  $T_r = 1$  sec Haskell pulse considering different rupture velocities. The supershear ruptures have near flat dependence of PGV with distance.

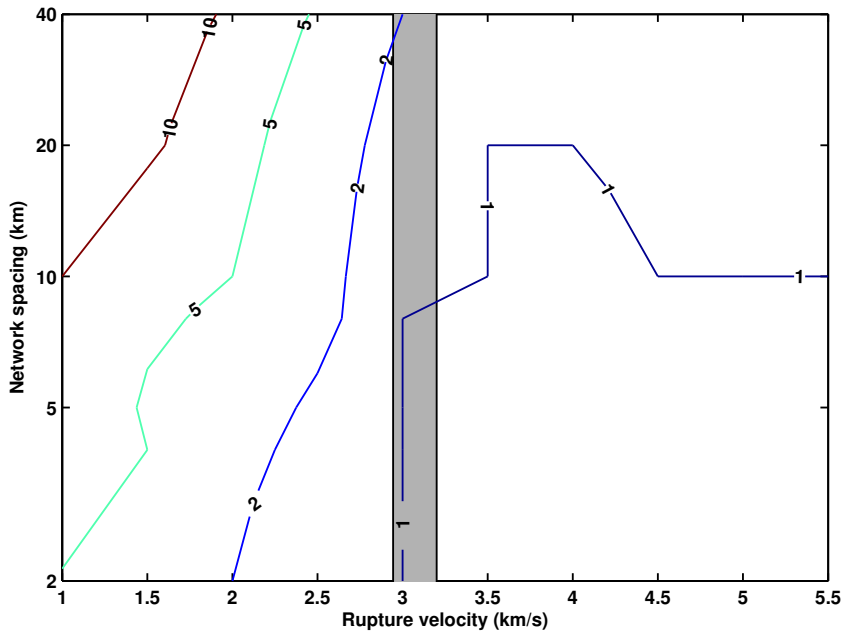


Figure 4.19: Contours of the ratio of the median rise-time estimates over the entire fault to rise time of input for  $T_r = 1$  sec. For supershear rupture velocities, all the networks seem to resolve the rise time well except possibly for the 40 km network spacing. In the case of sub-Rayleigh rupture speeds, a network spacing smaller than a km is required to get a good estimate of the rise time.

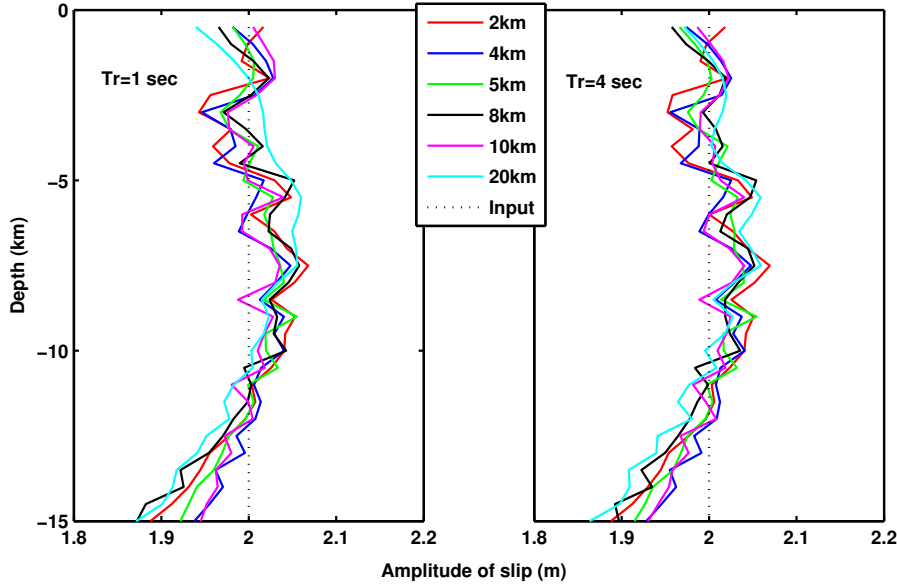


Figure 4.20: Profiles of the final slip averaged along strike plotted as a function of depth for different rise times (left)  $T_r=1$  sec and (right)  $T_r=4$  sec. Depth averaged slip recovery is almost independent of the rise time.

#### 4.6.5 Rise-time resolvability for variable rupture speed

The scenarios considered so far have a constant rupture speed over the entire fault plane. Let us consider a scenario with a variable rupture speed, in which rupture propagates with the speed of 2 km/s from 0 to 10 km along strike, 2.5 km/s from 10 to 20 km along strike, 2 km/s from 20 to 30 km, and finally 2.5 km/s from 30 to 40 km (the end of the rupture plane). Throughout the scenario, the rise time is kept constant at 1 s. We use data from a 4-km spaced network in this inversion. We choose this particular combination of the rise time and rupture speeds because, in the inversions with a constant rupture speed, the case of 2.5 km/s rupture speed has an improved resolution of the pulse width over that of 2 km/s rupture speed for 1 s rise time, when inverted with the 4-km-spaced network. Figure 4.21 shows the comparison of this inversion with the constant rupture speed inversions at mid-depth along strike in space-time plots. The space-time plots provide a consolidated view of rupture process along strike for a given depth. For Haskell pulses, rupture will be seen within a band of  $T_r$  sec having a slope of  $V_r$ . The portions during which the

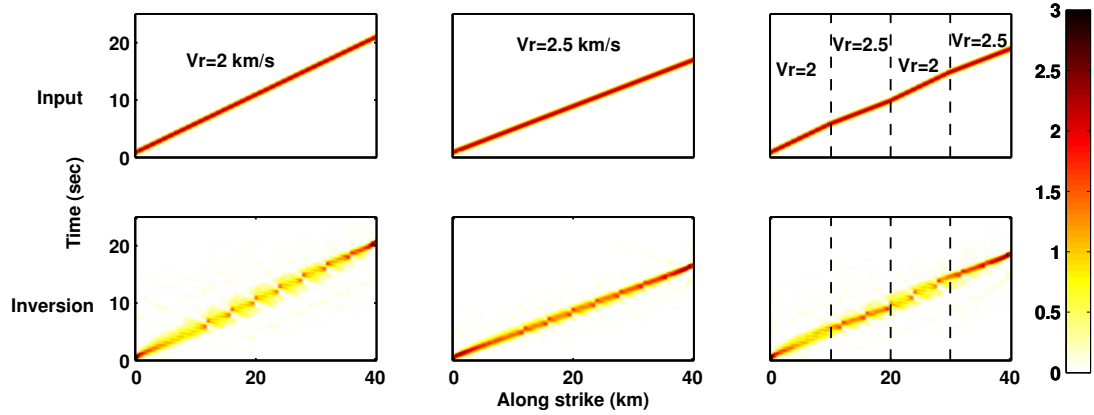


Figure 4.21: Space-time plot of the slip rate at mid-depth to test variable rupture velocity. A scenario with 2 km/s rupture velocity in  $0 < x \leq 10$  km,  $20 < x \leq 30$  km and 2.5 km/s in  $10 < x \leq 20$  km,  $30 < x \leq 40$  km gives inversion comparable to an overall rupture speed of 2 km/s in the regions where rupture speed is 2 km/s and comparable to an overall rupture speed of 2.5 km/s in the regions where rupture speed is 2.5 km/s.

rupture speed is slower, at 2 km/s, have poorer resolvability, similar to the inversion of the case with the 2 km/s constant rupture speed, while the portions with the faster rupture speed of 2.5 km/s have better resolution qualitatively comparable to that of the inversion of the case with the 2.5 km/s uniform rupture speed.

## 4.7 Trade-off between noise and network spacing

We consider the previously treated cases with two different rupture velocities one from each regime of resolvability of rise time. 3 km/s rupture velocity gave a good estimate (Figure 4.22) of rise time for both sparse (20 km) network as well as dense (2 km) network while 2 km/s rupture velocity (Figure 4.23) gave a poor estimate of rise time for sparse network. For each of the cases of rupture velocity, we add Gaussian uncorrelated noise of 1 cm/s to the data from dense network still keep the sparse network noiseless. It should be noted here that 1 cm/s noise added here is spatially uniform, unlike the noise typically added in source inversion studies that is expressed as some percentage of peak ground velocity. We see that the slip rate from inversions of dense network data with noise is nearly the same as that of inversion

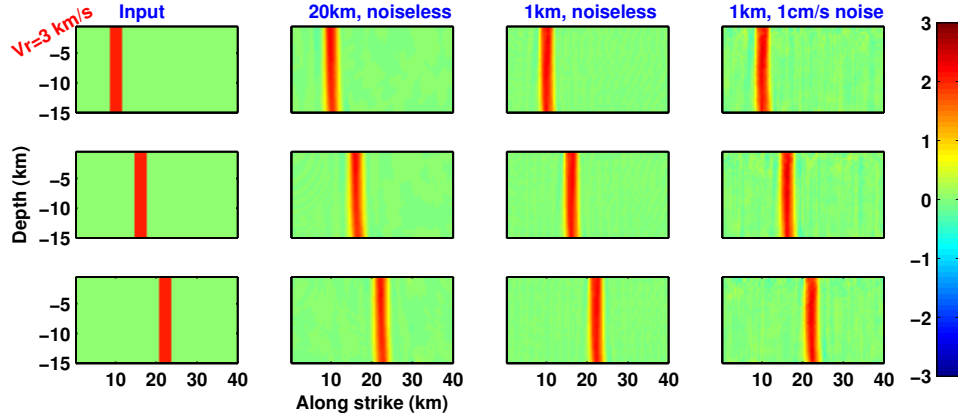


Figure 4.22: Slip rate snapshots from inversion with a noise of 1 cm/s added to the dense network data, and its comparison to its noiseless counterpart and a sparse network inversion for  $V_r=3$  km/s. The recovery of the dense network with 1 cm/s noise added to its data is qualitatively similar the dense network recover without noise.

based on dense network data without any noise, qualitatively. This indicates that the inversion based on data from the dense network with noise added to it has extracted all the information from the data except possibly for the intrinsic limitations of inverse problem.

## 4.8 Summary

We presented a consolidated method namely “adjoint linear source inversion” with ‘unrestricted multiple time window’ that do not involve any constraints. For subshear rupture velocities, network spacing has to be less than a penetration length that depends on rupture velocity and rise time, for qualitatively better (less than a factor of 2 over-prediction) recovery of rise time. Inverted models of supershear rupture speeds show almost identical recovery of width of pulse, independent of rise time and network spacing. Conclusions on rise-time resolvability are not dependent on the shape of pulse used. We verified this by using a Yoffe slip-rate function that is considered more realistic than the end-member boxcar pulse. Furthermore, rise-time resolvability for complicated sources with variable rupture speed can be found as superposition of its resolvability from constant rupture speed cases. Considering

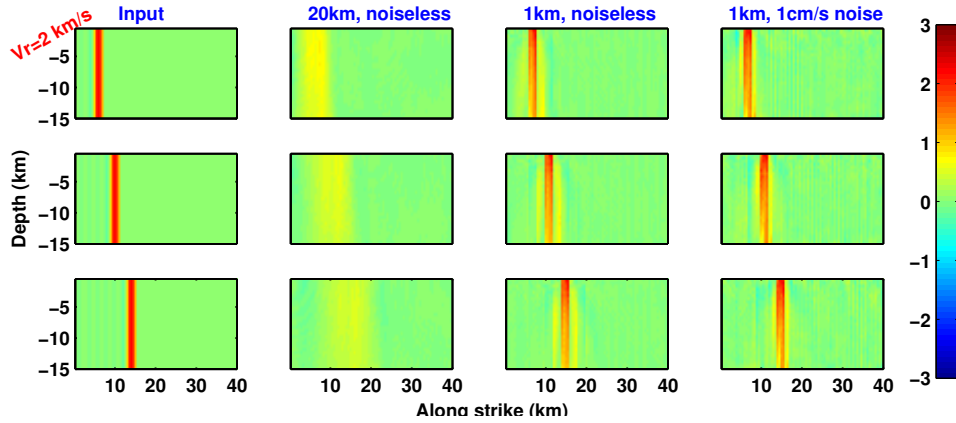


Figure 4.23: Slip rate snapshots from inversion with a noise of 1 cm/s added to the dense network data, and its comparison to its noiseless counterpart and a sparse network inversion for  $V_r=2$  km/s. The recovery of the dense network with 1 cm/s noise added to its data is qualitatively similar the dense network recover without noise.

40 km and 20 km network spacing, we cannot resolve rise time as suggested by previous studies, for subshear cases (Figure 4.19), which has to be true at least for multi-time window parameter although further investigation is needed to verify this for nonlinear parameterization. Rise-time resolvability is related to networks with distance of closest station from the fault similar to network spacing and is unchanged by shifting a coarser network such that its closest station to fault is closer than its network spacing (Figure 4.24). For a Gaussian additive uncorrelated noise level of 1 cm/s uniform over the entire domain, the rise-time resolvability of the dense network with noise is as good as its noiseless inversion and the qualitative comparisons to its noiseless sparse network still hold in different regimes of rupture velocity.

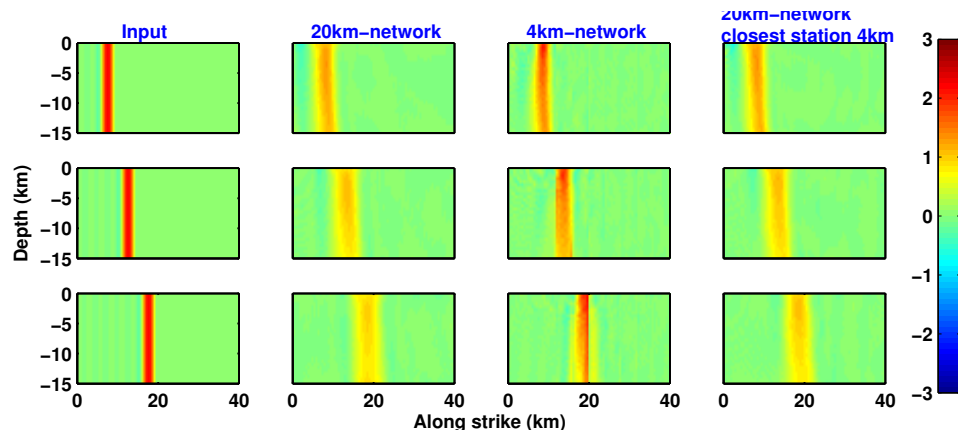


Figure 4.24: Slip rate snapshots from inversion for  $V_r = 2$  km/s and  $T_r = 1$  sec. Instead of having the network spacing as the closest distance from the fault, 20km-network is adjusted such that the closest stations are at a distance 4 km from the fault. Network spacing is the determining factor for the quality of inversion, but not the distance of the closest station to the fault.

## Chapter 5

# Conclusions

Source imaging is presented in two different settings: one where the velocity model is homogeneous/layered (Chapter 4) and other where the velocity model included lateral heterogeneity (Chapter 3). In each case a new method is presented to minimize the misfit between data and synthetics based on adjoint principles. Adjoint methods enabled data fitting using only the gradient information which proved to be very important to handle the vast amount of data and large number of free parameters. Going from data space to model space requires a matrix vector multiplication when the Green's functions (GFs) are known (homogeneous velocity model, where the matrix is the transpose of the GF matrix) while it requires solving a terminal value problem with time-reversed residuals as point forces at the locations where data is available when the Green's function matrix computation is too expensive (heterogeneous velocity model). The terminal value problem is solved using a 3D wave propagation code, SPECFEM3D. Using gradient information together with a conjugate-gradient algorithm, the cost function is minimized to arrive at a model that can explain the data well.

In homogenous velocity models, inversions are computationally inexpensive once a database of GFs is computed. So, a rigorous quantitative study of the capability to resolve fine properties of the rupture, such as rise time, is presented for homogenous velocity models. For heterogeneous velocity models, however, it is shown that the inversion is qualitatively similar to that of the homogenous velocity model, when the velocity model is known completely. For the heterogeneity that is found to be

representative of Earth's crust, not knowing the perturbations in velocity model gave counter-intuitive results. Two end-member heterogeneities (model B, model C) are found for which source inversion yields a source model that is as good as what would have been obtained if the complete 3D velocity model is considered in the inversion. So, in principle, all the results presented in Chapter 4 for the homogenous velocity model are still valid for the heterogeneous velocity model, if the velocity model is known well. When the velocity model is not perfectly known, the results of Chapter 4 are still valid as long as the uncertainty is no more than that of model B or C, as presented in Chapter 3. The combined results of Chapter 4 and 3 are useful in comprehending source inversion for velocity models with large uncertainty.

Inversion for complex sources can be well understood from the results of Chapter 4 itself. Slow ruptures will have trouble resolving rise times shorter than 4 sec with the best available ground motion earthquake recording systems as they have a spacing of the order of few tens of km. A new generation of earthquake recording systems with spacing less than a km will be required to obtain reliable estimates of the shorter rise times. Short rise times can only be trusted for fast ruptures. Care should be taken in interpreting the source models obtained by inversion modelers so far as almost all of them had stations that are few tens of km apart, especially when linear parametrization is used considering only the strong motion data.

## Chapter 6

# Recommendations for further research

### 6.1 Complex kinematic scenarios

Physics-based models of earthquakes show complex features in their source [*Gabriel et al.*, 2012] that may be resolved only using dense datasets. Identifying multi-pulse vs. single-pulse ruptures, especially on smaller scales, would put severe constraints on rupture models. A small domain having 60 km x 60 km station coverage is used to show that even if the dense data comes at the expense of noise that is higher than that of the coarse data, the inversion based on the dense dataset can still prove advantageous in getting a better idea of the peak slip velocity as well as pulse width and rupture complexity. Throughout these scenarios dense network refers to a station spacing of 1 km while coarse denotes stations 20 km apart from each other. A Gaussian additive uncorrelated noise of 1 cm/s is added to the dense data in all the scenarios considered in this section but the coarse data is not contaminated with any noise.

#### 6.1.1 Double pulse

Until now, only one pulse was prescribed on the fault plane and the inversion was performed from data of various networks. The next question that arises is what happens when there are multiple pulses. The simplest of the multiple pulse scenarios

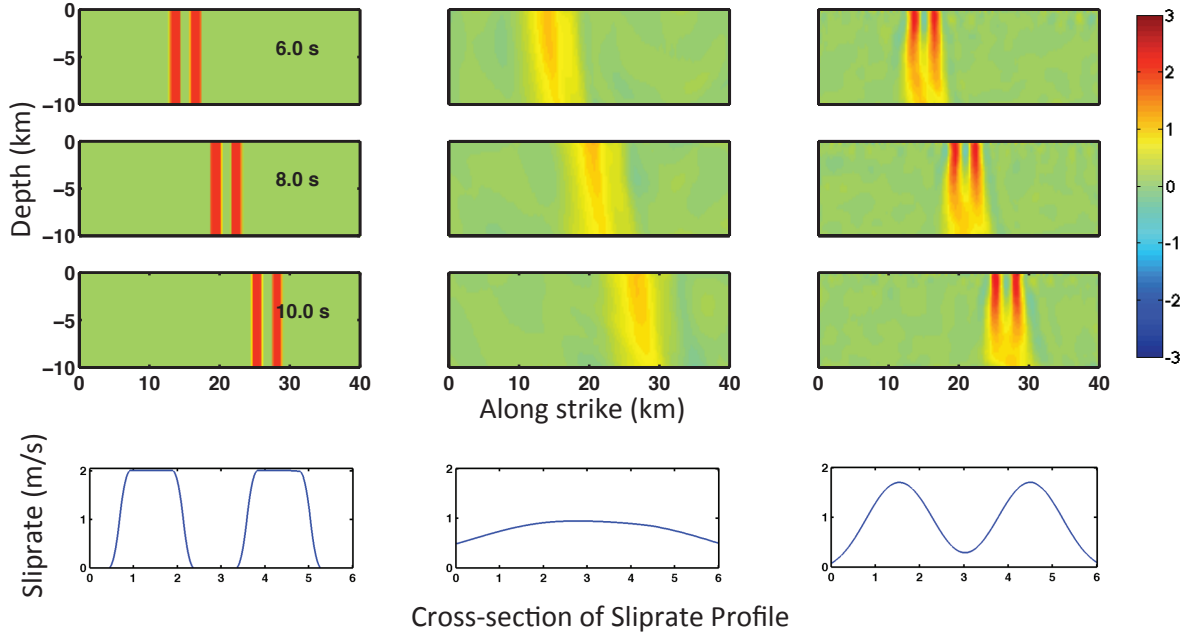


Figure 6.1: Top panel shows the input double pulse scenario (first column) and inversions for it based on data from the coarse network (second column) and data from the dense network (third column) at three different times. Bottom panel shows depth averaged profiles of the amplitude of slip velocity along strike for each of these cases. Only inversion from the dense network shows two pulses clearly. Pulse width is 1.5 km and the gap between pulses is also 1.5 km.

is a double pulse. Each pulse has its own three parameters: pulse width, rupture velocity and amplitude of slip rate. In addition to the parameters of the pulse, there is another parameter that needs to be prescribed viz. the gap between the pulses. A rigorous study of double pulse is not our goal here. So, we simply prescribe the scenario such that both pulses have same rupture velocity, slip-rate amplitude and pulse width. Also, the gap between the pulses is kept the same as the pulse width. When inversions are done with a pulse width of 1.5 km, we find that the inversion from the coarse network shows only one pulse in the recovered model while the dense network clearly shows both pulses in its recovered model (Figure 6.1). However, when the pulse width is increased to 3 km, both coarse and dense networks show clearly two pulses in the inverted source model (Figure 6.2). Nevertheless, the peak slip velocity is well resolved along with the shape of pulses only in the inversion based on dense network data.

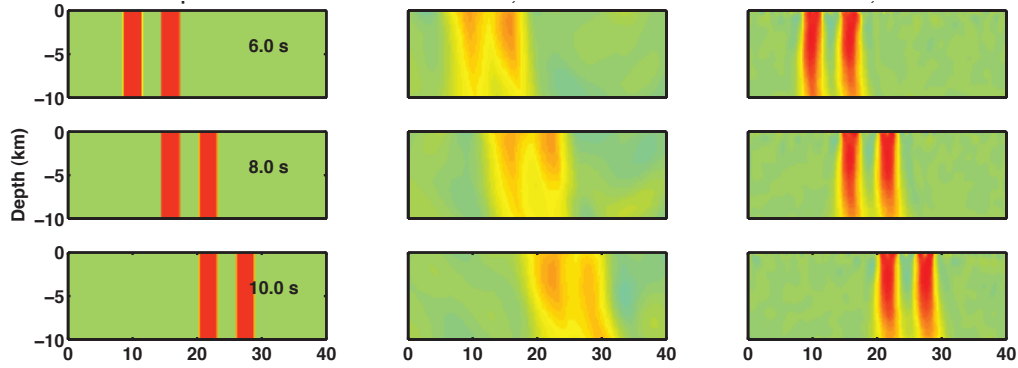


Figure 6.2: The three columns show the input, inversion with the coarse network and inversion with the dense network, respectively. Pulse width and the gap between them are both 3 km. Inversion from the data of coarse network also shows signs of two pulses for 3 km gap between pulses which was not the case when the gap was 1.5 km (Figure 6.1).

### 6.1.2 Back-propagating asperity

This scenario is motivated by an eye witness of the 2010 El Mayor - Cucapah earthquake where a portion of the fault was observed to be propagating in a direction opposite to the propagation direction of the rest of the fault. A kinematic Haskell pulse is prescribed such that it propagates at a uniform rupture speed from left to right except that a semi-circular asperity in the center of the fault close to the free surface remains locked until the rupture reaches the other end of the asperity. As the rupture moves away from the asperity, the semi-circular region starts to rupture from right to left with a peak slip velocity that is 1.5 times larger than the main pulse. An inversion with the dense network does show the difference in amplitudes of pulses while the inversion with the coarse network cannot distinguish the peak slip velocity in each pulse (Figure 6.3).

### 6.1.3 Apparent supershear

Inversions to date can identify if the rupture occurred at a speed that is faster than shear-wave speed but they cannot determine if the rupture jumped ahead of itself having an overall supershear speed. So, we prescribe a kinematic Haskell pulse that propagates at sub-Rayleigh speed but keeps jumping 1.5 km after propagating every

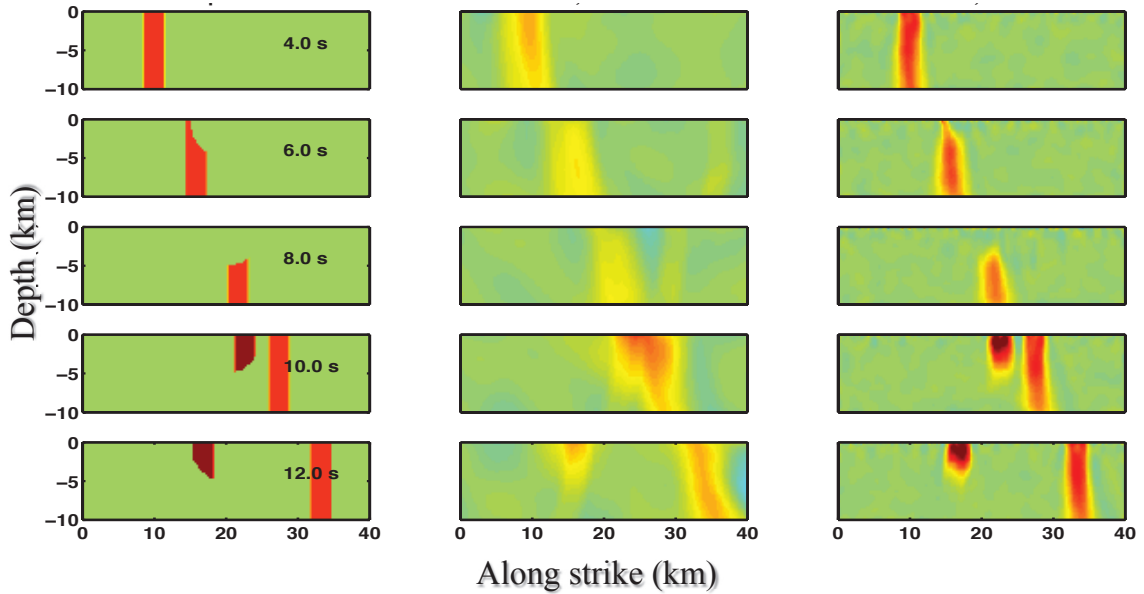


Figure 6.3: The three columns show rupture process of the input, inversion from the coarse network data and inversion from the dense network data, respectively, at five different times. A semi-circular asperity in the top center of the fault ruptures backward with higher slip velocity. Only the inversion from dense dataset can identify the amplitude difference in the back-propagating pulse.

7.5 km. The ratio of the length of the fault to the time taken by the rupture to reach the far end of the fault, gives an overall rupture speed of 4.5 km/s. The inversion carried out with data from the coarse network shows a pulse propagating uniformly at supershear speed but the inversion from data of the dense network can identify vividly the jumping of each sub-Rayleigh pulse (Figure 6.4).

## 6.2 Dynamic shear rupture

Most of the previous earthquake scenarios are based on kinematic sources where a rupture history was prescribed. In contrast, dynamic source modeling adopts fault constitutive laws and assumes initial conditions, then solves for a spontaneous dynamic rupture process. A more realistic earthquake scenario based on dynamic rupture modeling is considered here. The inversion of data from the subshear event shows a more clear delineation of the rupture front (Figure 6.5) for the dense network of

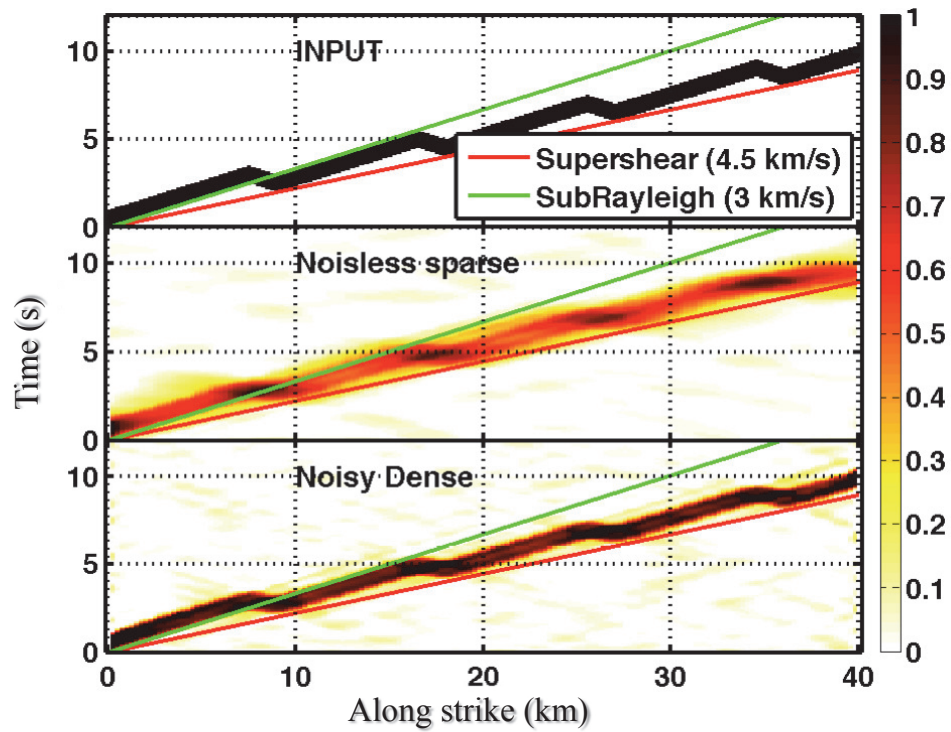


Figure 6.4: The three rows show the rupture process in space-time plots for the input, inversion from the coarse network data and inversion from the dense network data, respectively. The changes in speeds of individual pulses at regular intervals along strike is more evident in the dense dataset inversion.

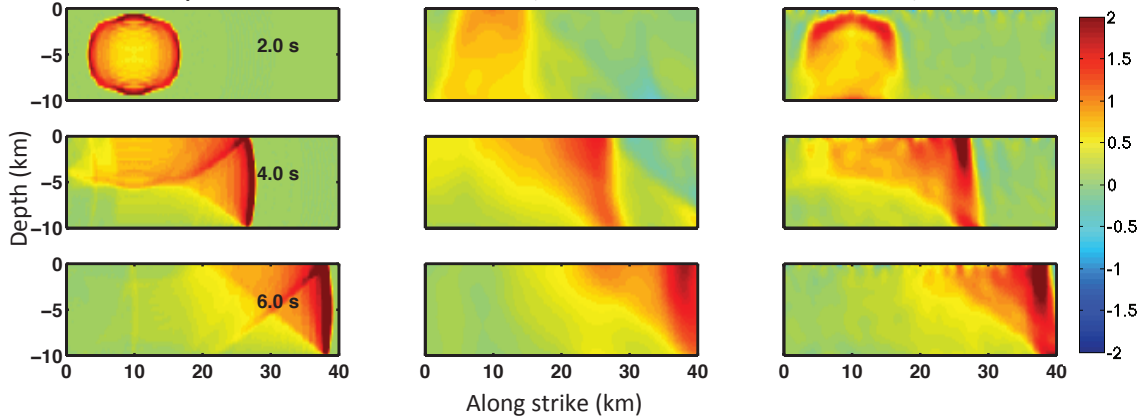


Figure 6.5: A spontaneously propagating dynamic shear rupture shown at three different times (left). Inversion from the coarse dataset is shown in the middle column and inversion from the dense dataset is shown in the right column.

sensors rather than the coarse network.

### 6.3 Trade-off between station spacing and noise

The dense network of stations is found to yield data that is robust to noise but a thorough quantification of the trade-off between network density and noise levels is required. The kinematic double pulse scenario is used to establish a preliminary understanding of this trade-off. Three different network spacings (1 km, 10 km and 20 km) are considered with three different noise levels (0 cm/s or noiseless, 3 cm/s and 10 cm/s). For the  $M_w$  7.0 scenario used here, 10 cm/s noise corresponds to a maximum signal to noise ratio (SNR) of 10:1. The inversion of dense data even for SNR 10:1 is equivalent to that of its noiseless inversion (Figure 6.6) indicating that the noisy dense inversion has extracted all the information from the data, and any other source properties that are not retrieved are due to the intrinsic limitations of the inverse problem.

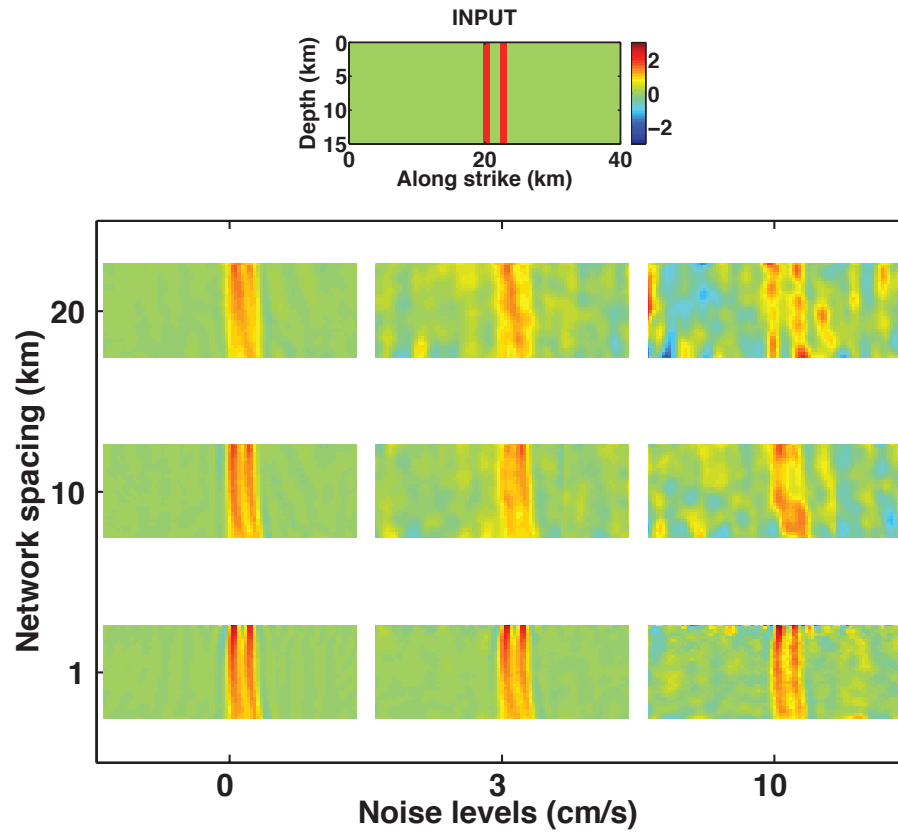


Figure 6.6: Inversions of a finely tuned double pulse scenario demonstrating that there is a certain pulse width and a certain gap below which the coarse dataset cannot predict that there are two pulses in the input while the dense dataset can show signs of two pulses even when the noise added to it has a signal to noise ratio of 10:1.

## 6.4 ShakeOut scenario

A great earthquake is overdue on the San Andreas fault that has been raising significant concern in Southern California. One of the main sources of information to construct scenarios of future earthquakes and to enhance our understanding of earthquake physics are images of the source processes of recent earthquakes inferred from seismological data. We need massively parallel computations to solve this inverse problem for densely recorded scenarios of large earthquakes on a California-sized scale.

To determine an optimal design for the space telescope (Section 1.7) and its advantages over traditional networks, a rigorous study of inferred parameters of realistic earthquake sources is required for different noise levels and network densities. Two main aspects need to be investigated. First, to reduce the noise in the data, the telescope diameter needs to be larger but that is more expensive and, at some point, not cost effective. Hence an optimal/acceptable diameter needs to be determined. Second, to compare telescope designs and traditional networks, the trade-off between spatial coverage and data error needs to be investigated. As the data get denser and denser, the associated inverse problems become computationally very challenging, hence the need for new inversion algorithms like the one developed in Chapter 2.

The real advantage of dense data can only be demonstrated and understood in the context of wave propagation in 3D heterogeneous medium. Crustal heterogeneities, especially shallow soft layers, control the mesh size and hence the computational cost of wave propagation simulations. For a seismic velocity model with shallow velocity layers having shear-wave speeds of 600 m/s (Figure 6.7), in order to properly resolve 1 Hz waves we need a mesh size of order 250 m, at least 10 times smaller than those used so far in our numerical experiments. An  $N$ -fold reduction in mesh element size leads to an  $N^4$  increase of computational cost, hence we are facing the challenge of a 10000-fold increase in computational cost. Such large-scale computations are only practically possible within reasonable time on state-of-the-art computing facilities like those available at National laboratories.

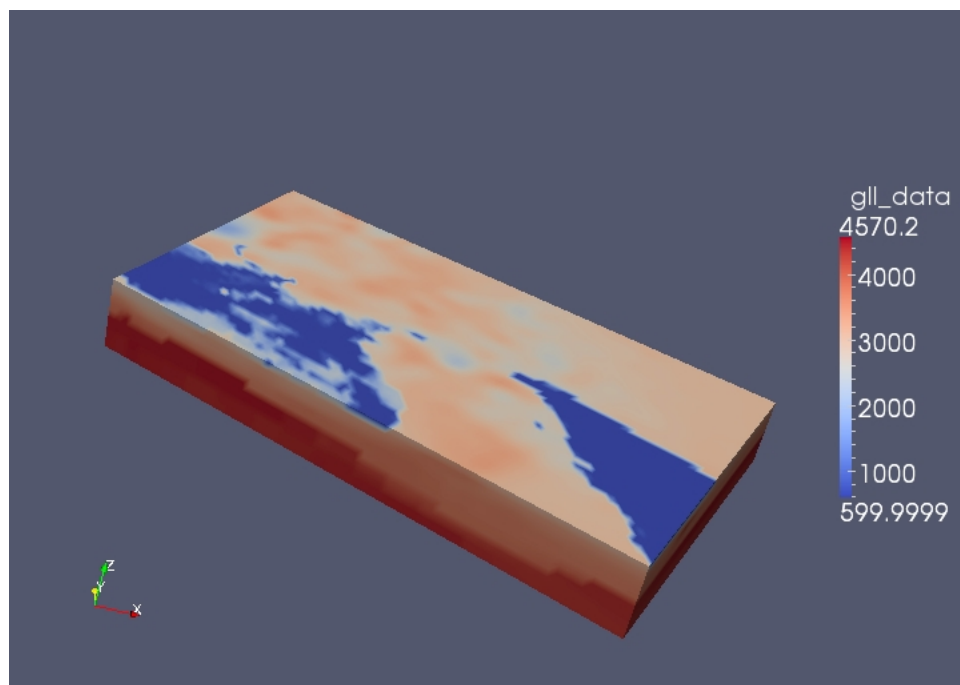


Figure 6.7: Domain for ShakeOut scenario showing shear-wave velocity ( $V_s$ ). The shallowest layers have a velocity of 600 m/s.

With the computational power feasible on the in-house supercomputing facility (FRAM) in the GPS division of Caltech, the source inversion of ShakeOut scenario is carried out by filtering data up to 5 sec period. Separate inversions were performed—one using the synthetic data from permanently deployed stations of Southern California Seismic Network (SCSN) and other using stations that are spaced 5 km apart. GSI would provide recording at much finer spacing but since the data is filtered at 0.2 Hz, much finer spacing would not add any additional information. These inversions show that there is no drastic gain with dense station spacing (Figure 6.8). One needs to push the filter cut off frequency to at least 0.5 Hz (would take several months on FRAM), if not 1 Hz, to see the real advantage of data from the space seismometer.

## 6.5 Tohoku-Oki earthquake

The source inversion code that is developed can be used to infer the evolution of slip for the  $M_w$  9.0 11th March, 2011 Tohoku-Oki earthquake with the strong motion data

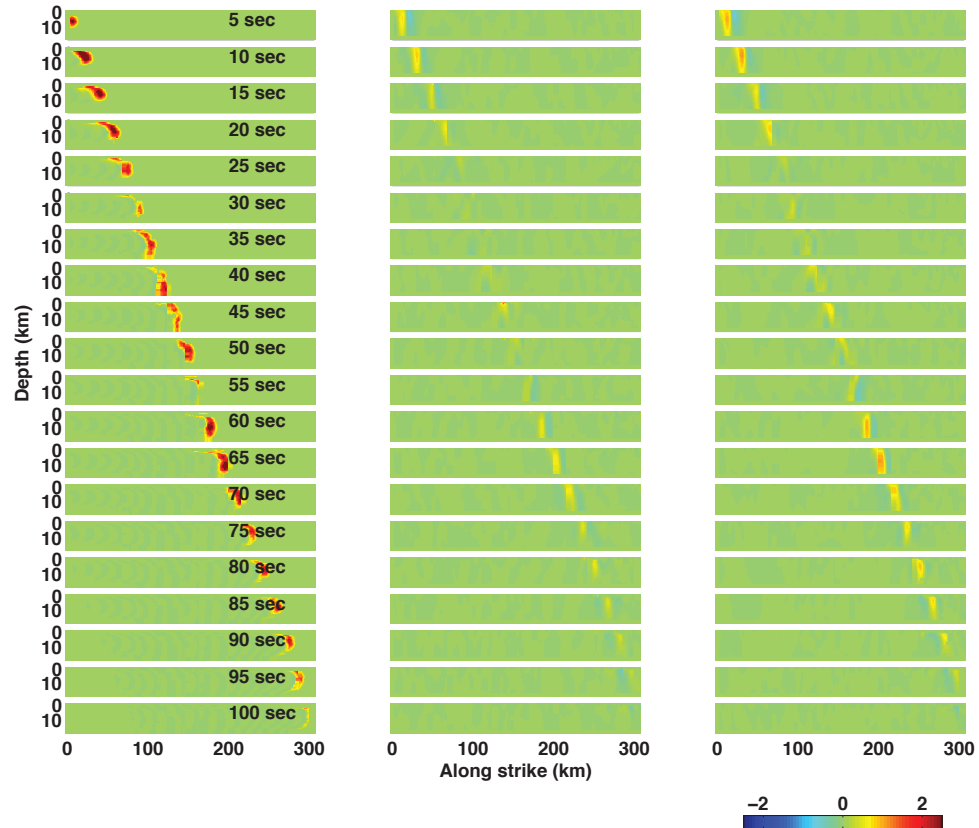


Figure 6.8: Source inversion of the ShakeOut scenario using data from the SCSN network (middle) and the data that would be provided by GSI (right). The input slip rate is shown at several time steps in left column. Data is low-pass filtered at 0.2 Hz before inversion. The 3D velocity model (SCEC CVM-H) of Southern California, with shallow layers having 600 m/s shear wave velocity, was used in the forward modeling as well as in the inversion.

from the best available ground network that is in Japan. Rupture models reported for this giant earthquake to date only considered data from a few stations along the coast. Most of the slip is concentrated in the up-dip regions for the inverted models, where the velocity strengthening region is thought to be present. It is possible to get a better understanding of slip complexity by considering strong motion data recorded by all the K-NET and KiK-net stations together with the continuous GPS stations. Moreover, most of the authors only considered layered velocity models while performing source inversion but details of ground motion can be significantly sensitive to lateral heterogeneities. Using the inversion that is developed as part of this thesis, the most realistic 3D velocity model of Japan can be used to address the rupture process of the Tohoku earthquake.

Subduction earthquakes have a branch fault that splays off from the megathrust fault reaching the seafloor at angles steeper than the megathrust. This kind of branch faults are known as megasplays and have implications for tsunami generation as there will be higher seafloor uplift if rupture branches to the megasplay. The virtue of the methodology developed in Chapter 2 is that it is general enough to incorporate multiple faults (both megathrust and megasplay) together with topography and bathymetry. Another advantage of our formulation is that it can handle the curvature of faults. The traditional way of modeling curved faults can at best model them as several planar sub-faults that give an overall non-planar shape but it is known that curvature is not handled properly in these formulations. A hexahedral mesh for the Tohoku earthquake is shown in Figure 6.9 that can be readily used in the inversion. The spectral element code used in all the works presented here has the limitation of using only hexahedral mesh elements which are not convenient enough for modeling sharp dip angles. Adjoint capabilities need to be incorporated in a finite-element code that can handle tetrahedral elements to perform a radically different inversion from those available for this earthquake in the literature.

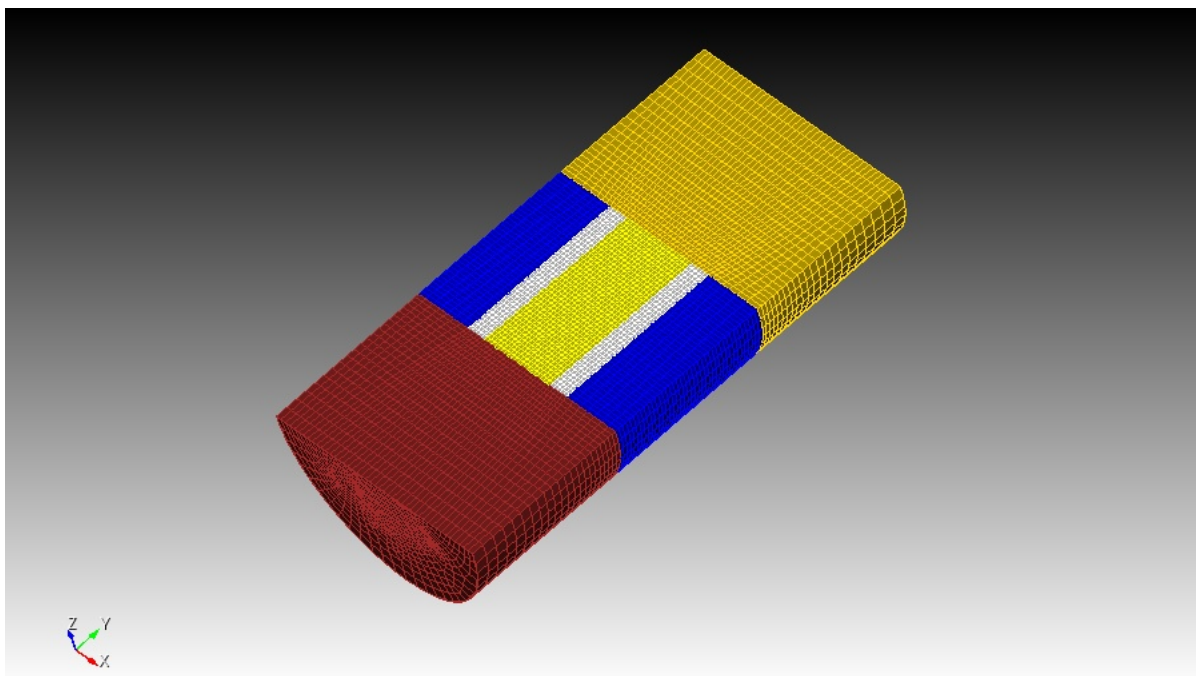


Figure 6.9: Meshed domain for the Tohoku earthquake. The central region is meshed by 5 km elements with buffer zones surrounding it that progressively coarsen outward.

## 6.6 Community Seismic Network

An emergent strategy to build extremely dense seismic networks involves low-cost micro-electromechanical system (MEMS) sensors and citizen seismologists. The Community Seismic Network (CSN) aims at deploying sensors on a block-by-block basis in southern California. An assessment can be made as to how CSN recordings could complement the Southern California Seismic Network (SCSN) to improve our understanding of earthquake physics, using the formulation presented in Chapter 2. Figure 6.10 shows a hexahedral mesh for the Sierra Madre fault system incorporating the non-planar nature of the fault. A  $M_w$  7.0 earthquake scenario can be simulated on the Sierra Madre fault system (Figure 6.10), which is within the urban area potentially covered by the CSN. Including the 3D velocity model of southern California (SCEC CVM-H), source inversions can be conducted based on the ground motions that would be recorded by the CSN and/or the SCSN. Due to the large number of stations and the complexity of the wave propagation medium, the source inversion

is computationally challenging. The Lagrangian formulation (Chapter 2) can be applied to invert for the source based on adjoint principles. The density of the CSN might resolve the details of the rupture process (e.g., position of asperities, peak slip velocity) significantly better than the SCSN.

## 6.7 Summary

We aim at understanding how well we can resolve the details of earthquake rupture from dense recordings. Dense data could enable source inversions with minimal or no assumptions, allowing the data to dictate how the rupture evolved. This can revolutionize our understanding of earthquake sources. Physics-based models of earthquakes show complex features that may be resolved only using dense datasets. We have investigated several such scenarios to determine what can be learned with dense measurements. The scenarios addressed open questions in earthquake dynamics and were also inspired by dynamic rupture simulations and laboratory observations. They included complexities such as multiple rupture fronts, apparent intersonic fronts and back-propagating fronts. Because current source inversion codes cannot handle the vast amounts of data that could be provided by the dense networks, we developed a new source inversion code based on adjoint methods. Equipped with this new tool, we have been assessing the effects of spatial, temporal and ground motion resolution on the quality of earthquake source imaging. These parameters trade off with the cost and feasibility of the GSI mission. The systematic studies have already provided elements for the GSI telescope design and for the scientific basis to justify a GSI space mission.

The methods and analysis developed in this thesis have broader applications beyond the GSI proof of concept. Our results contribute in general to the design of the next-generation of earthquake observation systems. For instance, the Community Seismic Network based on low-cost accelerometers aims at achieving dense spatial sampling in urban areas. Our source inversion approach can be applied to the recent Tohoku earthquake, which was recorded by the densest seismic and geodetic network

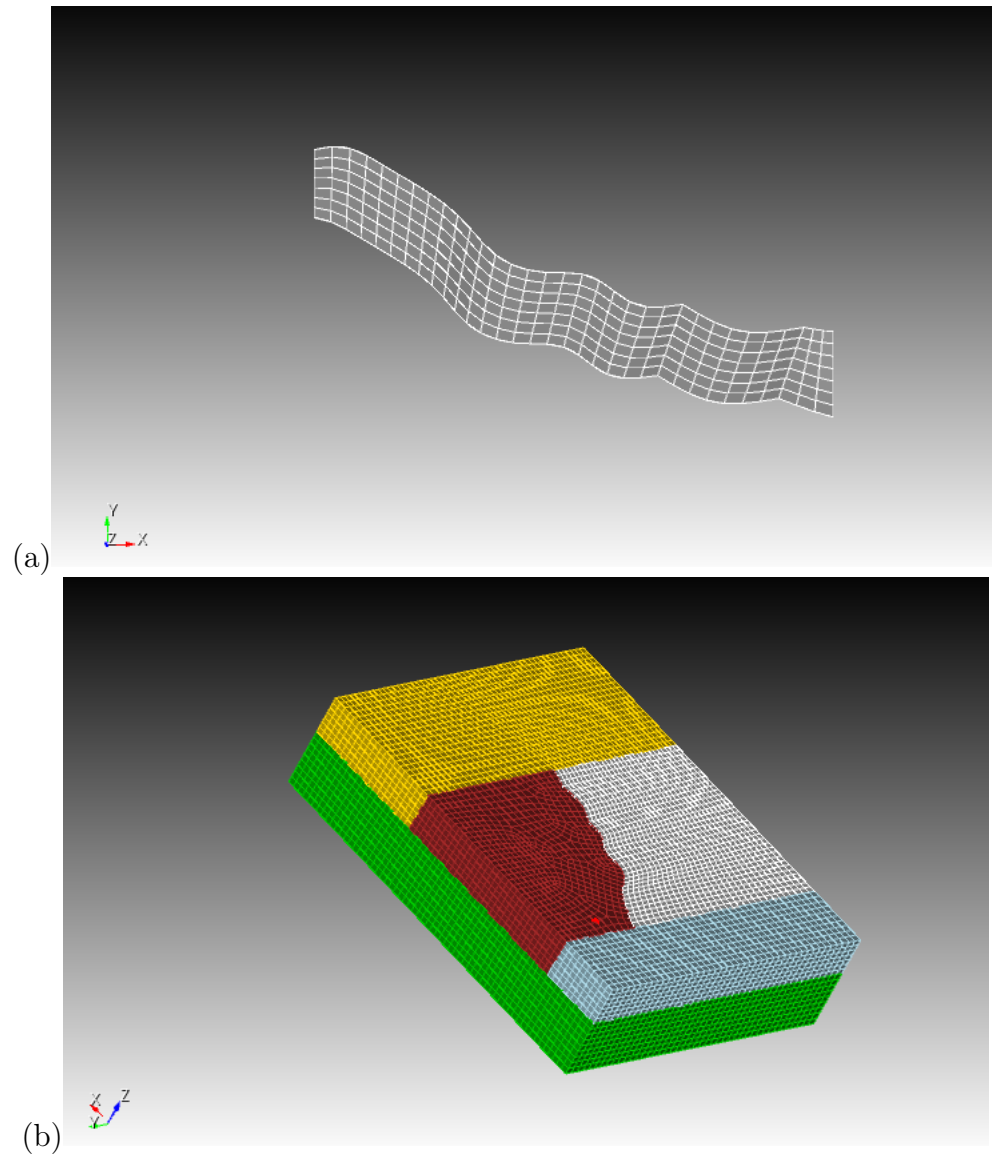


Figure 6.10: (a) Non-planar fault geometry of the Sierra Madre fault from the SCEC Community Fault Model (CFM). (b) A domain is constructed to encompass the fault and is meshed with hexahedral elements.

and yet the complete dataset has not been exploited.

Inversions for source models have so far used only data from few tens of stations. However, there are earthquakes which are recorded by thousands of stations (e.g., Tohoku-Oki etc.). Low-cost MEMS-based sensors as well as apps in smartphones, are leading to data explosion also known as 'Big Data', even with regard to ground shaking. A way of incorporating all this immense data in source inversion is demonstrated here for the first time in inverse problems with sensors of the order of tens of thousands and free parameters of the order of millions, using a scalable code that can run on exoscale computing facilities.

# Appendix A

## Software development (SPECFEM3D)

### A.1 Parallelization and scalability of fault solver in SPECFEM3D

In dynamic rupture simulations the computational mesh needs to be dense enough to resolve the breakdown zone at the rupture front, whose size is controlled by the rupture speed, frictional strength drop and slip-weakening distance [Day *et al.*, 2005]. The simulation of large earthquakes typically requires a node spacing less than a few hundred meter [Harris *et al.*, 2009]. For a total domain size of a few hundred km, the total number of spectral elements (e.g., with NGLL=5) needed is of the order of tens of millions. The elements carrying the fault interface need to be treated differently than the rest of the bulk, in order to satisfy the contact and friction conditions. One approach is to assign during domain decomposition all the spectral elements that are in contact with fault surfaces to a single processor. We initially adopted this strategy (as did Kaneko *et al.* [2008]) for the simplicity of its implementation. However, for large simulations this approach leads to a major load imbalance, with a bottleneck waiting for the processor that contains the faults.

To achieve load balancing, we parallelized the fault solver as well. During domain decomposition, we assigned matching pairs of elements on both sides of the fault to the same processor, the one with lowest rank of the pair. This simplifies the im-

plementation and avoids solver communications across the fault. The fault normal vector ( $\mathbf{n}$ ) and the fault boundary matrix ( $\mathbf{B}$ ) were pre-assembled across MPI interfaces along the fault, and internal forces are globally assembled before passing them to the fault solver. Hence, no additional assembly operation (no additional inter-processor communication) is performed by the fault solver. This strategy is expected to generate a minimal impact on the overall cost of computations, which should remain dominated by the bulk wave propagation solver. The original SPECFEM3D code has been shown to have good scaling properties for wave propagation problems [Komatitsch *et al.*, 2010]. We demonstrate here that our implementation of fault dynamics does not affect its parallel scalability.

We illustrate the strong scaling of the code in the community-based SCEC dynamic rupture benchmark TPV5. The problem comprises a fault 30 km long and 15 km deep. We placed absorbing boundaries 15 km away along strike from the fault tips, 25 km below the bottom edge of the fault and 30 km away in the fault normal direction. We adopted a spectral element size of 400 m with 5 GLL nodes per element edge, corresponding to the maximum recommended average grid size of 100 m [Harris *et al.*, 2009]. This resulted in 2,265,000 spectral elements. We ran the simulation at the Swiss National Supercomputing Center (CSCS) on Monte Rosa, a Cray XE6 system with 1496 compute nodes consisting of two 16-core AMD Opteron 6272 2.1 GHz CPUs and 32 GB of memory, and with high-performance networking through a Gemini 3D torus interconnect. The theoretical peak performance of Rosa is 402 Tflops. We choose numbers of processors in powers of 2 ranging from 64 to 8192. We suppressed intermediate outputs, as our focus was on verifying the scaling of the combined bulk-fault solver. The blue curve in Figure A.1 shows the total wall clock time taken by the solver (bulk and fault) to complete one TPV5 simulation. The code scales well within the range of number of processors we tested.

We also tested the scaling of the original SPECFEM3D code without fault implementation. For this purpose, we considered the same domain size and element size as that of our TPV5 simulations, but without the split-node fault surface, and we prescribed an explosion point source at the center of the domain. We repeated

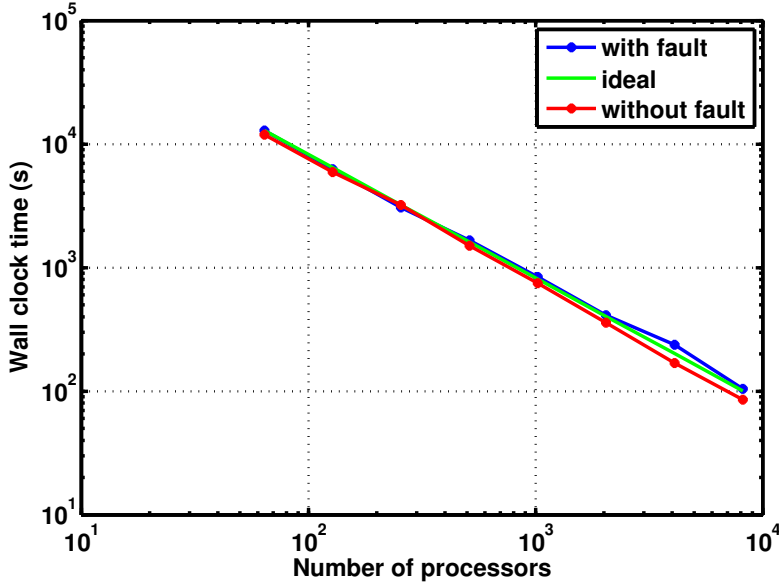


Figure A.1: Results of strong scalability of SPEC FEM3D with and without our fault implementation on CSCS’ Cray XE6 system (Rosa), up to 8192 processors. The tests are based on the SCEC TPV5 benchmark.

the scalability test in the same system and for the same set of processors as those previously used. The results, shown by the red curve in Figure A.1, demonstrate that the fault solver does not cause any significant load imbalance and does not affect the overall performance of the code.

While TPV5 was used to analyze strong scaling, we use a different version of the same benchmark, TPV205, for weak scaling. Essentially, a TPV5 (100 m grid size) run on 256 processors is compared with the same benchmark problem solved with 200 m grid size on 16 processors and 50 m grid size on 4096 processors. These three sets of simulations have, in principle, the same load per processor: the total number of operations for fixed domain size and duration scales inversely as fourth power of grid size. Figure A.2 shows the weak scalability results for SPEC FEM3D with our fault implementation. Wall clock time is normalized with respect to that of the 50 m grid size simulation. The weak scalability is overall satisfactory. The minor ( $< 2\%$ ) deviation in weak scaling could be attributed to the fact that the number of spectral elements are not exactly 4 times those at lower resolution on the fault plane, as the dimensions of fault are fixed.

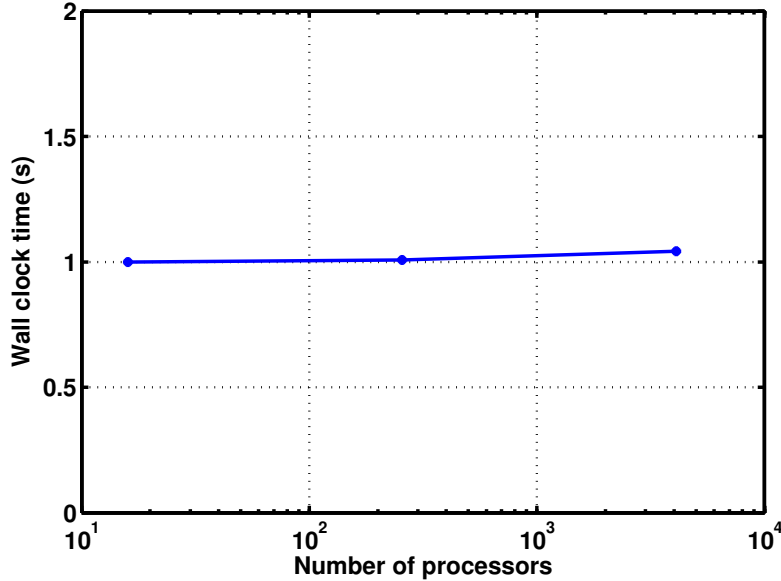


Figure A.2: Results of weak scalability of SPECFEM3D with our fault implementation on CSCS’ Cray XE6 system (Rosa). The tests are based on the TPV205 benchmark with 50, 100 and 200 m average grid spacing.

## A.2 Convergence analysis of SPECFEM3D for dynamic rupture

To assess our implementation of the dynamic rupture boundary conditions into the SPECFEM3D, we solve 3-D problems of spontaneous rupture propagation for planar and branched faults embedded in a uniform elastic isotropic half-space, in which the fault rupture reaches the Earth’s surface. The test problems correspond to the SCEC dynamic rupture code validation exercise [Harris *et al.*, 2009]. We assess the efficiency of the numerical model by estimating the convergence rate to a common solution by increasing the numerical resolution. For that purpose we use a planar fault corresponding to the TPV205 SCEC benchmark problem.

Assessing the accuracy of the numerical methods for spontaneous dynamic rupture simulations is challenging, as we lack appropriate analytical solutions for comparison. Determining the power-law convergence rates with respect to grid spacing is a good indicator of the efficiency of the numerical method to reach to a common solution

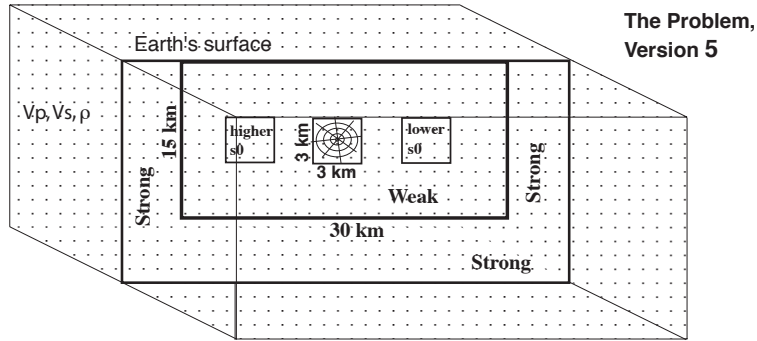


Figure A.3: Results of weak scalability of SPECFEM3D with our fault implementation on CSCS' Cray XE6 system (Rosa). The tests are based on the TPV205 benchmark with 50, 100 and 200 m average grid spacing. ([http://scecddata.usc.edu/cvws/benchmark\\_descriptions.html](http://scecddata.usc.edu/cvws/benchmark_descriptions.html)).

(e.g., *Day et al.*, 2005 *Dalguer and Day*, 2006). For this purpose we follow *Day et al.* [2005] and calculate three global error metrics (rupture time, final slip, and peak slip rate) for each numerical solution with grid sizes of 100 and 200 m using the highest-resolution solution (50 m) as reference solution. The error metrics are calculated by estimating the RMS differences of the quantities relative to the reference solution. The formulation and parameters of the numerical example correspond to the SCEC TPV205 benchmark problem. The problem geometry is shown in Figure A.3.

RMS quantities of final slip and peak slip rate are shown Figure A.4. All three of these quantities have power-law decay showing convergence of the solution. Unlike *Day et al.* [2005], the solid line does not seem to intersect dashed line in RMS of rupture time contours. This is because of no proper way of computing RMS error in spectral element grid. Interpolation techniques, if used, have to be done in spectral element domain. Also, fault edges are handled differently in SEM and so are removed in interpolation and RMS computation.

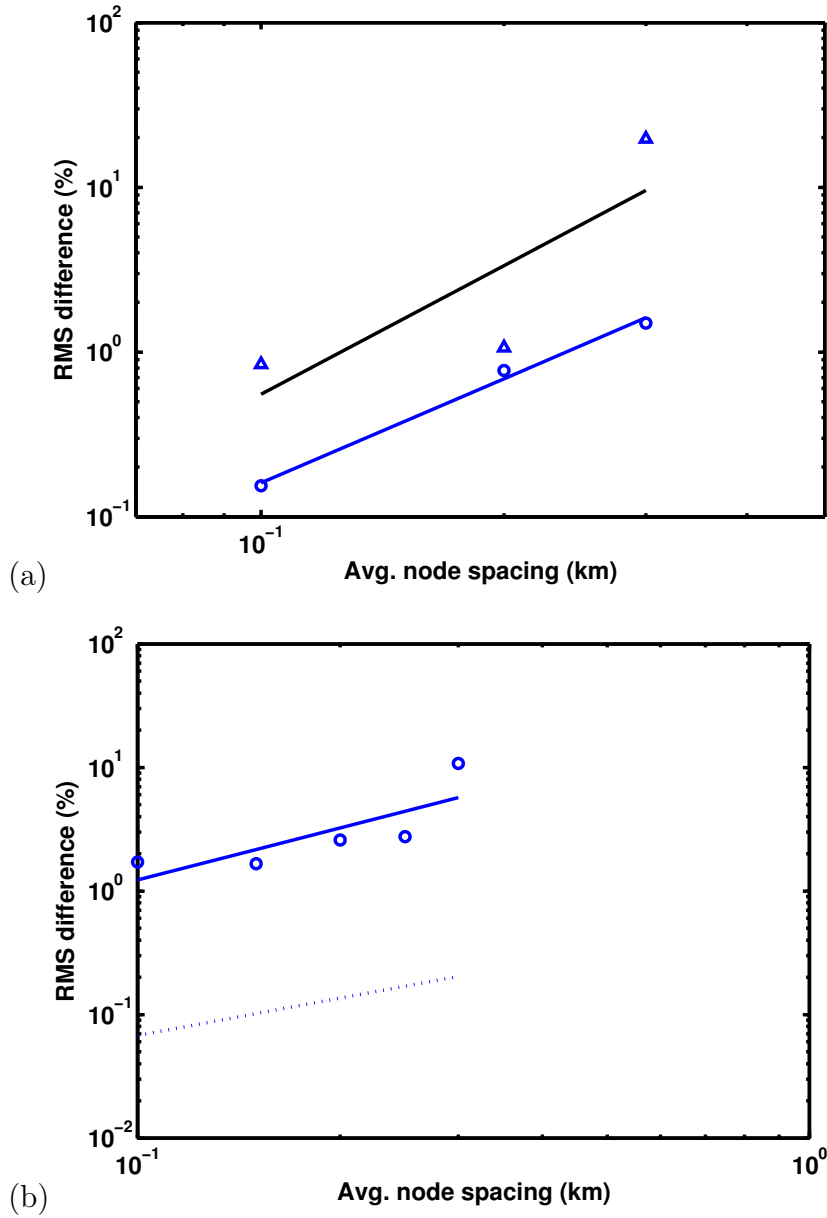


Figure A.4: (a) RMS misfits final slip (blue) and peak slip rate (black) as a function of grid size (b) RMS misfits rupture time as a function of grid size. Dotted line shows timestep.

# Bibliography

- Aagaard, B. T., and T. H. Heaton (2004), Near-source ground motions from simulations of sustained intersonic and supersonic fault ruptures, *Bulletin of the Seismological Society of America*, *94*(6), 2064–2078.
- Akcelik, V., G. Biros, O. Ghattas, J. Hill, D. Keyes, and B. van Bloemen Waanders (2006), Parallel algorithms for PDE-constrained optimization, *Parallel Processing for Scientific Computing*, p. 291–322.
- Aki, K., and P. G. Richards (2002), *Quantitative seismology*, Univ Science Books.
- Asano, K., and T. Iwata (2009), Source Rupture Process of the 2004 Chuetsu, Mid-Niigata Prefecture, Japan, Earthquake Inferred from Waveform Inversion with Dense Strong-Motion Data, *Bulletin of the Seismological Society of America*, *99*(1), 123–140, doi:10.1785/0120080257.
- Askan, A., and J. Bielak (2008), Full Anelastic Waveform Tomography Including Model Uncertainty, *Bulletin of the Seismological Society of America*, *98*(6), 2975–2989, doi:10.1785/0120080138.
- Beresnev, I. A. (2003), Uncertainties in Finite-Fault Slip Inversions: To What Extent to Believe? (A Critical Review), *Bulletin of the Seismological Society of America*, *93*(6), 2445–2458, doi:10.1785/0120020225.
- Beresnev, I. A., and G. M. Atkinson (2002), Source parameters of earthquakes in eastern and western North America based on finite-fault modeling, *Bulletin of the Seismological Society of America*, *92*(2), 695–710.

- Berman, D. H. (1997), Computing effective reflection coefficients in layered media, *The Journal of the Acoustical Society of America*, *101*(2), 741–748, doi:10.1121/1.418037.
- Bernard, P., and D. Baumont (2005), Shear Mach wave characterization for kinematic fault rupture models with constant supershear rupture velocity, *Geophysical Journal International*, *162*(2), 431–447.
- Bernard, P., J.-C. Gariel, and L. Dorbath (1997), Fault location and rupture kinematics of the magnitude 6.8, 1992 Erzincan earthquake, Turkey, from strong ground motion and regional records, *Bulletin of the Seismological Society of America*, *87*(5), 1230–1243.
- Beroza, G. C., and P. Spudich (1988), Linearized inversion for fault rupture behavior: application to the 1984 Morgan Hill, California, earthquake, *Journal of Geophysical Research: Solid Earth (1978–2012)*, *93*(B6), 6275–6296.
- Bizzarri, A., and P. Spudich (2008), Effects of supershear rupture speed on the high-frequency content of S waves investigated using spontaneous dynamic rupture models and isochrone theory, *Journal of Geophysical Research: Solid Earth*, *113*(B5), doi:10.1029/2007JB005146.
- Bizzarri, A., E. M. Dunham, and P. Spudich (2010), Coherence of Mach fronts during heterogeneous supershear earthquake rupture propagation: Simulations and comparison with observations, *Journal of Geophysical Research: Solid Earth*, *115*(B8), doi:10.1029/2009JB006819.
- Bouchon, M., M. N. Toksöz, H. Karabulut, M.-P. Bouin, M. Dietrich, M. Aktar, and M. Edie (2002), Space and time evolution of rupture and faulting during the 1999 Izmit (Turkey) earthquake, *Bulletin of the Seismological Society of America*, *92*(1), 256–266.
- Brodbeck, V., L. Spinelli, A. M. Lascano, M. Wissmeier, M.-I. Vargas, S. Vulliamoz, C. Pollo, K. Schaller, C. M. Michel, and M. Seeck (2011), Electroencephalographic

- source imaging: a prospective study of 152 operated epileptic patients, *Brain*, *134*(10), 2887–2897, doi:10.1093/brain/awr243, PMID: 21975586.
- Chen, Y. T., J. Y. Zhou, and J. C. Ni (1991), Inversion of near-source-broadband accelerograms for the earthquake source-time function, *Tectonophysics*, *197*(1), 89–98.
- Chi, W.-C., D. Dreger, and A. Kaverina (2001), Finite-source modeling of the 1999 Taiwan (Chi-Chi) earthquake derived from a dense strong-motion network, *Bulletin of the Seismological Society of America*, *91*(5), 1144–1157.
- Claerbout, J. F., and S. Fomel (2008), *Image estimation by example: geophysical soundings image construction: multidimensional autoregression*, Citeseer.
- Clayton, R. W., T. Heaton, M. Chandy, A. Krause, M. Kohler, J. Bunn, R. Guy, M. Olson, M. Faulkner, M. Cheng, L. Strand, R. Chandy, D. Obenshain, A. Liu, and M. Aivazis (2012), Community Seismic Network, *Annals of Geophysics*, *54*(6), doi:10.4401/ag-5269.
- Custódio, S., M. T. Page, and R. J. Archuleta (2009), Constraining earthquake source inversions with GPS data: 2. A two-step approach to combine seismic and geodetic data sets, *Journal of Geophysical Research: Solid Earth*, *114*(B1), doi: 10.1029/2008JB005746.
- Dalguer, L. A., and S. M. Day (2006), Comparison of fault representation methods in finite difference simulations of dynamic rupture, *Bulletin of the Seismological Society of America*, *96*(5), 1764–1778.
- Day, S. M., L. A. Dalguer, N. Lapusta, and Y. Liu (2005), Comparison of finite difference and boundary integral solutions to three-dimensional spontaneous rupture, *Journal of Geophysical Research: Solid Earth*, *110*(B12), doi: 10.1029/2005JB003813.
- Delouis, B., D. Giardini, P. Lundgren, and J. Salichon (2002), Joint inversion of InSAR, GPS, teleseismic, and strong-motion data for the spatial and temporal

- distribution of earthquake slip: Application to the 1999 Izmit mainshock, *Bulletin of the Seismological Society of America*, 92(1), 278–299.
- Fichtner, A., B. L. Kennett, H. Igel, and H.-P. Bunge (2010), Full waveform tomography for radially anisotropic structure: New insights into present and past states of the Australasian upper mantle, *Earth and Planetary Science Letters*, 290(3–4), 270–280, doi:10.1016/j.epsl.2009.12.003.
- Fletcher, R., and C. M. Reeves (1964), Function minimization by conjugate gradients, *The Computer Journal*, 7(2), 149–154.
- Frankel, A., and R. W. Clayton (1986), Finite difference simulations of seismic scattering: Implications for the propagation of short-period seismic waves in the crust and models of crustal heterogeneity, *Journal of Geophysical Research: Solid Earth*, 91(B6), 6465–6489, doi:10.1029/JB091iB06p06465.
- Fuchs, K., and G. Müller (1971), Computation of Synthetic Seismograms with the Reflectivity Method and Comparison with Observations, *Geophysical Journal of the Royal Astronomical Society*, 23(4), 417–433, doi:10.1111/j.1365-246X.1971.tb01834.x.
- Gabriel, A.-A., J.-P. Ampuero, L. A. Dalguer, and P. M. Mai (2012), The transition of dynamic rupture styles in elastic media under velocity-weakening friction, *Journal of Geophysical Research: Solid Earth*, 117(B9), n/a–n/a, doi:10.1029/2012JB009468.
- Graves, R. W., and D. J. Wald (2001), Resolution analysis of finite fault source inversion using one- and three-dimensional Green’s functions: 1. Strong motions, *Journal of Geophysical Research: Solid Earth*, 106(B5), 8745–8766, doi:10.1029/2000JB900436.
- Gülen, L., A. Pinar, D. Kalafat, N. Özel, G. Horasan, M. Yilmazer, and A. M. I\csikara (2002), Surface fault breaks, aftershock distribution, and rupture process

- of the 17 August 1999 Izmit, Turkey, earthquake, *Bulletin of the Seismological Society of America*, *92*(1), 230–244.
- Harris, R. A., M. Barall, R. Archuleta, E. Dunham, B. Aagaard, J. P. Ampuero, H. Bhat, V. Cruz-Atienza, L. Dalguer, P. Dawson, S. Day, B. Duan, G. Ely, Y. Kaneko, Y. Kase, N. Lapusta, Y. Liu, S. Ma, D. Oglesby, K. Olsen, A. Pitarka, S. Song, and E. Templeton (2009), The SCEC/USGS Dynamic Earthquake Rupture Code Verification Exercise, *Seismological Research Letters*, *80*(1), 119–126, doi:10.1785/gssrl.80.1.119.
- Hartzell, S., and C. Langer (1993), Importance of model parameterization in finite fault inversions: Application to the 1974 Mw 8.0 Peru Earthquake, *Journal of Geophysical Research: Solid Earth*, *98*(B12), 22,123–22,134, doi:10.1029/93JB02453.
- Hartzell, S., S. Harmsen, and A. Frankel (2010), Effects of 3D Random Correlated Velocity Perturbations on Predicted Ground Motions, *Bulletin of the Seismological Society of America*, *100*(4), 1415–1426, doi:10.1785/0120090060.
- Hartzell, S. H., and T. H. Heaton (1983), Inversion of strong ground motion and teleseismic waveform data for the fault rupture history of the 1979 Imperial Valley, California, earthquake, *Bulletin of the Seismological Society of America*, *73*(6A), 1553–1583.
- Heaton, T. H. (1990), Evidence for and implications of self-healing pulses of slip in earthquake rupture, *Physics of the Earth and Planetary Interiors*, *64*(1), 1–20, doi:10.1016/0031-9201(90)90002-F.
- Hernandez, B., N. M. Shapiro, S. K. Singh, J. F. Pacheco, F. Cotton, M. Campillo, A. Iglesias, V. Cruz, J. M. Gomez, and L. Alcantara (2001), Rupture history of September 30, 1999 intraplate earthquake of Oaxaca, Mexico ( $M$  (sub W) = 7.5) from inversion of strong-motion data, *Geophysical Research Letters*, *28*(2), 363–366, doi:http://dx.doi.org/10.1029/2000GL011975.

- Herrmann, R. B. (2001), Computer programs in seismology-An overview of Synthetic Seismogram Computation Version 3.1, *Department of Earth and Planetary Sciences, St Louis Univ.*
- Hestenes, M., and E. Stiefel (1952), Methods of Conjugate Gradients for Solving Linear Systems, *Journal of Research of the National Bureau of Standards*, 49(6), 409–436.
- Hjörleifsdóttir, V., M. Simons, J. Tromp, and California Institute of Technology. Division of Geological and Planetary Sciences (2007), Earthquake source characterization using 3D numerical modeling, Ph.D. thesis, California Institute of Technology, Pasadena, Calif.
- Huang, W.-G., J.-H. Wang, B.-S. Huang, K.-C. Chen, T.-M. Chang, R.-D. Hwang, H.-C. Chiu, and C.-C. P. Tsai (2001), Estimates of source parameters for the 1999 Chi-Chi, Taiwan, earthquake based on Brune’s source model, *Bulletin of the Seismological Society of America*, 91(5), 1190–1198.
- Huang, Y.-L., and B.-S. Huang (2004), Numerical Modeling for Earthquake Source Imaging: Implications for Array Design in Determining the Rupture Process, *Terrestrial, Atmospheric and Oceanic Sciences*, 15, 133–150.
- Ide, S. (2007), *Treatise on Geophysics, Volume 4-Earthquake Seismology*, 1st ed., Elsevier Science.
- Ide, S., G. C. Beroza, and J. J. McGuire (2005), Imaging earthquake source complexity, in *Geophysical Monograph Series*, vol. 157, edited by A. Levander and G. Nolet, pp. 117–135, American Geophysical Union, Washington, D. C.
- Iida, M. (1990), Optimum strong-motion array geometry for source inversion—II, *Earthquake Engineering & Structural Dynamics*, 19(1), 35–44, doi: 10.1002/eqe.4290190105.
- Ji, C., D. J. Wald, and D. V. Helmberger (2002), Source Description of the 1999 Hector Mine, California, Earthquake, Part I: Wavelet Domain Inversion Theory

- and Resolution Analysis, *Bulletin of the Seismological Society of America*, 92(4), 1192–1207, doi:10.1785/0120000916.
- Kaneko, Y., N. Lapusta, and J.-P. Ampuero (2008), Spectral element modeling of spontaneous earthquake rupture on rate and state faults: Effect of velocity-strengthening friction at shallow depths, *Journal of Geophysical Research*, 113(B9), doi:10.1029/2007JB005553.
- Kawakatsu, H., and J.-P. Montagner (2008), Time-reversal seismic-source imaging and moment-tensor inversion, *Geophysical Journal International*, 175(2), 686–688.
- Kim, Y., Q. Liu, and J. Tromp (2011), Adjoint centroid-moment tensor inversions, *Geophysical Journal International*, 186(1), 264–278.
- Komatitsch, D., G. Erlebacher, D. Göddeke, and D. Michéa (2010), High-order finite-element seismic wave propagation modeling with MPI on a large GPU cluster, *Journal of Computational Physics*, 229(20), 7692–7714, doi:10.1016/j.jcp.2010.06.024.
- Konca, A. O., Y. Kaneko, N. Lapusta, and J.-P. Avouac (2013), Kinematic inversion of physically plausible earthquake source models obtained from dynamic rupture simulations, *Journal of Geophysical Research*.
- Kremers, S., A. Fichtner, G. B. Brietzke, H. Igel, C. Larmat, L. Huang, and M. Käser (2011), Exploring the potentials and limitations of the time-reversal imaging of finite seismic sources, *Solid Earth*, 2(1), 95–105, doi:10.5194/se-2-95-2011.
- Lawson, C. L., and R. J. Hanson (1995), 23. Linear Least Squares with Linear Inequality Constraints, in *Solving Least Squares Problems*, pp. 158–173, Society for Industrial and Applied Mathematics.
- Lee, S.-J., K.-F. Ma, and H.-W. Chen (2006), Three-dimensional dense strong motion waveform inversion for the rupture process of the 1999 Chi-Chi, Taiwan, earthquake, *Journal of Geophysical Research: Solid Earth*, 111(B11), doi:10.1029/2005JB004097.

- Lee, S.-J., B.-S. Huang, M. Ando, H.-C. Chiu, and J.-H. Wang (2011), Evidence of large scale repeating slip during the 2011 Tohoku-Oki earthquake, *Geophysical Research Letters*, *38*(19), L19,306.
- Lee, W. H. K., T. C. Shin, K. W. Kuo, K. C. Chen, and C. F. Wu (2001), CWB free-field strong-motion data from the 21 September Chi-Chi, Taiwan, earthquake, *Bulletin of the Seismological Society of America*, *91*(5), 1370–1376.
- Li, X., V. F. Cormier, and M. N. Toksöz (2002), Complex source process of the 17 August 1999 Izmit, Turkey, earthquake, *Bulletin of the Seismological Society of America*, *92*(1), 267–277.
- Liu, P., and R. J. Archuleta (2004), A new nonlinear finite fault inversion with three-dimensional Green's functions: Application to the 1989 Loma Prieta, California, earthquake, *Journal of Geophysical Research: Solid Earth (1978–2012)*, *109*(B2).
- Liu, P., S. Custódio, and R. J. Archuleta (2006), Kinematic inversion of the 2004 M 6.0 Parkfield earthquake including an approximation to site effects, *Bulletin of the Seismological Society of America*, *96*(4B), S143–S158.
- Liu, Q., and J. Tromp (2006), Finite-Frequency Kernels Based on Adjoint Methods, *Bulletin of the Seismological Society of America*, *96*(6), 2383–2397, doi:10.1785/0120060041.
- Liu, Q., and J. Tromp (2008), Finite-frequency sensitivity kernels for global seismic wave propagation based upon adjoint methods, *Geophysical Journal International*, *174*(1), 265–286, doi:10.1111/j.1365-246X.2008.03798.x.
- Ma, K.-F., J. Mori, S.-J. Lee, and S. B. Yu (2001), Spatial and temporal distribution of slip for the 1999 Chi-Chi, Taiwan, earthquake, *Bulletin of the Seismological Society of America*, *91*(5), 1069–1087.
- Mai, P., J. Burjanek, B. Delouis, G. Festa, C. Francois-Holden, D. Monelli, T. Uchide, and J. Zahradnik (2007), Earthquake Source Inversion Blindtest: Initial Results and Further Developments, *AGU Fall Meeting Abstracts*, p. 08.

- Menke, W. (1989), *Geophysical Data Analysis: Discrete Inverse Theory*, Academic Press.
- Michel, R., J. Ampuero, J. Avouac, N. Lapusta, S. Leprince, D. Redding, and S. N. Somala (2013), A Geostationary Optical Seismometer, Proof of Concept, *IEEE Transactions on Geoscience and Remote Sensing*, *51*(1), 695–703, doi:10.1109/TGRS.2012.2201487.
- Miyatake, T., M. Iida, and K. Shimazaki (1986), The effect of strong-motion array configuration on source inversion, *Bulletin of the Seismological Society of America*, *76*(5), 1173–1185.
- Olson, A. H., and J. G. Anderson (1988), Implications of frequency-domain inversion of earthquake ground motions for resolving the space-time dependence of slip on an extended fault, *Geophysical Journal*, *94*(3), 443–455, doi:10.1111/j.1365-246X.1988.tb02267.x.
- Olson, A. H., and R. J. Apsel (1982), Finite faults and inverse theory with applications to the 1979 Imperial Valley earthquake, *Bulletin of the Seismological Society of America*, *72*(6A), 1969–2001.
- Page, M. T., S. Custódio, R. J. Archuleta, and J. M. Carlson (2009), Constraining earthquake source inversions with GPS data: 1. Resolution-based removal of artifacts, *Journal of Geophysical Research: Solid Earth*, *114*(B1), doi:10.1029/2007JB005449.
- Peyrat, S., K. B. Olsen, and R. Madariaga (2004), Which Dynamic Rupture Parameters Can Be Estimated from Strong Ground Motion and Geodetic Data?, in *Computational Earthquake Science Part II*, edited by A. Donnellan, P. Mora, M. Matsu'ura, and X.-c. Yin, PAGEOPH Topical Volumes, pp. 2155–2169, Birkhäuser Basel.
- Polak, E., and G. Ribière (1969), Note sur la convergence de directions conjuguées, *Rev. Française Informat, Recherche Opertionelle*, *3e année*, *16*, 35–43.

- Sambridge, M., and G. Drijkoningen (1992), Genetic algorithms in seismic waveform inversion, *Geophysical Journal International*, *109*(2), 323–342.
- Saraò, A., S. Das, and P. Suhadolc (1998), Effect of non-uniform station coverage on the inversion for earthquake rupture history for a Haskell-type source model, *Journal of Seismology*, *2*(1), 1–25, doi:10.1023/A:1009795916726.
- Sekiguchi, H., and T. Iwata (2002), Rupture process of the 1999 Kocaeli, Turkey, earthquake estimated from strong-motion waveforms, *Bulletin of the Seismological Society of America*, *92*(1), 300–311.
- Sen, M. K., and P. L. Stoffa (1991), Nonlinear one-dimensional seismic waveform inversion using simulated annealing, *Geophysics*, *56*(10), 1624–1638, doi: <http://dx.doi.org/10.1190/1.1442973>.
- Shao, G., and C. Ji (2012), What the exercise of the SPICE source inversion validation BlindTest 1 did not tell you, *Geophysical Journal International*, *189*(1), 569–590, doi:10.1111/j.1365-246X.2012.05359.x.
- Shao, G., C. Ji, and E. Hauksson (2012), Rupture process and energy budget of the 29 July 2008 M w 5.4 Chino Hills, California, earthquake, *Journal of Geophysical Research*, *117*(B7), doi:10.1029/2011JB008856.
- Tape, C., Q. Liu, A. Maggi, and J. Tromp (2009), Adjoint Tomography of the Southern California Crust, *Science*, *325*(5943), 988–992, doi:10.1126/science.1175298.
- Tape, C., Q. Liu, A. Maggi, and J. Tromp (2010), Seismic tomography of the southern California crust based on spectral-element and adjoint methods, *Geophysical Journal International*, *180*(1), 433–462, doi:10.1111/j.1365-246X.2009.04429.x.
- Tarantola, A. (1984), Inversion of seismic reflection data in the acoustic approximation, *Geophysics*, *49*(8), 1259–1266, doi:10.1190/1.1441754.
- Tromp, J., C. Tape, and Q. Liu (2005), Seismic tomography, adjoint methods, time

- reversal and banana-doughnut kernels, *Geophysical Journal International*, *160*(1), 195–216, doi:10.1111/j.1365-246X.2004.02453.x.
- Uchide, T., and S. Ide (2007), Development of multiscale slip inversion method and its application to the 2004 mid-Niigata Prefecture earthquake, *Journal of Geophysical Research: Solid Earth*, *112*(B6), doi:10.1029/2006JB004528.
- Wald, D. J., and R. W. Graves (2001), Resolution analysis of finite fault source inversion using one- and three-dimensional Green's functions 2. Combining seismic and geodetic data, *Journal of Geophysical Research*, *106*(B5), 8767–8788.
- Yagi, Y., and Y. Fukahata (2008), Importance of covariance components in inversion analyses of densely sampled observed data: an application to waveform data inversion for seismic source processes, *Geophysical Journal International*, *175*(1), 215–221, doi:10.1111/j.1365-246X.2008.03884.x.
- Yoffe, E. H. (1951), The moving Griffith crack, *Philosophical Magazine*, *42*(330), 739–750.
- Yu, S.-B., L.-C. Kuo, Y.-J. Hsu, H.-H. Su, C.-C. Liu, C.-S. Hou, J.-F. Lee, T.-C. Lai, C.-C. Liu, and C.-L. Liu (2001), Preseismic deformation and coseismic displacements associated with the 1999 Chi-Chi, Taiwan, earthquake, *Bulletin of the Seismological Society of America*, *91*(5), 995–1012.
- Zeng, Y., and C.-H. Chen (2001), Fault rupture process of the 20 September 1999 Chi-Chi, Taiwan, earthquake, *Bulletin of the Seismological Society of America*, *91*(5), 1088–1098.